IMPERIAL COLLEGE OF SCIENCE, TECHNOLOGY AND MEDICINE
UNIVERSITY OF LONDON

INTERACTION BETWEEN FUNDAMENTAL LAMB MODES AND DEFECTS IN PLATES

by

Olivier Diligent

A thesis submitted to the University of London for the degree of
Doctor of Philosophy

Imperial College London
Mechanical Engineering Department
Exhibition Road
London SW7 2AZ

2003

Abstract

The thesis is motivated by the goal of developing techniques for inspecting plate structures using ultrasonic Lamb waves. Many engineering structures are composed of large areas of flat or curved plates, including, for example, oil and chemical storage tanks. The inspection of a plate by Lamb waves requires the propagation of multiple signals in order to achieve full coverage. This can be achieved using a plate tester device which has been developed separately. The work presented in this thesis investigates the interaction of the fundamental Lamb modes with a free edge of a plate and with different types of defects with very simple geometries. This is studied in order to bring understanding of the detection capabilities of the inspection system, as well as to aid the signal processing procedures used by the system. Finite Element, analytical and experimental studies are compared.

The reflection of Lamb waves when the fundamental antisymmetric Lamb mode (A_0) or the fundamental symmetric Lamb mode (S_0) is incident at the free end of a plate is studied, in order to identify the extent to which the generation of non-propagating modes influences the field local to the end of the plate. The results of this work are important if the pate tester device is placed close to a defect, or close to the edge of a plate, because the non-propagating modes could then interfere with propagating modes and pollute the signal processing. Two frequencies are investigated. A simple case is a frequency below the second anti-symmetric mode cut off frequency, where there is only one anti-symmetric mode (A_0 mode). A second and more complex case is above this cut-off frequency when there are more than one anti-symmetric mode. These two cases show that there is some additional motion due to the non-propagating modes. It is also shown, in contrast, that no such additional motion happens in the case when the fundamental symmetric mode S_0 is incident at the end of the plate.

The interaction of the S_0 Lamb mode with circular defects is investigated. The low frequency mode S_0 is the most attractive of the two fundamental modes for Non

Destructive Evaluation (NDE) because it has low dispersion (the velocity is approximately constant for low frequencies), it has a high group velocity, it is equally sensitive to defects at any depth in the plate and, if the plate is immersed in a fluid medium, the attenuation due to leakage is very small. Two types of generation and two types of defect are studied. First the S_0 Lamb mode is excited by a plane wave and interacts with a circular hole through the full-thickness of the plate. Second, the S_0 mode is still excited by a plane wave but interacts with a part-depth circular hole. These two studies give the first understanding of the reflection behaviour, showing the mode conversion at the defect, the beam spreading of the reflected wave and the creation of circumferencial waves that propagate around the hole. Finally the S_0 mode is excited by a small circular source and interacts with the same defects. This is of particular interest because it gives information which is directly applicable to what takes place with the plate tester device.

Acknowledgements

I would like to thank my supervisors, Dr. Mike Lowe and Prof. Peter Cawley, who have provided invaluable guidance throughout this study. I must also acknowledge their patience and English skills which help me to conclude this project.

None of the work presented here would have been accomplished without the help of the members of the NDT group at Imperial College.

This project would also not have seen light without A. Gorvet from BP Exploration, R. Gregory from Esso Engineering (Europe) Ltd, B. Roosenbrand from Shell Global Solutions, C.P. Hsiao from Chevron and the UK Engineering and Physical Sciences Research Council (EPSRC) who funded the research.

Finally, my deepest thoughts go to my family (Francis, Sylviane, Nicolas and Mélanie) who, 1159 km away from London, supported me through these years of hard work, while Mike Lowe and Peter Cawley were torturing me...

Contents

List of Figures

List of Tables

Nomenclature

a	radius
A	amplitude
A_i	antisymmetric mode
α	complex amplitude
b	hole depth
c	velocity
D	distance
d	plate thickness
δ	distance from edge of hole
δt	time step (Finite Element)
Δx	biggest dimension across a single element (Finite Element)
Δs	shortest side-length of an element (Finite Element)
E	Young's modulus
$\hat{e_r}, \hat{e_z}$	unit vectors
$F(\omega)$	frequency spectrum
f	frequency
h	plate thickness
i	$\sqrt{-1}$, integer
j	direction, integer
k	complex wavenumber
$k^{'}$	real part of complex wavenumber
$k^{''}$	imaginary part of complex wavenumber
λ	wavelength
n	integer
ν	Poisson's ratio
ω	angular frequency
Φ	phase
r, θ, z	cylindrical co-ordinate axis

continue on next page

continue from previous page

R	reflection coefficient
ρ	density
S_i	symmetric mode
σ	normal stress
$\boldsymbol{\sigma}$	stress distribution
$\bar{\bar{\sigma}}$	stress tensor
t	time
τ	shear stress
U	displacement
v	velocity
V	particle velocity
w	notch width
X, Y, Z	cartesian co-ordinate axis
superscript $^>$	outer region of a hole (analytical)
superscript $^<$	inner region of a hole (analytical)

Chapter 1

Introduction

1.1 Motivation

This thesis reports work done as part of a project to design a low frequency ultrasonic inspection technique which will test large areas of thick walled structures such as pressure vessels or petro-chemical storage tanks. Figure 1.1 shows a photograph of a typical oil tank. Tank floors are composed of many welded plates. The plate thickness can vary between 5 mm and 20 mm and the area of each plate can be 20 m^2. The arrow shows a corrosion patch that needs to be detected by the ultrasonic inspection technique, corrosion also has to be found if formed underneath the plate.

The usual inspection of such large areas is very time consuming and thus expensive because conventional techniques require a test point by point in two dimensions over the whole area. Two conventional techniques are widely used and measure thickness changes. The first one is SLOFEC (Saturated LOw Frequency Eddy Current) (see for example [2]). The technique uses the magnetic biased eddy current principle. By superimposed DC-magnetization, the depth of penetration in the material is increased. This technique is used for testing through-corrosion, coating, rubber and plastic layers. SLOFEC scanners have been developed for (semi) automatic Non Destructive Testing (NDT) inspections. The second and older technique is called MFL (Magnetic Flux Leakage) (see for example [3]). The magnetizer module induces a magnetic circuit into the floor to produce a high magnetic flux density within the

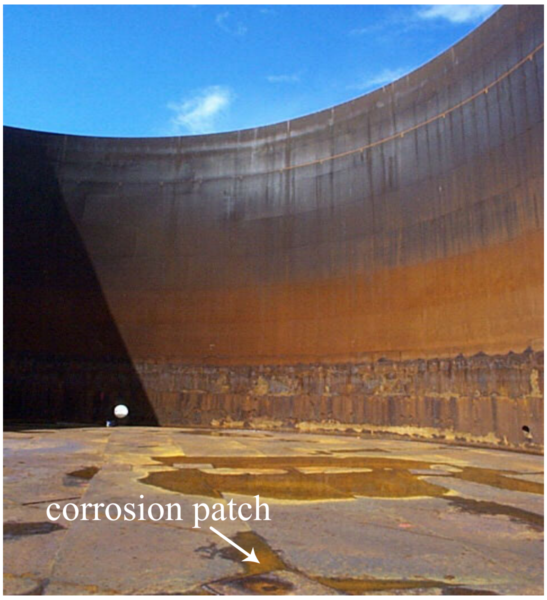

Figure 1.1: Photograph of an oil tank. The arrow shows an example of a corrosion patch

plate. Changes in shape such as defects or corrosion pitting cause localized flux leakage at the top and bottom surfaces of the plate. The inspection instrument's Flux Leakage (FL) sensors detect these perturbations in the magnetic field. The advantage of these two methods is that the floor thickness can be given in millimetres, but again, there are point-by-point measurement techniques, and both are very time consuming.

Conventional ultrasonic inspection techniques can be used through-thickness for a similar kind of scan as SLOFEC or MFL, but besides also being time consuming, there are in addition coupling problems. These conventional ultrasonic inspection techniques use bulk longitudinal or shear waves which propagate in the region of the structure immediately around the probe. The reflections from the features can be detected either by the emitter itself (pulse-echo test) or by a receiver placed adjacent to it (pitch-catch test). This method is not very attractive because of the large areas to be scanned and in practice it is used mostly for spot checks or to investigate local areas where there is a particular concern.

An alternative method is to use ultrasonic Lamb waves which propagate along the

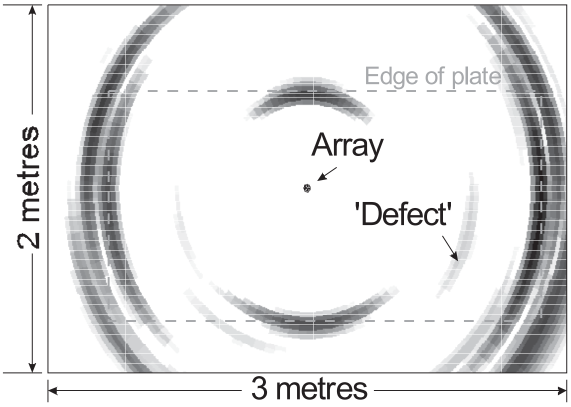

Figure 1.2: Example of a map of the plate

plate and may be reflected by any defects. These waves can inspect all positions along a line; thus the time of inspection can be reduced. Lamb waves will be discussed in greater detail in section 1.2.

This approach of using Lamb waves has been implemented in a project involving the author and Dr Paul Wilcox. Dr Wilcox has developed a plate tester device [1, 4]. This is a phased array transducer, which generates a controlled signal in a chosen direction in the structure and then receives the reflections coming from defects and other features. Conceptually, the operation of the array may be regarded as a number of pulse-echo tests, each looking in a different direction at the surrounding plate. The final output from the array is displayed to the operator as a two-dimensional grey scale map of the plate, where the colour scale indicates the amplitude of the reflected signal at each point in the plate (white low, black high). Figure 1.2 shows an example of a map of a plate where the edges can be clearly seen as well as a 10 mm diameter hole drilled through the thickness of the plate, labelled 'defect' in the figure.

The part of the project investigated in this thesis is the interaction of the waves with different kinds of features and defects. It is essential when processing received signals to account properly for those which arise due to reflection from different features. For example, studying interactions from corrosion-like defects is a necessity in order to understand what modes are converted at the defect and how they behave when they propagate in the plate. Their amplitude, the beam spreading, and their interaction with additional displacements created at the feature were studied. It is also important to be aware of how far the transducer needs to be from an edge of the plate or a defect, in order to avoid detecting additional displacements (non-propagating modes), which may be generated at the edge of the plate.

1.2 Lamb waves

Lamb waves are guided elastic waves which propagate in the plane of a plate and, like bulk elastic waves, their interaction with defects means they can be used for inspection purposes. The plate forms a guide to the ultrasonic waves, which directs them along the structure. Because they can propagate in the plane of a plate, and as the material used here has very little damping, the energy of the waves is practically not absorbed as they travel, and thus they can travel over long distances. Hence, reasonably large area of the tested structure can be inspected from a single location.

Figures 1.3(a) and 1.3(b) show examples of velocity dispersion curves for a 1 mm thick steel plate. The dispersion will be explained later in the section. These curves were calculated using the DISPERSE code [5, 6]. Figure 1.3(a) displays the dispersion curves as phase velocity against frequency. This display describes the rate at which an individual crest of the wave travels. The group velocity projections are shown in Figure 1.3(b). This figure displays the speed at which a guided wave packet travels. For isotropic non-attenuative media, this can also be seen as the velocity of the energy of the wave. The attenuation (decay of the guided wave) or the wavenumber (relationship between temporally and spatially varying wave characteristics along the direction of propagation) as a function of frequency are further representations of the dispersion curves.

Two types of Lamb modes exist: symmetric (solid lines) and anti-symmetric (dashed lines). The symmetric modes are symmetric with respect to the mid-plane of the plate and are noted S_i, where i is the order of the mode. Anti-symmetric modes are

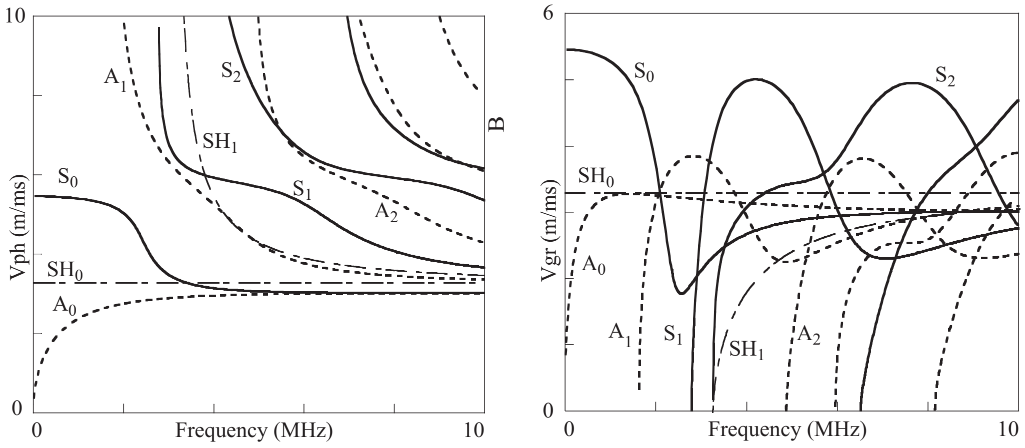

(a) phase velocity

(b) group velocity

Figure 1.3: (a) Phase and (b) Group velocity dispersion curves for a 1 mm thick steel plate. Solid lines denote symmetric modes and dashed lines denote anti-symmetric modes.

anti-symmetric with respect to the mid-plane of the plate and are noted A_i.

It can be seen from Figures 1.3(a) and 1.3(b) that the number of modes increases with the frequency. Thus, an infinite number of symmetric or anti-symmetric modes can exist. For each of these modes, their velocity varies with frequency, which means that they are all dispersive. The effect of dispersion on a propagating wave packet of acoustic energy is that the energy spreads in time and space as it propagates. Hence, close to the source, the signal is similar to the input, but as the distance increases, the signal duration increases and the peak amplitude decreases. Both of these features are undesirable in an inspection application as the sensitivity decreases, and as reflections from two artefacts in close proximity might not be separated and identified. The use of Lamb waves is then not as straight-forward as it is for bulk waves.

The selection of a suitable Lamb mode is fundamental to the project. The aim of long-range inspection is to investigate large areas rapidly. Hence, the dispersion is a key factor and modes with low dispersion have to be chosen and the signal to noise ratio needs to be as high as possible to maximize the range of inspection. Another important effect is the attenuation. Attenuation will primarily be due to leakage of energy into surrounding fluid in any test structures which contains fluid or are in contact with fluid. Hence it is very likely that this will reduce the choice of a suitable Lamb mode to those who have very little out-of-plane displacement at the contacting surface of the plate. The fundamental S_0 Lamb mode at low frequency satisfies such criteria. It is not very dispersive, the resolution will not worsen as the signal duration increases and the peak amplitude of the signal will not decrease as it propagates, hence the signal to noise ratio does not change; and it has very low attenuation if the plate is in contact with a fluid. These properties make it a suitable mode for the plate tester device.

The small number of modes present at low frequency is also useful. When the incident S_0 mode reaches a defect, some mode conversion into other modes may occur [7, 8, 9, 10, 11, 12, 13]. But at this low frequency, only one other Lamb mode is present: the fundamental anti-symmetric mode A_0. The A_0 wave has stress and displacement fields which are simple too, but these are anti-symmetric with respect to the mid-plane of the plate, and it displays the characteristics of flexural behaviour. Besides the Lamb waves, another possible wave within the frequency range is the SH_0 wave. The SH_0 wave is the fundamental symmetric wave of the family of waves whose particle motion is parallel to the plate surfaces and normal to the direction of propagation.

Although Lamb produced the dispersion equation for acoustic wave propagation in plates in 1917 [14], it was not until 1961 that Worlton [15, 16] gave an experimental confirmation of Lamb waves at megacycle frequencies and that Lamb waves can be used for non destructive testing purposes. Since then, much work has been carried out on the use of Lamb waves and other guided waves, a good review can be found in [17].

In general, Lamb waves are used for two different purposes. Firstly, there is short range propagation, where Lamb waves may be used at relatively high frequency in preference to conventional techniques. This purpose includes material characterization [18, 19] and the detection of defects close to interfaces, see for example [20]. In these cases the dispersion is not of such importance as the wave propagates over short distances but the sensitivity is a key factor.

The second purpose is in applications where the wave propagates over long distances. Applications of long range inspection include pipeline inspection [21, 22, 23, 24, 25, 26, 27] or inspection of composites [28, 29, 30, 31].

More about the theory of Lamb waves will be discussed in the following sections.

1.3 Background to research

This section will present a summary review of earlier work which is of relevance for the thesis. Two main topics are presented. The first is the generation of localised perturbations when the incident wave reflects at a free end of a plate; the second is the scattering from circular defects. Scattering is an extremely broad area of research and in accordance with the work presented later in the thesis, two main lines are discussed here. The first one is the interaction between an incident wave and small inclusions and the second is the reflection and mode conversion from circular defects.

1.3.1 Non-propagating modes

It is well known that the reflection of Lamb waves from a free end of a plate is often accompanied by the generation of localised displacements that do not propagate into the plate. The non-propagating modes, which exist solely in the vicinity of the end of the plate, have been reported and studied quite broadly [7, 32, 33, 34, 35, 36, 37]. The work of Torvik [7] is of particular interest. He describes a method using the modes of vibration for an infinite plate as elements of an expansion applicable to semi-infinite plates. The method is employed to study the reflection of an infinite train of waves from the edge of an elastic plate. The incident waves induce other, non-propagating, modes. The evanescent modes affect the stress distribution of a portion of the end of the plate. Gazis [36] and Mindlin [32] have also studied this reflection using an approximate, two-dimensional, solution. Their study employs only the first three roots of the frequency equation. At low frequency, this includes only the propagating modes and the first pair of non-propagating modes. Most of the time, the interest in using these non-propagating modes is in properly accounting for all contributions to the field around a discontinuity when a normal mode superposition technique is employed, see for example the work of Auld [33], Le Clézio [38] or Wang *et. al.* [39].

In this thesis, analytical, Finite Element and experimental results for the reflection of the first anti-symmetric Lamb mode and the generation of non-propagating modes at the free end of a plate will be compared. A key novelty of this research will be the measurement of the displacement field of the non-propagating modes using a laser interferometer.

1.3.2 Scattering

The work which is presented in this thesis is motivated by the development of a technique in order to inspect a plate. One part of this work is the interaction of Lamb waves with circular defects. When the incident wave reaches the defect, it is reflected and mode converted, and these waves propagate back in the plate. This is called scattering.

Scattering is a very wide topic and has been discussed by many authors. The scattering of ultrasonic waves from contacting surfaces, see for example [40, 41, 42, 43, 44], is one example of this topic. Different models were developed for the understanding of the transmission and reflection of an incident wave with contacting surfaces. It has been shown that the transmission between two surfaces is a result of the large number of micro-contacts [40]. Also developed in this field is an understanding of the interaction between waves and contacting asperities, and that the density and size of the contacts (or asperities) can be estimated from acoustical measurements [41, 42, 43, 44]. Although very interesting, this field of research is not directly exploitable for the work described in this thesis. The defects that are studied in the thesis are between one and three wavelengths of the incident wave (approximately between 50 and 150 mm), and there is only one defect present in the portion of the plate modelled.

More important in regard to the work presented here, a key area of scattering investigation has been the reflection and mode conversion of guided waves when they are incident to a single defect, see for example [11, 34, 45, 46, 47, 48, 49, 50, 51, 52]. Strong interaction between the incident wave and the flaw is important to the location and sizing of the defect. These cited studies assume in general a two-dimensional plain strain domain, representing a section through the plate and defect, which are infinite in the direction normal to the plane. This approximation is only valid when the size of the defect is large compared with the beam of the wave, whereas in this thesis, the size of the defect can be narrower than the width of the excitation. But these approaches are very useful for the understanding of the phenomena. Other work done on three-dimensional defects have been published, see for example [39, 53, 54, 55]. In these works, the authors study the interaction of an incident wave with a spherical or cylindrical shaped cavity. Their analytical work gave great understanding of the behaviour of the reflected waves.

When the incident wave reaches the hole, some additional waves, other than Lamb waves are mode converted. These waves, first introduced by Viktorov [56], are called "circumferential creeping waves". They are Rayleigh-like waves and are formed when the incident wave reaches the hole. They have been studied quite extensively in relation to incident shear waves by Nagy *et. al.* [57, 58], and by various authors [59, 60, 61, 62, 63, 64]. In the case developed in the thesis, the creeping waves are generated from an incident S_0 wave (instead of a SH wave), but the phenomenon is essentially the same. It is interesting to notice that these waves re-radiate some of the energy into the solid. The re-radiated field can then be observed as a weak scattering perturbation caused by the curvature of the surface. These waves can also be used in order to locate and size cracks [58, 65]. For sizing the crack, the amplitude of the circumferential wave is used. The crack is then located by calculating time delays between a perfect hole and its backscattered counterpart (if a crack is present). This time delay gives the distance between the defect and the receiver as long as the size of the hole is known.

This thesis will show the behaviour of the reflected and scattered waves at different angles around the hole. Finite element, analytical and experimental results will study their interaction, beam spreading, and the importance of the creeping waves.

1.4 Overview of the thesis

This thesis presents the interaction between the fundamental Lamb modes and different types of features. Two main themes are addressed. The first is the reflection of the first antisymmetric Lamb mode from a free edge of a plate. This is studied in order to give understanding on where the plate tester device has to be placed for a test in order to avoid the measurement of additional displacements which only exist in the vicinity of the end of the plate or of a defect. The second is the interaction between an incident symmetric mode with a circular defect; this is studied in order to find out the sensitivity of the inspection technique.

Chapter 2 studies the reflection of the fundamental mode A_0 from the end of a plate, in order to identify the extent to which the generation of non-propagating modes influences the field. Analytical predictions, Finite Element simulations and experimental measurements are presented for frequencies below the A_2 cut-off. It is shown, for frequencies below the A_1 cut-off, that reflection of the A_0 mode is accompanied by a delay in phase, and that there is significant additional motion due to non-propagating modes within about 5 plate thicknesses of the end. The extent of this additional motion in the vicinity of the end of the plate is demonstrated by subtracting the contribution of the propagating modes from the displacement field. The wave field at frequencies above the A_1 cut-off is more complex because the A_1 as well as the A_0 propagating modes are present at the end of the plate. Nevertheless, it has still been possible, using analytical predictions and Finite Element simulations, to demonstrate the additional motion due to the non-propagating modes. The reflection of the S_0 mode, which is much simpler in its behaviour, is also considered for completeness.

The interaction between an incident S_0 Lamb mode with a corrosion like defect is presented in three different chapters (3-5). The interactions of Lamb waves with cracks or notches have already been studied by others using plain strain models [51, 66]. Here we will be interested in circular defects as a first approximation of corrosion patches. The studies start with the simplest shape of defect or source (plane stress model, hole through the full thickness of the plate and plane wave source) and tend towards more realistic cases (three dimensional, flat-bottom defect) as we go through the chapters in order to better match the wave field of the real testing device and more realistic flaws.

Chapter 3 presents the first study of the interaction of the S_0 Lamb wave with a circular through-thickness hole in a plate. The study is limited to the non-dispersive frequency range of this wave, in which the distributions of stress and displacement are simple. This allows a Finite Element analysis to be undertaken using a two-dimensional membrane discretisation. Predictions of the direct reflection of the S_0 mode and the lateral scattering of the SH_0 mode are made for a range of diameters of the hole. At the same time, an analytical solution based on modal superposition is developed, and this is also used to predict the reflection and scattering coefficients. Both sets of predictions are validated by experimental measurements. It is found that the trends of the reflection coefficients for different hole diameters, frequencies and distances from the hole satisfy a simple normalisation. On a detailed scale, the functions exhibit undulations which are shown to result from the interference of the direct reflection with the re-radiation of a creeping wave which travels around the hole.

In Chapter 4 the second study of the interaction of Lamb waves with a circular defect is presented. The Lamb wave mode chosen was again the S_0 mode in the low frequency-thickness regime. A three dimensional Finite Element mesh was generated, representing an area of the plate with a circular part-depth hole (33% or 50% of the plate thickness deep). The specular reflection of an incident S_0 wave is predicted and shows the importance of several factors, such as the decay in amplitude of the reflected wave and the generation of "creeping waves" which travel around the hole.

Chapter 5 presents the third study of the interaction of Lamb waves with a circular defect. The Lamb wave mode chosen was again the S_0 mode but this time it was excited by a small circular source. A three dimensional Finite Element mesh was generated, representing an area of the plate with a 50% of the plate thickness deep circular hole. The specular reflection of an incident S_0 wave was predicted and compared with the plate tester device as well as with a single EMAT transducer. This chapter assesses the significance of the path lengths, wavelengths and defect sizes on the reflection characteristics.

Finally, Chapter 6 summarizes the work undertaken through the thesis and future work is recommended in Chapter 7.

Chapter 2

Predictions and measurements of non-propagating modes at the end of a plate when the fundamental anti-symmetric mode A_0 is incident

2.1 Introduction

It is well known that the reflection of a Lamb wave from the end of a plate is very often accompanied by the generation of additional localised disturbances. These non-propagating modes, which exist solely in the material near the end of the plate, and which are present only during the time it takes for the Lamb wave to reflect, have indeed been studied and reported quite extensively, see for example [7, 32, 33, 34, 35, 36, 37, 38]. The work of Torvik [7] is particularly recommended. Very often the interest in considering these modes is in properly accounting for all contributions to the field around a discontinuity when applying normal mode superposition techniques [33, 37, 38, 39].

The aim of the work presented in the thesis is to develop a technique which can be used rapidly to assess the integrity of a plate using Lamb waves. The notion is that a transducer unit placed on the plate will generate and receive Lamb waves in controlled directions; processing of the arrival of reflected waves will then allow a map of corrosion anywhere in the plate to be constructed (see section 1.1). Some preliminary results of the work on this technique have already been reported [4, 67]. The value of the knowledge of the non-propagating modes for that work is: (1) it is essential when processing received signals to account properly for those which are reflections from the edge of the plate under test; for example, if not understood, phase delays of these reflections could adversely affect the performance of a phased array transducer; (2) it is important to be aware of how far the transducer needs to be from the edge of the plate in order to avoid detecting the additional localised displacements.

The study of the non-propagating modes which is presented in this chapter was conducted in the context of collaborative work between the Non-Destructive Testing (NDT) laboratory at Imperial College and the Laboratoire de Mécanique Physique (LMP) of Bordeaux. It resulted in a joint publication [68]. Nevertheless, the majority of the work presented in this chapter was done by the author at Imperial College and unless indicated, it should be assumed that it belongs to the author. The work from Bordeaux will be clearly indicated.

The principal aim of this chapter is to understand what happens at the edge of a plate. This is done by performing a cross-validation of the model developed in Bordeaux with the FE calculations and experiments undertaken at Imperial College, by comparing results for the reflection of Lamb waves and the generation of non-propagating modes when the A_0 mode is incident, at frequencies both below and above the A_1 cut-off frequency. Even though the chosen Lamb mode for the plate tester device is the S_0 mode, when it reaches a non-symmetric feature it will mode convert into other modes [11]. Thus, the A_0 mode will propagate in the plate and this is why its interaction with a free end of a plate needs to be studied. The novel measurements of the fields of the non-propagating modes using a laser interferometer are also included in the validation exercise. Finally, the reflection of the S_0 mode, which is much simpler in its behaviour, is considered briefly for completeness and because of its importance as the primary mode of interest for the plate tester device.

The chapter is in seven sections. The first section presents the properties of the anti-symmetric propagating and non-propagating modes. The second section summaries the analytical model developed at the University of Bordeaux. The experimental set-up used to validate numerical results is presented in the third section, while the procedure for Finite Element simulation is reported in the fourth section. Results are compared and discussed in the fifth section and finally a conclusion is presented, summarizing the results.

2.2 Properties of the antisymmetric propagating and non-propagating modes

Figure 2.1 shows the group velocity dispersion curves for Lamb waves in an aluminium plate (see properties in table 2.1). These, and all other dispersion curves and mode shapes in this chapter, were plotted using the predictive model DISPERSE [5, 6]. Lamb wave dispersion curves are scalable by the product of the frequency and the plate thickness. Thus the curves here show the frequency-thickness on the horizontal axis. The work which is presented here is focused on the A_0 mode at two different frequency-thicknesses: (1) at 1 MHz-mm, where it is least dispersive and is also below the A_1 cut-off; (2) at 2.7 MHz-mm where both the A_0 and A_1 modes are present as propagating modes (“real modes”), and A_1 is relatively non-dispersive. The edge of the plate is assumed to be cut perfectly square, and the A_0 wave is assumed to be normally incident. It follows that at 1 MHz-mm there is no mode conversion of the propagating modes due to the symmetry of the reflector: an incident mode of A_0 reflects as A_0 with a reflection coefficient amplitude of unity. On the other hand, at 2.7 MHz-mm the incident A_0 mode can be reflected partially as A_0 and partially, by mode conversion, as A_1.

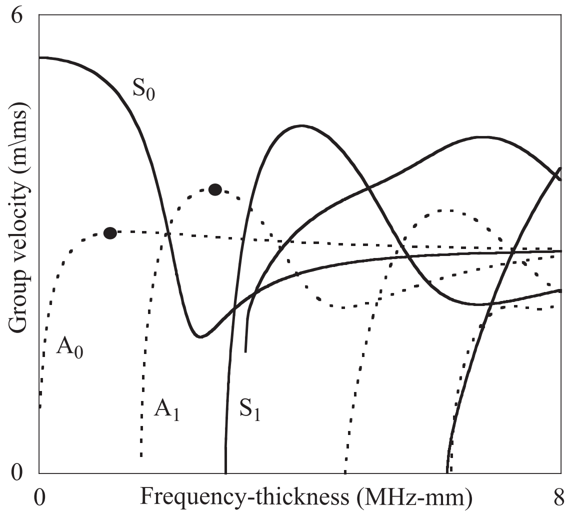

Figure 2.1: Group velocity dispersion curves for Lamb waves in an aluminium plate. Solid lines are symmetric modes, dashed lines are antisymmetric modes. The two dots show the two frequencies (1.0 and 2.7 MHz-mm) at which the study was carried out.

Density (ρ)	Poisson's ratio (ν)	Young Modulus (E)
2.7 g/cm^3	0.33	70.75 GPa

Table 2.1: Material properties for aluminium.

The role of the non-propagating modes when Lamb waves are reflected from the end of a plate is easily understood by examining the mode shapes of the A_0 and the A_1 modes, shown for frequency-thickness products of 1 MHz-mm and 2.7 MHz-mm in Figure 2.2. The z direction is the direction of propagation of the wave and the x direction is the normal to the plate. Considering for example the A_0 mode at 1 MHz-mm, the two components of the stress field of importance here, the normal stress (σ_{zz}) and the shear stress (τ_{xz}), show the characteristic distributions corresponding to the flexural behaviour of the wave. Shown by Figure 2.3, and very important, is the phase relationship; in fact although both components vary harmonically in time, τ_{xz} lags 90 degrees in phase behind σ_{zz}. At this frequency, and considering just the propagating modes, it is clear that an A_0 mode incident at the square end of a plate must reflect also in A_0 with unit amplitude reflection coefficient at 1 MHz-mm. However, because of the phase difference of the stress components, there is no linear combination of incident and reflected modes which can satisfy the requirement that both σ_{zz} and τ_{xz} are zero across the end of the plate. It is then of course the presence of non-propagating modes which allow these boundary conditions to be satisfied. The same feature happens at 2.7 MHz-mm when A_0 is incident and is partially reflected into A_0 and A_1. There is no combination at the end of the plate to satisfy the boundary condition and hence non-propagating modes are needed.

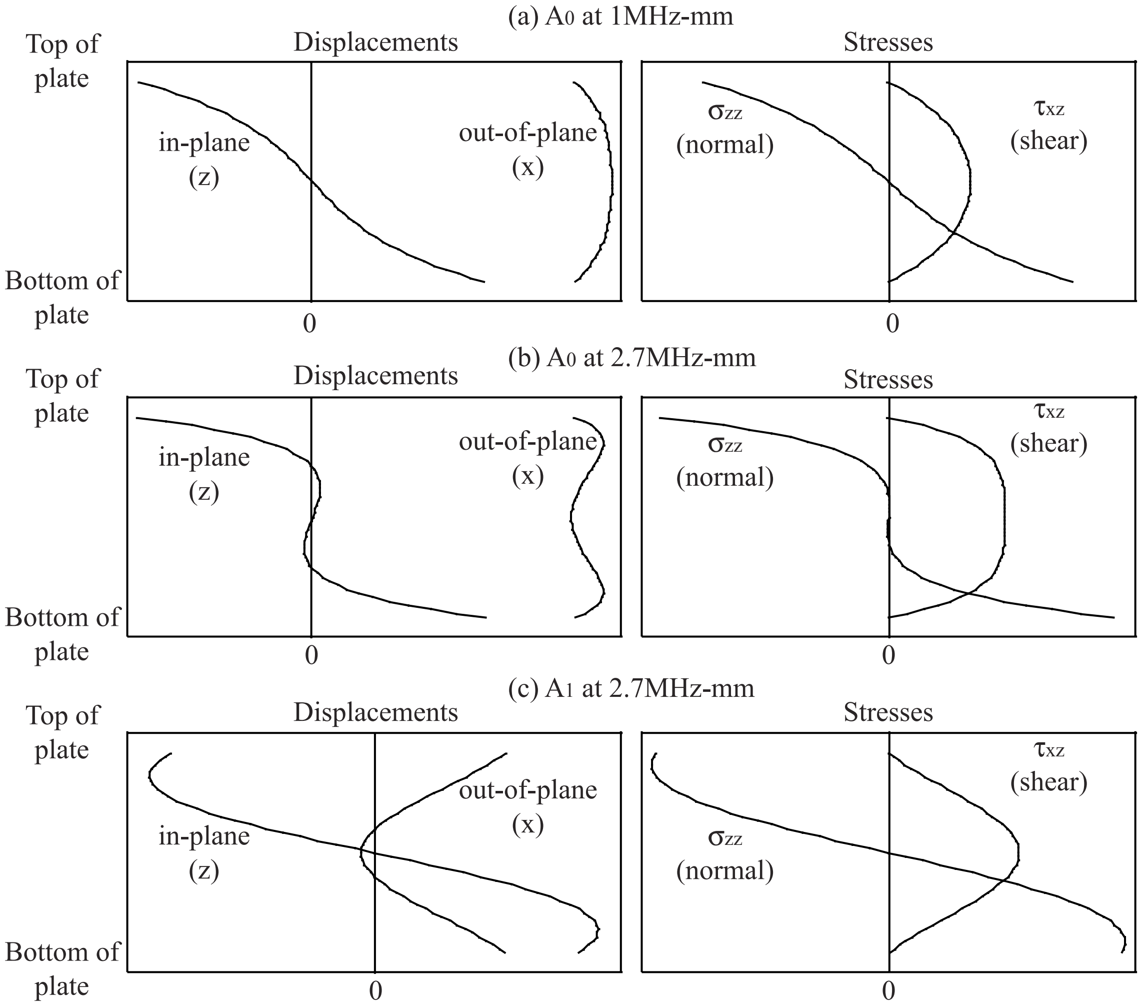

Figure 2.2: Mode shapes of the A_0 and A_1 modes in an aluminium plate: (a) A_0 mode at 1 MHz-mm; (b) A_0 mode at 2.7 MHz-mm; (c) A_1 mode at 2.7 MHz-mm.

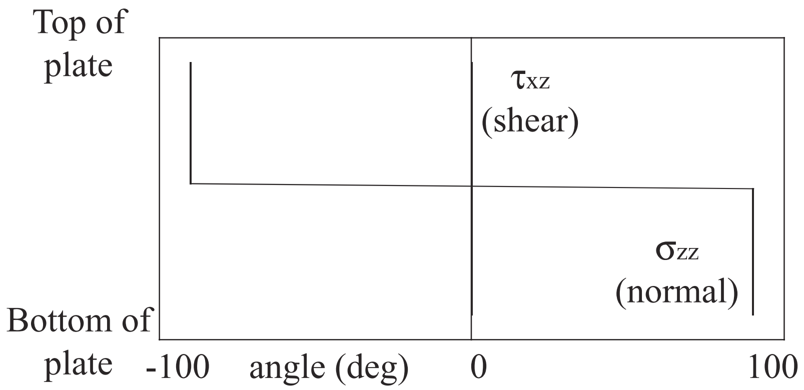

(a) A_0 at 1 MHz-mm

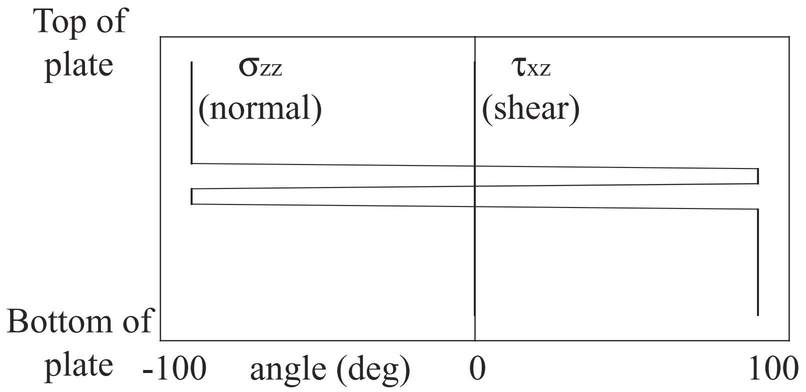

(b) A_0 at 2.7 MHz-mm

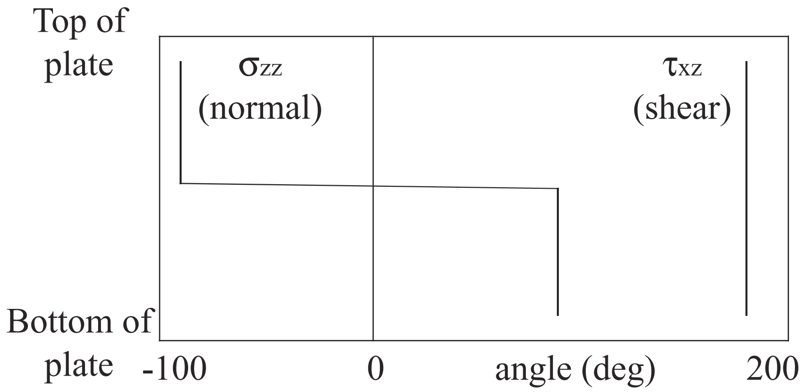

(c) A_1 at 2.7 MHz-mm

Figure 2.3: Stress mode shapes of the A_0 and A_1 modes in an aluminium plate displayed as phase: a) A_0 mode at 1 MHz-mm; (b) A_0 mode at 2.7 MHz-mm; (c) A_1 mode at 2.7 MHz-mm.

Dispersion curves for the anti-symmetric modes in a 1mm thick aluminium plate, including the non-propagating branches, are shown in Figure 2.4. These show similar information to the well-known curves in [32, 33], except that those authors present only the symmetric modes, and also it was chosen here to plot the curves three times with different 2-D projections as an alternative to their 3-D plot. In part (a), the only addition which the non-propagating modes make to the usual Lamb wave phase velocity curves (the real modes) are the branches labelled A_2+A_3 (these two modes are separated in a 3D plot but appear together when displayed in the phase velocity / frequency-thickness plane [69]) and A_4 linking the cut-offs to the origin of the plot. These are in fact complex branches whose wavenumbers have both real and imaginary parts, as can be seen in parts (b) and (c) of the figure. These complex non-propagating modes are therefore characterised by a sinusoidal variation of the field along the plate, described by the real part of the wavenumber, modified by an exponential decay function, described by the imaginary part of the wavenumber. The imaginary part corresponds to Nepers/mm attenuation along the plate (1 Np/mm = 8.69 dB/mm). The shape of a complex mode is illustrated in the sketch in Figure 2.5(b).

The A_1 mode is radically different from A_2 and A_3, its non-propagating branch being entirely imaginary. Thus it does not appear in the phase velocity plot and it has zero value to the left of the A_1 cut-off in the real wavenumber plot. Its shape is thus characterised just by an exponential decay, as illustrated in Figure 2.5(a).

Torvik [7] demonstrated that neither the imaginary nor the complex modes transport energy along the plate. Thus the imaginary part of the wavenumber describes, not an attenuation of energy, but simply the spatial shape of the field. Also, this means that calculations of power flow may only be used to equate the energy of the incident and the scattered propagating modes. Although the mode shapes bear a strong resemblance to the mode shapes of vibrations at the end of a plate, such a comparison can lead to misunderstanding, for two reasons. First, these modes have non-zero stresses at the end of the plate, so it is not possible for them to exist in isolation; they can only be present in combination with other modes. The second point follows from this, that they do not exhibit the ringing of a free vibration mode but exist only while the propagating modes are reflecting.

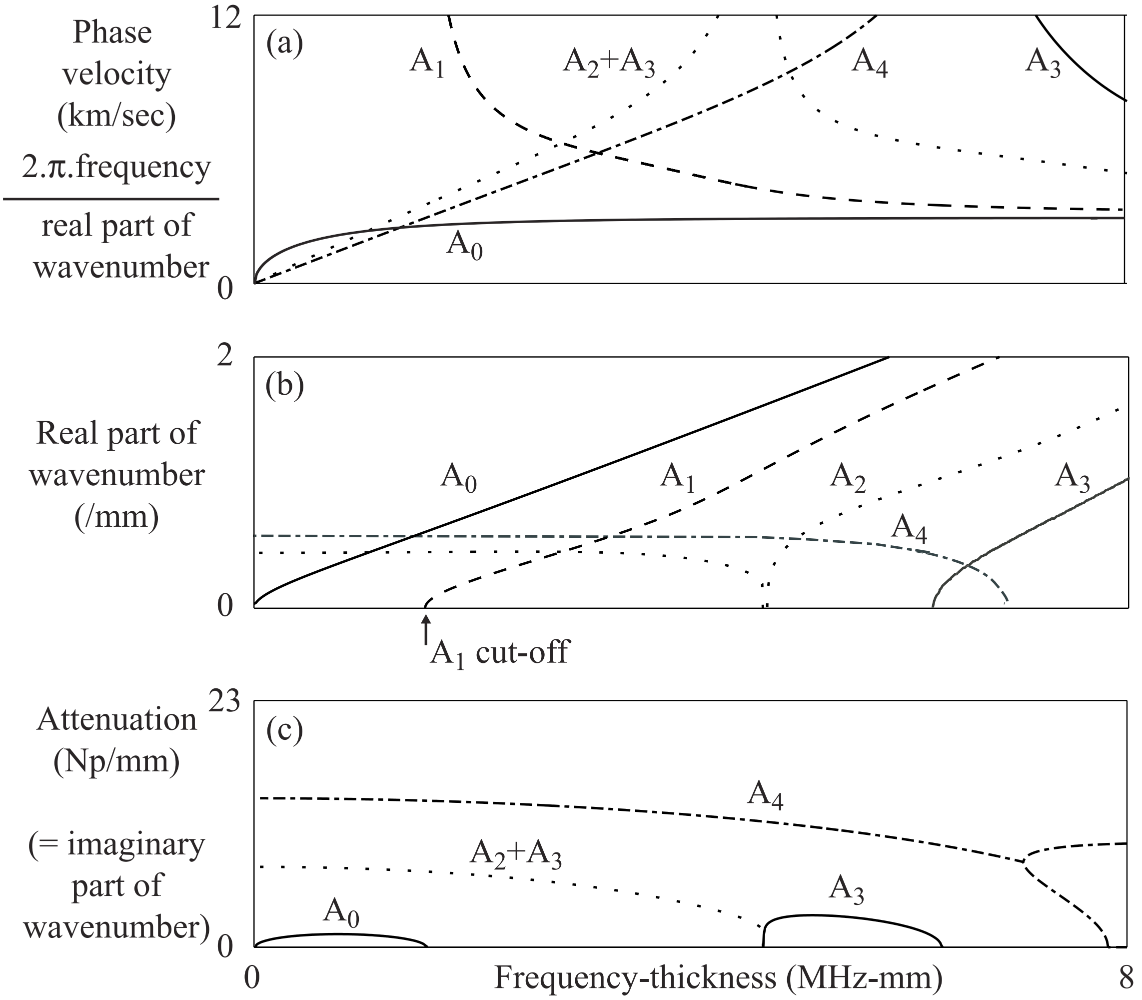

Figure 2.4: Dispersion curves for anti-symmetric modes in a 1mm thick aluminium plate, including non-propagating branches: (a) phase velocity, (b) real part of wavenumber and (c) imaginary part of wavenumber.

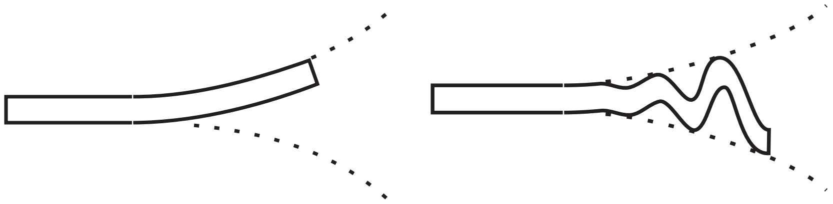

(a) Exponential function

(b) Harmonic function, exponential window

Figure 2.5: Illustration of the shapes of the non-propagating modes at the end of the plate: (a) imaginary modes, (b) complex modes.

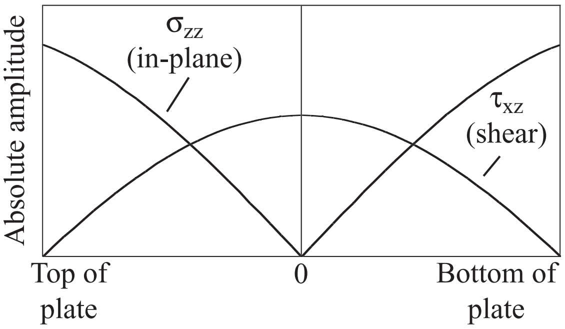

(a) A_1 at 1MHz-mm

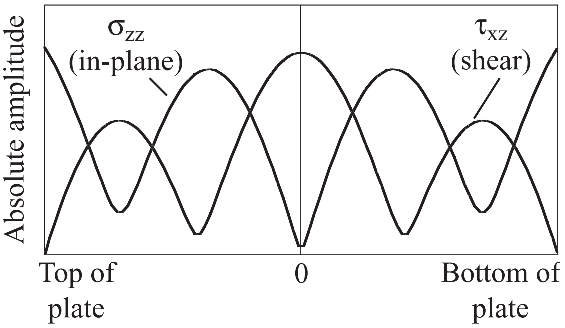

(b) A_2 at 1MHz-mm

Figure 2.6: Stress mode shapes of the non-propagating modes: (a) A_1 at 1 MHz-mm and (b) A_2 at 1 MHz-mm.

The stress mode shapes of the first two non-propagating modes are shown in Figure 2.6(a) and 2.6(b). It is interesting to see here that the shapes of the A_1 mode are very similar to those of the A_0 mode shown in Figure 2. However these A_1 shapes differ in that there is no phase shift between the σ_{zz} and τ_{xz} components. On the other hand the A_2 mode, which is complex, does have phase shifts between stress components; indeed the phase shift varies according to the position through the thickness of the plate. A_2 also shows an increase, with respect to A_1, in the number of cycles in the shape of the through-thickness distribution, a trend which is continued with the higher non-propagating modes in the series.

2.3 Procedure for prediction of the amplitudes of the non-propagating modes using normal mode analysis

The work presented in this section was undertaken by Emmanuel Le Clésio from the Laboratoire de Mécanique Physique (LMP) at the Université de Bordeaux I. The analytical model presented here is a summary of the model he developed as part of his work [69]. The results from his model will be compared later with the ones developed in the thesis.

A normal mode analysis is chosen to solve the reflection of A_0 at the free end of a plate. Every acoustic field that exists in the plate can be developed as an expansion of Lamb waves:

$$V = \sum_n \alpha_n V_n \tag{2.1}$$

where $V_n = v_n(x)e^{i(k_n z - \omega t)}$ is the particle velocity field of the n^{th} Lamb mode. In order to be able to represent completely the acoustic phenomena, all of the Lamb modes that can exist in the plate must be considered [70]. Indeed, at a particular frequency-thickness product, only a finite number of propagating (real), a finite number of imaginary, and an infinite number of complex Lamb modes coexist in the plate. As discussed in the preceding section, the imaginary and complex modes do not propagate energy but they create a spatially transient acoustic field in their excitation area. The reflection of a Lamb mode at the free end of a plate requires selecting specific imaginary and complex roots, so that the corresponding modes have a physical meaning. Here the z axis is defined to be positive in the direction away from the edge of the plate. With this convention, these imaginary and complex wave-numbers must correspond to amplitudes decreasing away from the end [36] according to:

$$\begin{cases} k_n = ik_n^{''}, \text{ for imaginary modes} \\ k_n = \pm k_n^{'} + ik_n^{''}, \text{ for complex modes} \end{cases} . \tag{2.2}$$

The co-existence of real, imaginary and complex Lamb modes at the end of the plate allows stress-free boundary conditions to be satisfied. To fulfil these conditions, from ten to twenty-five locations are considered across the thickness at the end. At these points, the total stress field, produced by the superposition of all the propagating modes, all the imaginary modes, and between ten and twenty complex modes, must vanish. To find the complex amplitudes α_n of all these Lamb modes, a linear system is solved. For each point:

$$\bar{\bar{\sigma}}.\hat{e_z} = \begin{cases} \sum\limits_n \alpha_n \sigma_{zz(n)} \\ \sum\limits_n \alpha_n \tau_{xz(n)} \end{cases} = \begin{cases} 0 \\ 0 \end{cases} . \tag{2.3}$$

An energy balance criterion is used to check the validity of the numerical result. The energy carried by the reflected propagating modes must be as close as possible to the energy of the incident mode. However, if the energy balance is not satisfied, the parameters of computation (i.e. the number of the points through the thickness at the end of the plate and the number of complex modes) are optimised until the best result is obtained. In the results presented in this chapter, the energy balance is always correct within 5% error.

When the system is correctly solved, the particle velocity field at the end can be computed by introducing the amplitudes α_n in equation (2.1). The displacement is given by dividing the particle velocity by $i\omega$. Moreover, to compare to the Finite Element predictions and to the experimental data, the reflection coefficients can be computed as ratios of displacements at the plate surface:

$$R_j^n = \alpha_n \frac{U_j^n(h/2)}{U_j^I(h/2)}, \text{ where j = x, z indicates the displacement component.} \quad (2.4)$$

$U_j^I(h/2)$ and $U_j^n(h/2)$ are the displacements, at the plate surface, in direction j, of the incident Lamb mode (I) and of the reflected Lamb mode (n) respectively.

A single frequency computation of the displacement field at the end and the reflection coefficients of the propagating modes takes about thirty seconds. If similar computations were to be done for a range of frequencies, then the computational parameters should be optimised for some frequencies, thus implying a non-linear increase of the computational time. This method has proved to be numerically stable up to 16 MHz-mm. However, the validity of the results obtained for such high frequency-thickness products has not been confirmed by experimental data, or compared to other numerical predictions. A more thorough description of this model is presented in references [38, 69].

2.4 Experimental set-up for measurement of the non propagating modes

Experimental studies were conducted in order to provide some practical validation for both the analytical and the Finite Element work. The experimental set-up to study the A_0 reflection above the A_1 cut-off frequency requires a very long plate. This can be understood by looking at the dispersion curves plotted in Figure 2.1, from which it can be seen that the group velocities of A_0 and A_1 are very close. In order to fully separate in time these reflected propagating modes, which is necessary in order to calculate the non-propagating modes (see Section 2.5), a 4 m long plate would be needed. Thus, only experiments below the A_1 cut-off frequency have been performed, as the only propagating mode within this frequency bandwidth is A_0.

For practical convenience, an 800 mm x 800 mm x 8 mm thick aluminium plate was used. The A_0 Lamb mode was excited using a piezo-electric transducer (ULTRAN WS100-0.2) aligned at the appropriate coincidence angle ($\simeq 35^o$) in a local water immersion arrangement (see Figure 2.7). The signal was narrow in bandwidth, consisting of a 10 cycle tone burst modified by a Hanning window at 125 kHz (equivalent to 1 MHz for a 1 mm thick plate). This scaling relationship will be exploited so that all the results presented later will correspond to a plate of 1 mm in thickness. The transducer was excited using a WAVEMAKER instrument from Macro Design Ltd (UK). A POLYTEC laser interferometer [71] was used in order to measure the in-plane and out-of-plane displacements at the different locations marked in the figure.

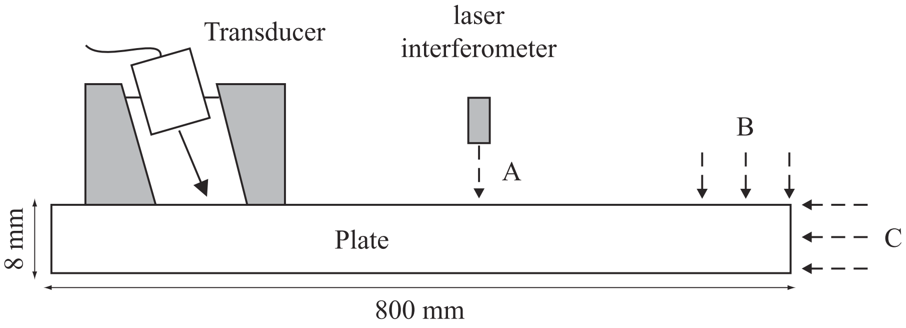

Figure 2.7: Schematic illustration of the experimental set-up.

The interferometer system consists of the interferometer itself, a decoder and two probes connected by fibre optic cable to the interferometer. One of the two probes is nominally the measurement probe and the other the reference probe. In order to measure the in-plane displacement at a surface, both the measurement and the reference probe are aligned so that their beams lie in a plane normal to the surface, and both beams strike the surface at the same spot. Within their plane, the two probes are aligned at equal and opposite directions with an angle of $\pm 30^o$ to the normal to the plate. In this configuration, both displacements measured by the probes contain equal amounts of the out-of-plane component of surface displacement and equal and opposite amounts of the in-plane component of surface displacement. Hence when the reference signal is subtracted from the measurement signal, the out-of-plane components of surface displacement cancel out and the in-plane components of surface displacement add. Using an angle of $\pm 30^o$ for the probes means that the constant of proportionality relating voltage to displacement is equal for both the in-plane and out-of-plane measurement configurations. In order to measure out-of-plane displacements the reference probe is replaced by a mirror while the second probe is simply aligned normal to the surface of the plate.

With the interferometer at the location marked A, both the incident and the reflected A_0 modes could be monitored remote from the end. Then at the positions B and C the displacements comprising the sum of the incident and reflected A_0 modes and the non-propagating modes could be measured. When measuring at C, only the displacements in one half of the plate were measured, those in the other half being expected to respect the conditions of anti-symmetry. While setting up, the attenuation of the signal due to beam spreading, which is inversely proportioned to the square root of the propagating distance, was measured by detecting the change in amplitude of the incident signal for two different locations near A; subsequently all measured amplitudes were adjusted according to the distance travelled so that the results would correspond to those for lossless plane waves.

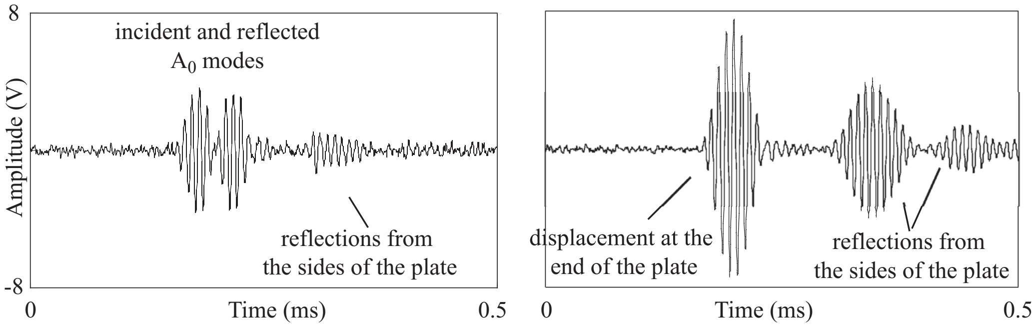

(a) **(b)**

Figure 2.8: Typical experimental out-of-plane displacement at location “B” when A_0 mode of 1 MHz-mm centre frequency-thickness is incident; (a) 40 mm from the end of the plate and (b) at the end of the plate.

Figures 2.8(a), 2.8(b) and 2.9 show typical experimental time histories. Figures 2.8(a) and 2.8(b) shows out-of-plane displacements measured at location B in Figure 2.7. Figure 2.8(a) shows a measurement at 40 mm away from the end of the plate, where the incident and the reflected A_0 modes are just separated but they still include some contribution from non-propagating modes. This measurement will be used later for the calculation of the spatial attenuation of the non-propagating modes. Figure 2.8(b) shows the out-of-plane displacement measured at the end of the plate, on the top surface. Note the increase in amplitude at the end of the plate (b) compared to that at the location 40 mm away (a). Figures 2.8(a) and 2.8(b) also shows some unwanted reflections from the sides of the plate. Fortunately these arrive sufficiently late to be gated out; however they indicate the importance of using a plate of significant width in order to achieve the necessary delay.

Figure 2.9 shows the in-plane displacement at the end of the plate measured at the corresponding location C in Figure 2.7. Some S_0 mode is visible just before the A_0 wave. This is due to the very strong in-plane displacement of the S_0 mode, which is partially excited by the set-up. It did not appear in the out-of-plane measurements because its out-of-plane displacement is very weak, and S_0 is indeed very difficult to excite at this frequency with an out-of-plane forcing technique. The S_0 velocity is much higher than the A_0 velocity (see Figure 2.1) and they are easily and safely separated in time when they have travelled along the plate.

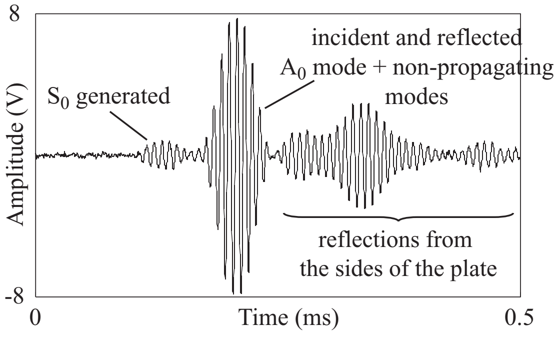

Figure 2.9: Typical measured signal of in-plane displacement near the top surface of the plate at location “C ”, when the A_0 mode of 1 MHz-mm centre frequency-thickness is incident.

2.5 Procedure for Finite Element simulation

The FE simulation is used as a validation in the same way as experiments, and indeed the results will be processed in the same way. In the previous section, the formation of non-propagating modes above the A_1 cut-off frequency has not been studied experimentally due to the closeness of the group velocities of the A_0 and the A_1 modes. However the case of a very long plate is possible in the FE model, and so predictions at both of the test frequencies can be made.

The general features of the FE approach is first discussed and then the specific models for the 1 MHz-mm and 2.7 MHz-mm cases.

2.5.1 Discretisation

The propagation of straight-crested Lamb waves can be modelled using a two-dimensional spatial discretisation. The two-dimensional Finite Element modelling was performed, with the assumption of plane strain, using the program FINEL which was developed at Imperial College [72]. Rectangular elements, with four nodes and linear shape functions, each node having two displacement degrees of freedom in the plane of computation, were used in the models. The spatial discretisation in both cases was chosen to be certain of satisfying the rule:

$$\lambda_{min} \geq 8\Delta x, \tag{2.5}$$

where λ_{min} is the shortest wavelength, within the bandwidth of the signal, of any waves which may travel in the structure, and Δx is the biggest dimension across any single element in the model. This rule has been found to be effective for ensuring accurate modelling, see for example [26].

The program uses a diagonal mass matrix, allowing an efficient explicit time marching algorithm to be exploited. The explicit algorithm is stable provided that the time step δt is short enough to meet the stability criterion [73]:

$$\delta t \leq 0.8\frac{\Delta s}{c}, \tag{2.6}$$

where c is the velocity of the wave and Δs is the shortest side-length of any element.

2.5.2 Simulations below and above the A_1 cut-off frequency

A schematic illustration of the model is shown in Figure 2.10. Plates of 8 mm thickness were modelled, the thickness being chosen for convenience to match the thickness of the plate in the experimental work. In fact, as discussed earlier, the choice of thickness is arbitrary provided that the other spatial dimensions and the frequency are scaled to give the appropriate frequency-thickness product when comparing the results. Accordingly all the results presented later will correspond to a plate of 1 mm in thickness. The models used 16 elements through the thickness of the plate and the elements were defined to be square. Thus the number of elements per wavelength was safely above the 8 elements required, being about 37 elements per wavelength at the frequency-thickness product 1 MHz-mm and 20 elements per wavelength at the frequency-thickness product 2.7 MHz-mm.

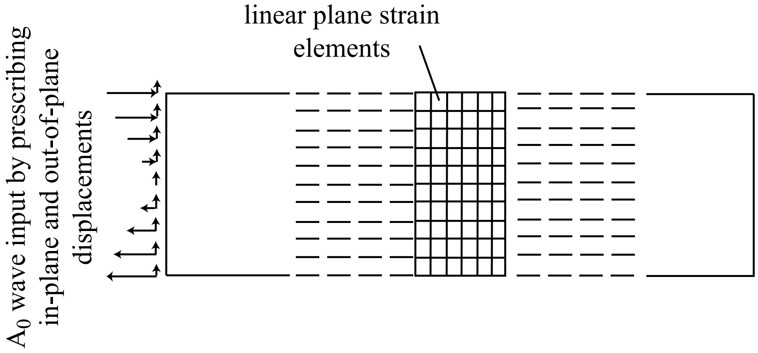

Figure 2.10: Schematic illustration of Finite Element spatial discretisation for a plate, with excitation of the A_0 wave.

The temporal model for the 1 MHz-mm case was chosen to match exactly the experimental A_0 input signal, so a 1 MHz-mm 10 cycle tone burst modified by a Hanning window was excited at one end of the plate. This was achieved by prescribing in-plane and out-of-plane displacements at each node across the thickness (see Figure 2.10). The model was 800 mm long and several regions were monitored. First the end of the plate through the thickness (location “C”) was monitored in the in-plane and out-of-plane directions, every 0.5 mm, providing the total field displacement. A second region was monitored through the thickness at 300 mm and 200 mm away from the end of the plate in order to monitor the incident and the reflected A_0 modes when they are fully separated in time. Finally, in order to study the spatial attenuation of the non-propagating modes, points every 0.5 mm from the end of the plate along the top surface were monitored.

The same model could not be used for frequencies above the A_1 cut-off frequency because then more than one antisymmetric mode exists. The problem is that the A_1 mode is excited by mode conversion at the end of the plate and it propagates back together with the reflected A_0 mode. Since they have very similar values of group velocity, they need to propagate a very long distance before they can be recorded separately. Thus the model was extended to 4 m in length. The separation of these two modes in time is important in order to perform the processing to expose the non-propagating modes which will be explained in the following section of the chapter.

The input A_0 signal for the 2.7 MHz-mm case was similar to the 1 MHz-mm case, except that a 30 cycle signal was used, in order to minimise dispersion over the long propagation distance. Furthermore, the profile of the displacement field which was imposed at the end of the plate had to be chosen more carefully, since it was essential to avoid generating any A_1 in the incident signal. This was done by imposing displacements which matched exactly the mode shape of the A_0 mode at 2.7 MHz-mm [74].

FE predictions of the 2.7 MHz-mm case were done at 3 m and 3.2 m away from the end of the plate, through the thickness of the plate and in both in-plane and out-of-plane directions. Figure 2.11 shows, by way of example, the monitored in-plane displacement at 3.2 m from the end of the plate; it can be seen that the A_0 and A_1 modes are satisfactorily separated. The end of the long plate was also monitored, in exactly the same way as in the 1 MHz-mm case.

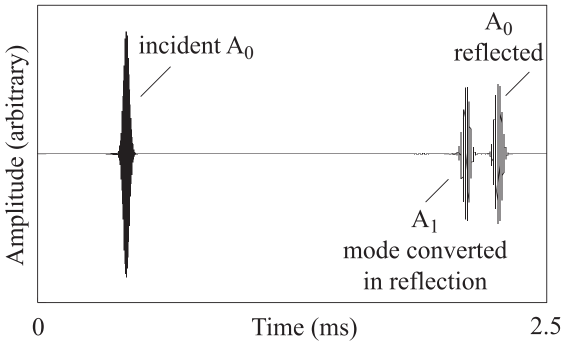

Figure 2.11: Typical FE predicted in-plane displacement signal, when the incident A$_0$ wave has a centre frequency-thickness of 2.7 MHz-mm, monitored at 3.2 m from the end of the plate, showing separation of the reflected A$_0$ and the mode converted A$_1$.

2.6 Procedure for removal of the propagating modes from the total displacement field at the end of the plate

An aim of the analysis in this chapter is to illustrate the extent to which the non-propagating modes contribute to the total displacement field at and near the end of the plate. One way to perform such an illustration is to subtract the contributions of the propagating modes from the total field at the end of the plate, thus leaving only the displacements due to the non-propagating modes. The procedure by which that subtraction is performed will be explained here.

The amplitudes of the incident and reflected propagating modes are known from the remote monitoring at location "A" (these will be presented later and are plotted in Figure 2.12), so this determines the amplitudes of the fields to be subtracted at the end of the plate. However the phases of these waves at the end of the plate are not yet known. The following process is applied sequentially and separately to each of the three possible propagating modes: the incident A$_0$ mode, the reflected A$_0$ mode and (if present) the mode converted A_1 mode.

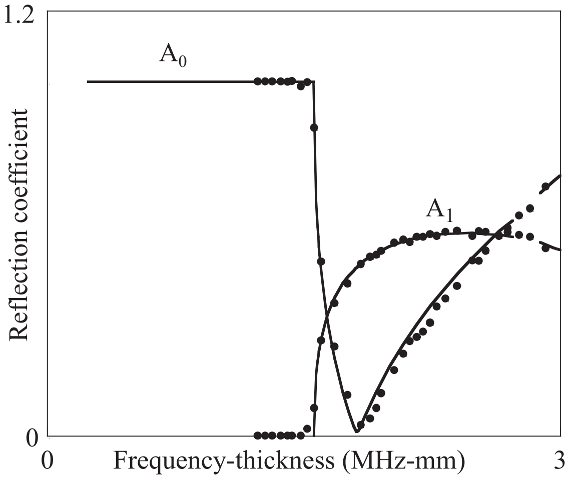

Figure 2.12: Predictions of the reflection coefficient spectrum of the A_0 and A_1 modes when the A_0 mode is incident. Solid lines are analytical solution (Le Clézio model), filled circles are FE results. The reflection coefficient is defined as the ratio of the amplitude of the out-of-plane displacement of the reflected wave to that of the incident A_0 wave, calculated at the surface of the plate.

The out-of-plane displacement of the propagating mode is monitored at two separate locations remote from the end of the plate, let us say locations at distances D1 and D2 from the end of the plate. The FFT of each of these monitored signals is calculated, giving the amplitude and phase at the chosen calculation frequency (1 or 2.7 MHz-mm). The phase, ϕ_{end}, at the end of the plate is then found by linear extrapolation of the phases at D1 and D2:

$$\phi_{end} = \phi_{D2} - (\phi_{D2} - \phi_{D1}) * \frac{D2}{D2 - D1} \tag{2.7}$$

Having found the amplitude and phase of the propagating wave at the end of the plate, these can be converted to real and imaginary quantities and subtracted from the real and imaginary parts of the total field at the end of the plate. Once this has been performed for all of the propagating modes, the remaining field is that due solely to the non-propagating modes.

The above calculation corresponds just to the out-of-plane component of displacement at the surface of the plate. In order to process the in-plane displacement, and the values at any other locations through the thickness of the plate, it is a simple matter just to make use of the known mode shape of the mode (Figure 2.2). Thus for example, the amplitude of the out-of-plane displacement at a quarter depth in the plate is taken to be the known amplitude at the surface multiplied by the ratio of the amplitudes of the mode shape at quarter-depth and surface. When processing the FE results, an alternative approach was to perform the complete phase extrapolation separately at each depth, since the signals were monitored at all depths at the remote locations. This achieved the same results, confirming agreement between the mode shapes in the FE simulations and those predicted by DISPERSE.

2.7 Results

2.7.1 Below A_1 cut-off frequency

Figure 2.12 shows a comparison of the analytical (Le Clézio model [69]) and the Finite Element predictions of the amplitudes of the reflection coefficient of the A_0 mode and the "mode conversion coefficient" of the A_1 mode when the A_0 mode is incident at the free edge of an aluminium plate. The reflection coefficient here is calculated from the out-of-plane component of the displacement at the surface of the plate (at location A in the FE models), and is defined by the ratio of the amplitude of the displacement of the reflected wave to that of the incident wave. This detail is unimportant when considering the A_0 mode, because the identical reflection coefficient would be indicated by considering any component or depth-location of the displacement; however it will become essential information when considering the A_1 mode because the mode shapes of the A_1 mode are different from those of the incident A_0 mode. Furthermore, it should be emphasised that neither the A_0 nor the A_1 coefficient indicates directly the coefficient of the reflection of energy; the A_0-A_0 energy reflection coefficient is given by the square of the value reported here, while the A_0-A_1 mode conversion coefficient would require a calculation accounting for all of the field through the thickness of the plate. The FE coefficients were calculated in the frequency domain, that is to say the amplitude frequency spectrum of the reflected signal was divided by that of the incident signal. This required a number of simulations with different centre frequencies in order to cover the bandwidth of the plot.

Very good agreement is found in Figure 2.12 between the two methods across the full bandwidth, thus confirming consistency in the methodologies of the two techniques. As would be expected, only the A_0 mode is present at frequencies below the A_1 cut-off frequency, and its reflection coefficient is unity. As the frequency is increased above the cut-off, it can be seen that the amplitude of A_0 initially decreases while the amplitude of A_1 increases; then later A_0 rises again. These trends have also been demonstrated experimentally using a water-coupled piezo-electric source transducer and an air-coupled capacitive receiver transducer; full details of that setup and results are given in [69].

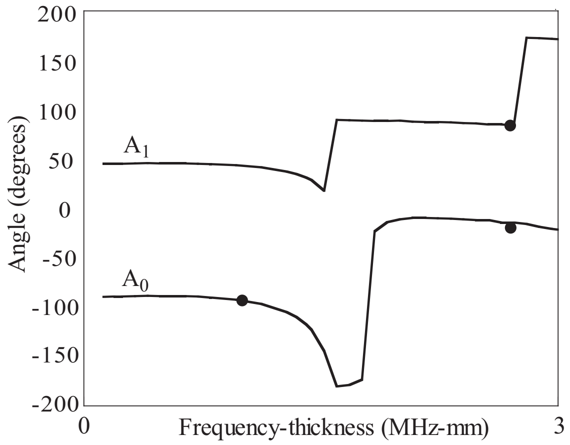

Figure 2.13: Predictions of the phase of the reflected A_0 and A_1 modes at the end of the plate when the A_0 mode is incident. Solid lines are analytical solution (Le Clézio model), filled circles are FE results. The values are the difference between the phase of the out-of-plane displacement of the reflected mode and that of the incident mode.

Figure 2.13 shows the change of phase of the two propagating modes as they are reflected or mode converted at the end of the plate. The phase was calculated from the out-of-plane component of displacement at the surface of the plate. Thus if the incident mode has its phase set to zero at the moment it arrives at the end of the plate, then the plotted phase is that of the reflected or mode converted mode at the moment it leaves the end of the plate. The sign convention is that negative angles denote a phase delay. Very good agreement is again found between the analytical and the FE predictions.

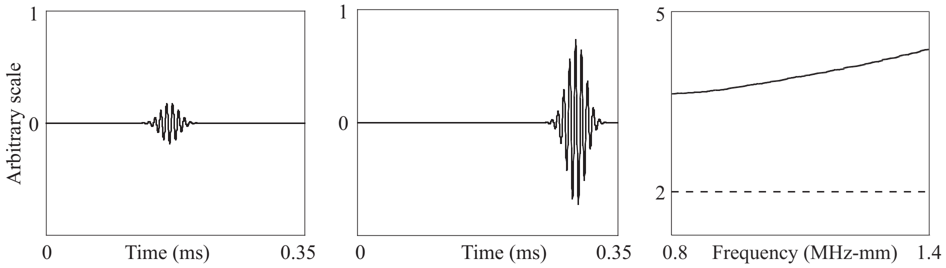

(a) incident mode **(b)** end of plate **(c)** ratio (b)/(a)

Figure 2.14: Prediction of the enhancement of the displacements at the end of the plate caused by the non-propagating modes: (a) incident A_0 mode; (b) signal at end of plate, consisting of incident and reflected A_0 and non-propagating modes; (c) ratio (b)/(a) (solid line) and expected ratio (b)/(a) (dashed line) if there were no non-propagating modes. All results are out-of-plane component of displacement at surface of plate, using signal with centre frequency of 1 MHz-mm.

Figures 2.14(a), 2.14(b), and 2.14(c) show Finite Element predictions which illustrate the extent to which the displacements at the end of the plate are enhanced by the contributions from the non-propagating modes. For simplicity the illustration is based on predictions made using a signal with centre frequency-thickness equal to 1 MHz-mm, when the only propagating mode is A_0. The incident wave was sampled by monitoring the out-of-plane component of the displacement at the surface of the plate at location A of Figure 2.7, and this is shown in Figure 2.14(a). Figure 2.14(b) then shows the same component of displacement at the end of the plate (surface of plate at location C). If this study had been carried out on the reflection of plane bulk waves from the free surface of a semi-infinite half-space, then the amplitude of the signal in (b) is expected to be exactly twice that of the signal in (a). However the ratio of these amplitudes, shown in the frequency domain in Figure 2.14(c), is clearly very much more than two. The additional displacement amplitude is that of the non-propagating modes. Similar enhancement of the displacements is found at frequencies above the A_1 cut off frequency, but for brevity such cases are not shown here.

Further illustration of these enhanced displacements is developed in Figure 2.15. This shows the total displacement field through the thickness at the end of the plate at 1 MHz-mm. The field comprises the sum of the incident and reflected propagating modes and the non-propagating modes. The values are scaled such that the amplitude of the out-of-plane surface displacement of the incident A_0 mode is unity. Each of the two components of the displacement is plotted without phase information, that is to say the displacement profile is shown at the instant during the harmonic cycle when it has its maximum value at the surface of the plate. Excellent agreement is found between the analytical solutions, the FE predictions and the experimental measurements.

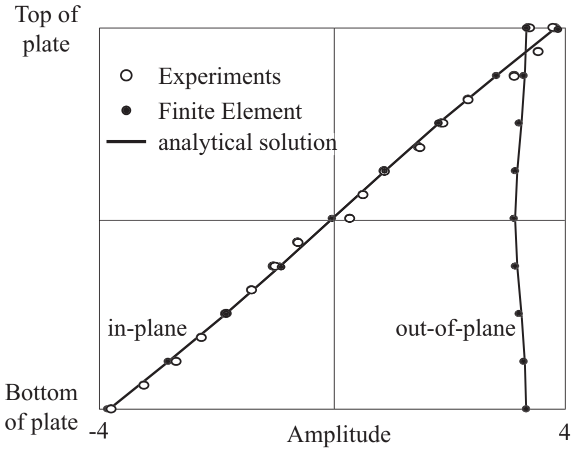

Figure 2.15: Total displacement field (all modes) through the thickness at the end of the plate at 1 MHz-mm, when the incident A_0 mode has unit amplitude out-of-plane displacement at plate surface. Solid lines are analytical solution (Le Clézio model), filled circles are FE results, empty circles are experimental measurements.

Results making use of the method and described in Section 2.6 to remove the propagating modes from the total displacement field of Figure 2.15 are now presented, leaving the contribution due just to the non-propagating modes. The results thus processed are shown in Figure 2.16. Again the amplitudes are scaled to correspond to unit amplitude of the out-of-plane surface displacement of the (removed) incident A_0 mode. Also, the displacement components are shown without phase information, as in the preceding figure. This process was applied separately to the FE and the experimental data, and both are shown in the plot: FE predictions by filled circles and experimental measurements by empty circles. The sum of the non-propagating modes from the analytical model are also shown here, plotted as solid lines. In general there is very good agreement between these results, although the measurements show some scatter near the surface of the plate. This scatter comes from the difficulty measuring near a corner with the laser. The diffraction of the laser beam caused by the corner of the plate means that not the full beam (or full displacement) is received by the interferometer but only a part of it.

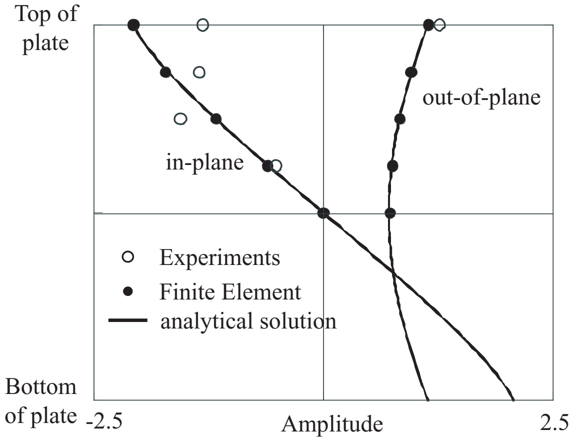

Figure 2.16: Displacement field corresponding to Figure 2.15, but after removal of the incident and reflected propagating modes, leaving just the non-propagating modes. Solid lines are analytical solution (Le Clézio model), filled circles are FE results, empty circles are experimental measurements.

An interesting outcome of the study at this particular frequency is that the non-propagating wave field is dominated by the A_1 non-propagating mode. This is confirmed by examining the results of the analytical model, revealing that the displacement amplitudes of the A_1 non-propagating mode are more than one order of magnitude larger than those of any other non-propagating mode. Indeed plots of the in-plane and out-of-plane displacement mode shapes of A_1 can be practically overlaid on Figure 2.16.

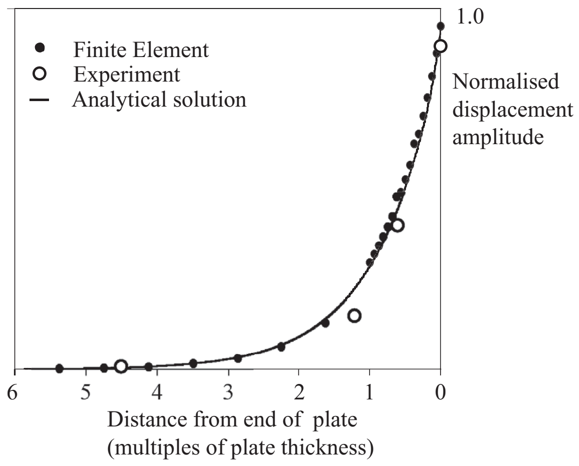

Figure 2.17: Out-of-plane displacement field of the non-propagating modes in the vicinity of the end of the plate, after removal of the incident and reflected A_0 mode, at 1 MHz-mm. Solid line is analytical solution (Le Clézio model), filled circles are FE results, empty circles are experimental measurements.

A similar approach was applied to the displacement field along the top surface of the plate, in the vicinity of the end (location B). After applying the processing to remove the displacements of the incident and reflected A_0 modes, the Finite Element predictions and the experimental measurements of the non-propagating modes field are shown in Figure 2.17. The plot shows the out-of-plane displacement, the amplitude corresponding as before to unit amplitude of the incident mode. Once again there appears to be good agreement between the Finite Element and the experimental results. The decay of the non-propagating modes within about 5 plate thicknesses of the end of the plate is clearly demonstrated. Also shown in the figure, by a solid line, is the decay profile of the A_1 non-propagating mode, taken from the imaginary part of the wavenumber from the analytical model (the DISPERSE prediction shows exactly the same shape). This confirms the observation that the non-propagating modes field is well described by just the A_1 non-propagating mode. Indeed it can be seen in Figure 2.4(c) that the A_1 non-propagating mode has much the lowest value of attenuation at 1 MHz-mm, and so any other non-propagating modes present at the end of the plate would have vanishing amplitude within a short distance along the plate.

2.7.2 Above the A_1 cut-off frequency

The behaviour at 2.7 MHz-mm, when both the A_0 and A_1 modes may propagate is now considered. For brevity the field across the end of the plate in this case is only studied.

Figure 2.18 shows the total displacement field through the thickness at the end of the plate. This field comprises the sum of the incident A_0 mode, the reflected A_0 mode, the reflected and mode converted A_1 mode, and all the non-propagating modes. The amplitude scaling and the form of the presentation is exactly the same as was used in the preceding section for the 1 MHz-mm case. The results show very good agreement between the FE and the analytical predictions.

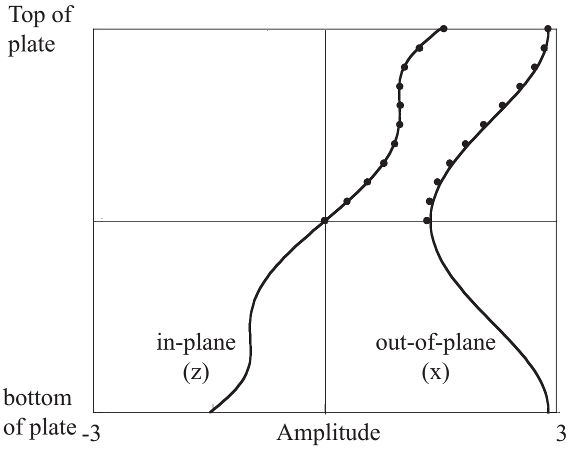

Figure 2.18: Total displacement field (all modes) through the thickness at the end of the plate at 2.7 MHz-mm, when the incident A_0 mode has unit amplitude of out-of-plane displacement at plate surface. Solid lines are analytical solution (Le Clézio model) , filled circles are FE results.

Finally, Figure 2.19 shows the displacement field through the thickness at the end of the plate, after removal of the three propagating modes. This field is thus the sum of the non-propagating modes. Good agreement between the FE and the analytical predictions is demonstrated. The shape of the field here is somewhat more complicated than that for the 1 MHz-mm case, and indeed the analytical study showed that this field is no longer dominated by a single non-propagating mode, but by a combination, consisting predominantly of A_2 and A_3.

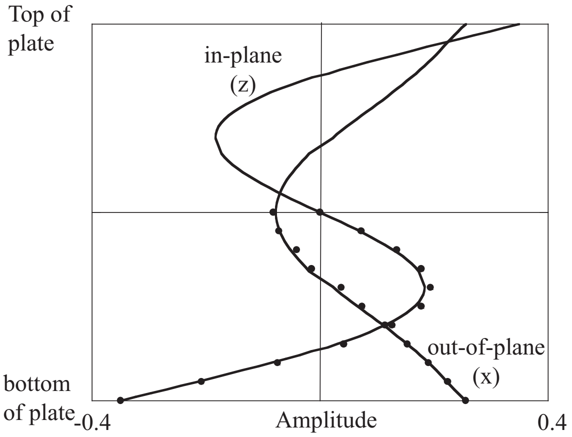

Figure 2.19: Displacement field corresponding to Figure 2.18, but after removal of the incident and reflected propagating modes, leaving just the non-propagating modes. Solid lines are analytical solution (Le Clézio model), filled circles are FE results.

2.7.3 The symmetric mode S_0

As discussed in Section 2.2, the non-propagating modes play a part in the reflection behaviour when the traction-free boundary condition at the end of the plate cannot be satisfied by a superposition of propagating modes. At low frequencies the S_0 mode is dominated by its in-plane displacement and stress components, and these allow the traction-free boundary conditions to be satisfied simply by the sum of the incident and reflected S_0 modes. Thus negligible contributions from non-propagating modes are expected.

Indeed FE studies of the S_0 mode within the frequency range up to the A_1 cut-off showed no evidence of the phenomena which were observed with the A_0 mode. The displacements at the end of the plate were found to be almost exactly twice the values of the incident mode, thus implying that the amplitude of non-propagating modes is negligible. There was also no evidence of a phase change when reflecting from the end of the plate.

Nevertheless, it should be noted that this conclusion only applies in this low frequency range; significant amplitudes of non-propagating modes exist at higher frequencies [7, 38].

2.8 Conclusion

The study has demonstrated significantly enhanced displacements in the vicinity of the end of a plate when the A_0 mode is incident. Analytical predictions, Finite Element simulations, and experimental measurements have been used to investigate these fields at two example values of frequency-thickness, below (1 MHz-mm) and above (2.7 MHz-mm) the A_1 cut-off. Good agreement has been found between the results of all three techniques. Then, by identification of the amplitudes and phases of the propagating modes, it has been possible to remove these from the displacement fields at the end of the plate, thus revealing the fields due solely to the non-propagating modes.

In relation to the motivation for the work, the development of NDE techniques for the inspection of plates, there are two important outcomes from the study. The first is that the reflection of the A_0 mode occurs with a change of phase, for example a 90 degree delay in the more useful 1 MHz-mm case. It may be necessary to take account of this when dealing with the superposition of multiple reflected signals in an area-inspection technique. The second is that the non-propagating modes can enhance the displacement field at some distance from the end of the plate, and this indicates the importance of transducer placement for inspection. In the 1 MHz-mm case the field is enhanced within a region of about 5 plate thicknesses from the end of plate.

It is also useful to know that there should be negligible non-propagating mode generation by reflection of the S_0 Lamb mode from the edge of the plate. This is important information because the S_0 mode is the preferred mode for the test instrument.

Chapter 3

Reflection and scattering of the S_0 Lamb mode from a through-thickness circular defect

3.1 Introduction

The motivation of the work presented in the thesis is the development of a Lamb wave inspection technique for large areas. The primary goal is the detection of corrosion. In more recent years, there has been a large and increasing number of publications relating to the exploitation of Lamb waves for the inspection of flat plates [46, 11, 49, 34, 45, 50, 47, 48, 54, 75, 76, 77, 78] or cylindrical shell [21, 22, 79, 24, 25, 26, 27] structures. Rayleigh waves have also been exploited for the detection and measurement of surface breaking cracks, for example [80, 81], although such an approach is limited to localised detection of small cracks rather than long range inspection. A large proportion of the literature has addressed the practical aspects of the application of guided waves to the inspection of pipes; this is in some ways a simpler problem than inspecting flat plates because the propagation is essentially unidirectional. However, there remains a strong motivation to extend the findings on pipe inspection to the closely related two-dimensional problem of inspecting the area of a plate [4]. This chapter is the first of several where the fundamental S_0 Lamb mode interacts with circular shaped defects, approximating a corrosion patch.

Specifically, it is important to extend the knowledge of the interaction of the Lamb waves with defects from the two-dimensional plane strain studies (see for example [51, 66]) to cases in which the defect is realistically represented as a three-dimensional shape at some location in a plate. Knowledge of this will be essential in order for the area scanning approach to be exploited reliably. This chapter is an initial study, taking a defect with the simplest geometry of a through-thickness hole. Increases in the complexity to address more realistic defects such as part-depth holes representing corrosion loss, and more realistic sources, will be presented in the following chapters. The diameters of the hole relative to the wavelength in this study are representative of the dimensions being considered in the developments reported by Wilcox *et. al.* [4].

Two predictive studies are reported here. The first uses a Finite Element time domain model to simulate the interaction of an incident plane S_0 Lamb wave with a circular hole. The S_0 wave which is reflected straight back from the hole, and the SH_0 wave which is scattered at 90 degrees to the incident direction, are both monitored, and these are used to predict the reflection and scattering functions for a range of hole sizes, frequencies and monitoring distances from the hole. The second approach uses an analytical model to predict the same quantities. This model, whose derivation is summarised, is based on mode superposition. It has been developed by Dr Tomas Grahn [82] who worked in collaboration with the present author. His work will be clearly indicated. Finally a third set of results consists of a limited number of experimental measurements, using a set-up which approximates that of the predictions sufficiently well to validate the trends of the findings.

The work reported in this chapter has been published in the Journal of the Acoustical Society of America [83].

3.2 Mode characteristic and frequency range of interest

Dispersion curves for the well-known Lamb waves in a steel plate (see material properties in table 3.1) are shown in Figure 3.1. These dispersion curves were calculated using the predictive model DISPERSE [5, 6].

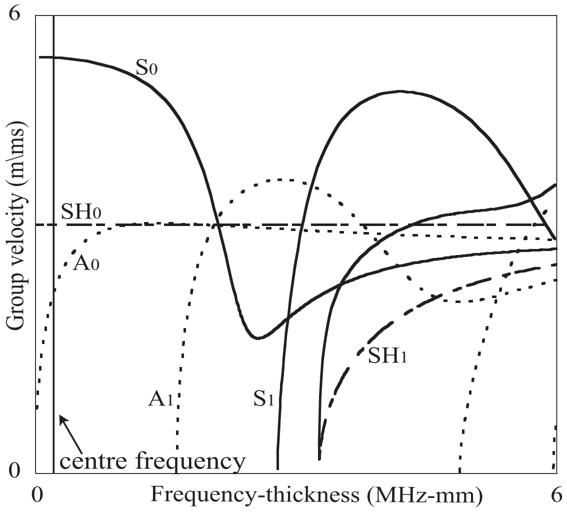

Figure 3.1: Group velocity dispersion curves for Lamb waves in a steel plate.

Density (ρ)	Poisson's ratio (ν)	Young Modulus (E)
7.850 g/cm^3	0.30	210.0 GPa

Table 3.1: Material properties for steel.

The choice of the low frequency mode S_0 for the project has been explained in chapter 1. It has been shown that at low frequency, the S_0 Lamb mode has very little dispersion, which is ideal for long range NDE. However resolution requirements normally force the frequency of choice upwards, so that a compromise is required, and indeed an optimum can be identified logically [84]. Furthermore, another consideration is that increasing the frequency may also increase the sensitivity to defects [51]. A sensible upper limit to this increase is about 1.6 MHz-mm [84], in order to avoid the A_1 cut-off frequency. In fact the work which is presented here is limited to the very low end of the range, that is below about 500 kHz-mm, where the S_0 mode is essentially non-dispersive.

Figure 3.2 shows stress and displacement mode shapes of the S_0 mode through the plate at 100 kHz-mm. The co-ordinate system used from here is different than the system used in the previous chapter. The direction y denotes the normal to the surface of the plate, z denotes the normal to the plane of plane strain, and x denotes the direction of propagation of the wave; displacements and stresses are u and σ respectively. It can be seen here that the mode shapes of this mode at low frequency are extremely simple. This will enable a very simple Finite Element to be employed for the modelling. Within the same frequency range, SH_0 and A_0 can also be present. Since these two waves may exist within the frequency range of interest, it is possible in principle for both of them to be excited by mode conversion when an S_0 wave is incident at a defect.

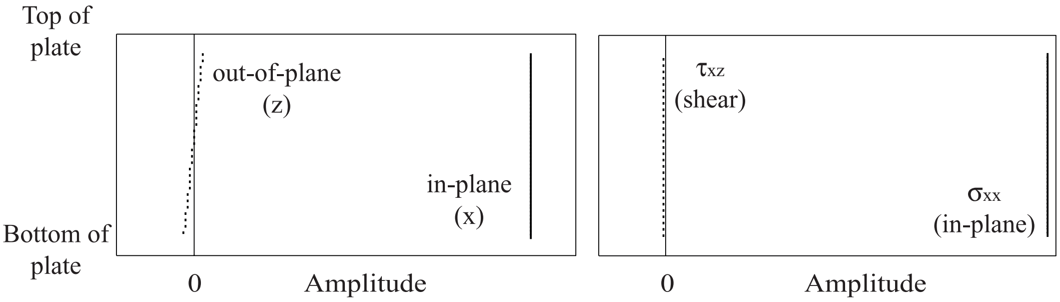

(a) Displacements (b) Stresses

Figure 3.2: Mode shapes of the S_0 mode in an aluminium plate at 100kHz-mm; (a)Displacements and (b) Stresses.

3.3 Procedure for Finite Element simulation

3.3.1 Discretisation

The case which was chosen for the study is sufficiently simple that it can be modelled using a two-dimensional spatial discretisation. Examination of Figure 3.2 shows that the behaviour of the S_0 mode at low frequency is essentially that which is described by simple membrane theory. Propagation of this wave in a plate can therefore be modelled using plane stress membrane Finite Elements, the elements lying along the neutral axis of the plate. Such an approach has similarly been used to model the L(0,2) mode in pipes [26]. Clearly the through-thickness hole can be introduced in such a model, although it should be noted that future chapters will present development of this work to part-depth holes and this will require a genuinely three-dimensional discretisation. The membrane elements can also correctly represent the propagation of the SH_0 wave and so mode conversion between the incident S_0 wave and scattered SH_0 waves can be predicted.

There are two limitations of the membrane model, but fortunately neither invalidates this particular study. The first is that it cannot represent the propagation of the S_0 mode at higher frequency, that is in its dispersive region; therefore at all frequencies the wave propagates at the velocity which it has at zero frequency. The second is that it cannot represent the propagation of the A_0 mode. However the A_0 mode is never excited when the S_0 wave arrives at the hole, the reason being that all of the features of the geometry and of the incident wave are symmetric with respect to the mid-plane of the plate.

The Finite Element modelling was performed using the program FINEL which was developed at Imperial College [72] and already discussed in section 2.5. The membrane elements which were used were four-noded quadrilaterals with 2 degrees of freedom (x, y displacements) at each node, so the solution was performed in the two-dimensional xy plane. Figure 3.3 illustrates the spatial domain, including detail of the mesh around the hole.

An interesting issue worth mentioning here is how best to design the mesh around the hole. A smooth surface around the hole is most easily defined by designing the whole mesh in a radial form, rather like a spider's web (see Figure 3.4(a)). Using this type of mesh raised a problem. Because each element is different to its

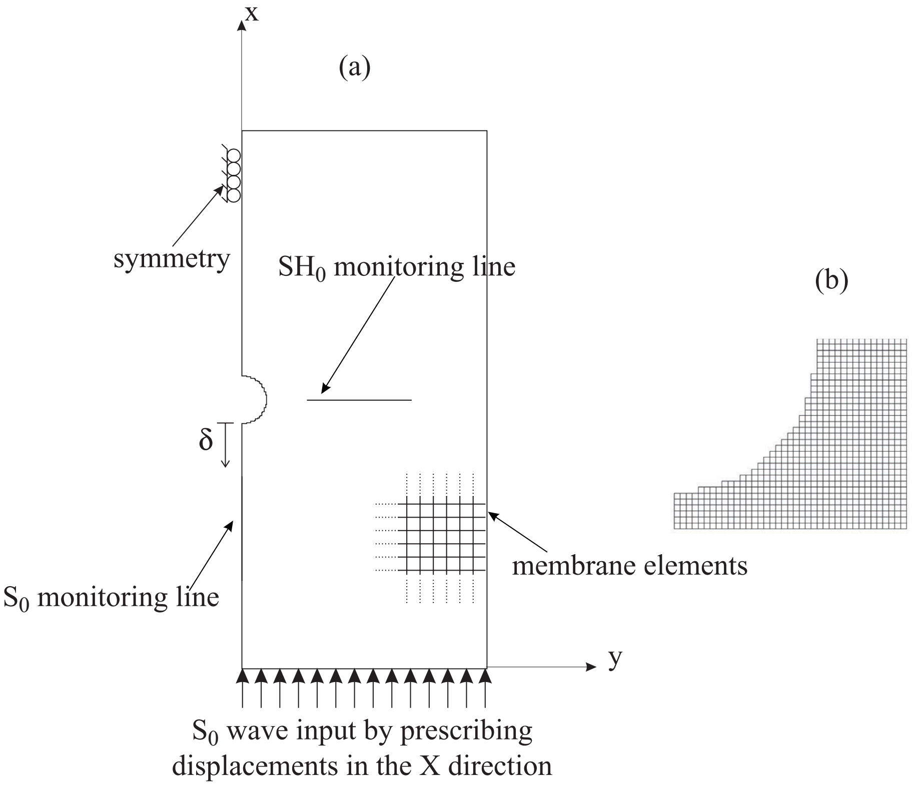

Figure 3.3: (a) Schematic illustration of Finite Element spatial discretisation for the plate and (b) Mesh details around the hole.

neighbour, the energy does not propagate completely from one element to the next but is scattered and steered a little. Another alternative is to introduce different shapes of elements in the locality of the hole, including triangular elements at the edge (see Figure 3.4(b)). However the author's experience has shown that the most satisfactory behaviour is obtained by maintaining identical element sizes and shapes throughout the model. The rather crude approach of simply omitting elements which is illustrated in Figure 3.3 gives the level of accuracy needed throughout the study and is therefore believed to be an appropriate choice.

The same spatial and temporal criteria as described in chapter 2 were used:

$$\lambda_{min} \geq 8\Delta x, \tag{3.1}$$

for the spatial discretisation and:

$$\delta t \leq 0.8\frac{\Delta s}{c} \tag{3.2}$$

for the temporal discretisation.

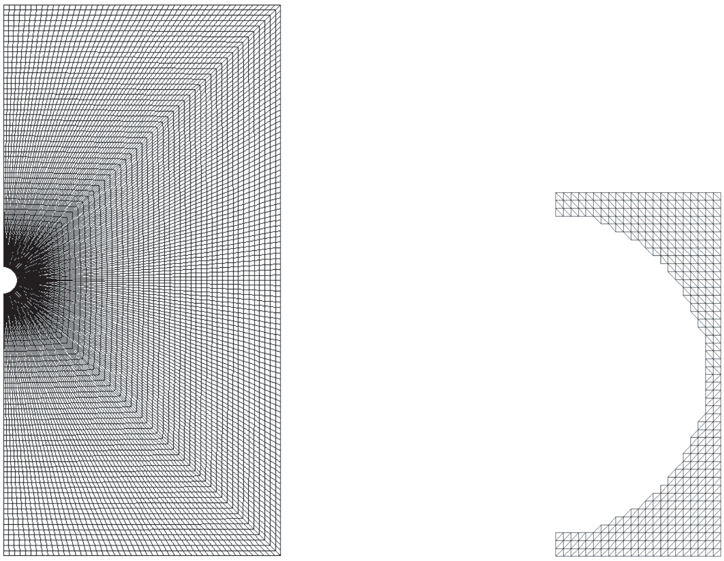

(a) (b)

Figure 3.4: (a) Portion of mesh where a circular hole is present, using 4-noded membrane deformed elements; (b) portion of mesh using triangular elements.

3.3.2 Simulations

The plate which was modelled was 600 mm wide and 1200 mm long. Since the membrane element models waves which are perfectly non-dispersive, the thickness of the elements has no effect on the predictions and so was set arbitrarily. A circular hole was introduced by removing elements from the mesh, as discussed above, and illustrated in Figure 3.3. The dimensions of the plate were chosen to be large enough to avoid the unwanted edge reflections and also to be able to separate in time the reflected signals from the input signals. The length of each element was chosen to be 3 mm, the spatial criterion of equation 3.1 being controlled in this case by the SH_0 mode which has the shortest wavelength. Thus, approximately 10 elements were present per wavelength of SH_0 at 100 kHz. Symmetry was assumed along the x axis through the centre of the hole, so that only one half of the plate had to be modelled (Figure 3.3). The model was repeated for different sizes of hole, its diameter varying between 1 and 3 wavelengths of S_0 at 100 kHz (one wavelength is approximately

55mm).

The S_0 mode was excited by prescribing nodal displacements in the x direction along the whole edge of the plate, as shown in the figure. The input signal consisted of a five-cycle narrow band tone burst, defined by a sine wave modulated by a Hanning window function. The frequency of the tone was 100 kHz. The propagation of the plane wave across the plate was then simulated by the time marching algorithm.

Following the interaction of the S_0 wave with the circular hole, the scattered S_0 and SH_0 waves were received by monitoring the displacements at two series of nodes shown in the figure. The first series of points was along the axis of symmetry (defined by $y = 0$), in order to extract only the S_0 wave which was reflected from the hole. The displacements in the x direction were monitored here, so that the time trace showed the input S_0 signal on its way to the hole, then the reflected S_0 signal returning. Due to the symmetry, there cannot be any SH_0 wave on this axis, so it was never present in these received signals. The second series of points was along a line at 90^o to the hole, and once again the displacements in the x direction were monitored here. The purpose of these monitoring points was to detect the SH_0 wave which was scattered in this direction. Thus the time traces at these points showed the incident S_0 plane wave passing through, then the scattered SH_0 wave. In general an S_0 wave is also scattered in this direction but this was not received because it has negligible displacements in the x direction.

3.4 Analytical model

In this section an analytical model developed by Dr Tomas Grahn [82], suitable for full three-dimensional predictions, is summarised. This model was part of his PhD and was developed during a placement period when he worked at Imperial College in collaboration with the present author. Therefore, it is appropriate to compare it with the work presented in this thesis. This approach should apply not only for the low frequency range which is of concern in this chapter but also for higher frequencies. Furthermore, it is well configured for further development to the more advanced problems involving part-depth holes.

Analytical approaches for scattering problems in plates are quite rare. Plate theory approaches have been employed by for example McKeon and Hinders [54] to study the scattering of Lamb waves by a through hole in a plate using Kane-Mindlin higher order plate theory. Scattering of flexural waves by circular holes have been treated by Norris and Vemula using Kirchoff plate theory [75] and Mindlin theory [76]. A combined FE and mode expansion technique has been used by Chang and Mal [77] to investigate the scattering of Lamb waves by a circular hole, with or without edge cracks. In their paper the far-field is expanded in propagating Lamb modes and the region around the hole is modelled using FE.

In this particular study the incoming field is defined, as discussed in the preceding section, to be a plane S_0 Lamb wave mode. However in the general case this analytical model is applicable to other forms of incident field, such as fields that include several symmetric Lamb wave modes or Lamb waves which have been generated from a point source. The same principle would also apply for an anti-symmetric incoming field.

The geometry for the 3-D problem is given in Figure 3.5. The coordinate system is placed at the centre of the hole and the XY plane is the mid-plane of the plate. The coordinate z denotes the thickness of the plate.

Since only symmetric incoming fields are considered, and since the scatterer is symmetric, the scattered field also consists solely of symmetric modes [11]. Thus, the scattered field is represented by only the S_0 Lamb mode and the SH_0 mode. One way of expressing Lamb wave modes is via a potential function as shown in Achenbach and Xu [78]. The SH modes can be expressed in a similar way as the Lamb modes with the aid of a different scalar potential function [78]. Then, in order to find the different parts of the wave field, solutions of these scalar potentials have to be found.

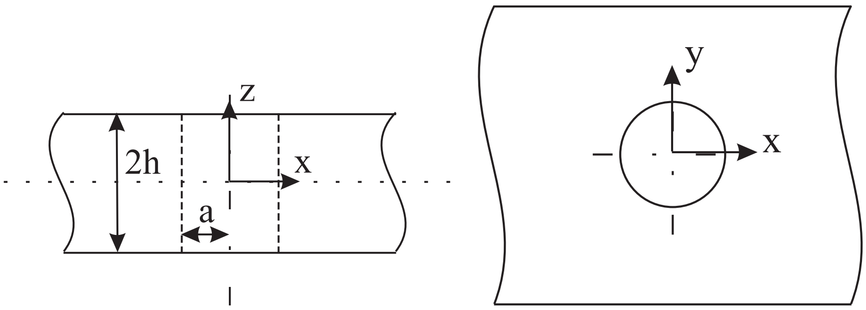

(a) Side view **(b)** Top view

Figure 3.5: Geometry of the analytical problem with: (a) side view and (b) top view.

The expansions for the stresses for the incoming field, needed for the boundary conditions, are calculated using Hooke's law. The total stress distribution in the plate is given by the sum of the incoming field and the scattered field, i.e. $\boldsymbol{\sigma} = \boldsymbol{\sigma}^{\text{inc}} + \boldsymbol{\sigma}^{\text{scat}}$. Next the expressions for the stresses are used to calculate the expansion coefficients for the scattered field by applying the boundary conditions.

The boundary conditions for the stress free hole, expressed in cylindrical co-ordinates are

$$\sigma_{rr} = \sigma_{r\theta} = \sigma_{rz} = 0, \quad r = a,\ -h < z < h,\ 0 < \theta < 2\pi. \tag{3.3}$$

To obtain a system of equations for the expansion coefficients of the scattered field, the boundary conditions (3.3) and the expressions for the stresses are employed. The boundary conditions are projected onto some complete set of orthogonal functions in order to get rid of the dependence on the z and θ co-ordinates. The orthogonality of the θ-dependent functions, $f_m(\theta) = e^{im\theta}$, suggest that they are suitable as projection functions in the θ-direction. For the z-dependency there is no obvious choice of projection functions, at least not for the Lamb wave part. However, it is always possible to project onto any complete orthogonal set of functions.

The displacements in all of the examples given below are calculated at the mid-plane of the plate ($z = 0$). However, as discussed earlier, the displacements of the S_0 and SH_0 modes are more or less uniform through the plate thickness.

To produce results in the time domain which can be compared with the corresponding results given by the Finite Element calculations, an inverse Fourier transform is employed

$$\boldsymbol{u}(t) = \int \boldsymbol{u}(\omega) F(\omega) e^{-i\omega t} d\omega. \tag{3.4}$$

Here $F(\omega)$ is the frequency spectrum, in this case given by a Hanning window. In order to have almost identical input signals to the Finite Element studies, the frequency spectrum $F(\omega)$ which was used was taken from an FFT of the input signal in the Finite Element model.

3.5 Experimental procedure

An experimental programme was conducted in order to provide some practical validation of the findings of the Finite Element and analytical modelling work. It is clearly a very difficult task to generate a plane S$_0$ wave across a significant width of a plate and so this was not attempted. Instead the S$_0$ Lamb wave was generated at a single location, approximating a point source, at a significant distance from the hole. Thus the experimental configuration was not precisely that which was modelled. Nevertheless, it is believed that this approximate approach was useful and sufficiently accurate to validate the trends and magnitudes of the cases which were predicted. The case of the point source will be considered in later modelling.

Six 1200 mm x 1200 mm x 1 mm thick steel plates, each with a through-thickness circular hole in the middle, were used for the experiments. The plates and experimental set-up are illustrated in Figure 3.6(a). The diameters of the holes varied between approximately 1 wavelength and 2.5 wavelengths of the S$_0$ wave at 100 kHz centre frequency (between 60 mm and 132 mm). The S$_0$ wave, generated using a Wavemaker (Macro Design Ltd, UK) instrument, was excited at one end of the plate by a 5-cycle 100 kHz tone burst modified by a Hanning window.

Although the S$_0$ mode is the simplest of the Lamb waves, and is non-dispersive

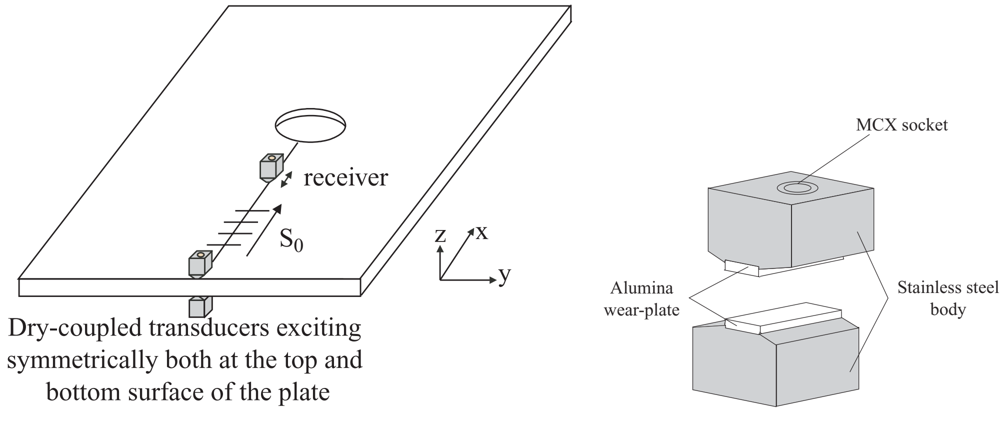

(a) Experimental set-up **(b)** Transducer element

Figure 3.6: (a) Experimental set-up; (b) transducer element description.

at low frequencies, it is actually very tricky to work with experimentally. A classic excitation method consists of creating perturbations on the surface of the plate [85, 86, 87, 88, 89]. Typically, stresses can be induced at the surface of the plate by an ultrasonic transducer sending waves through a coupling medium such as water between it and the plate. By setting a specific angle of the incident wave with respect to the plate, a selected Lamb mode can be excited. However, S_0 at low frequency has very little out-of-plane displacement and so it is not easily excited, whereas A_0 is very readily excited. Therefore, even when the angle of the incident wave is set to excite the S_0 mode, it only excites it weakly, and at the same time the spatial bandwidth of the excitation field is such that some unwanted A_0 is also excited. Consequently it was decided to make use of dry contact transducers (see Figure 3.6(b)) [90, 91] both to excite the S_0 wave and to receive the reflected and scattered signals. These piezoelectric transducers do not need coupling and impose a shear stress in the region of contact, therefore preferentially exciting modes with significant in-plane displacements at the surface of the plate.

These transducers are small (approximately 14 mm long) compared to the wavelengths used in this study (typically 55 mm), and so can be considered here to be point sources. In fact, although they preferentially excite the S_0 and SH_0 modes, they do excite some of the A_0 mode, so care is still needed in order to make use of them. The S_0 mode and the A_0 modes are excited along one axis (both backwards and forwards) and the SH_0 mode is excited in the perpendicular axis. Differentiation of the S_0 and A_0 modes may most easily be achieved by choosing sufficiently long propagation distances that their signals separate. A further step to minimise the excitation of A_0 is to use a pair of transducers working in parallel on opposite sides of the plate, as shown in the figure. With this set-up, any remnant A_0 can be the result only of an imbalance of the pair of transducers. The SH_0 mode is more easily separated by selection of the orientation of the transducer. Of course these arguments apply equally to the use of the transducers for excitation or reception.

Along the line of primary interest, corresponding to the axis of symmetry in the Finite Element model, and shown in the illustration in 3.6(a), the measurements contain S_0 and any remnant A_0 and SH_0. These can easily be separated in time in a plate of this size and so it was possible to record reliably just the S_0 reflection. Figure 3.7 shows a typical measured time history at a location on this axis and 390 mm from the hole. This shows the incident S_0 mode on its way to the hole, which was in this case 108 mm in diameter, and the S_0 reflection from the hole. To calculate the reflection ratio in the frequency domain, the frequency spectrum of the reflected S_0 signal was divided by that of the incident S_0 signal, yielding a reflection ratio as a function of the frequency within the bandwidth of the windowed toneburst. In some cases reflection ratios were also calculated using time domain values. This was done by calculating the envelope of the time signal, by taking the Hilbert transform, then simply dividing the value of the reflection peak by that of the incident peak. Given that the signal has rather a narrow frequency band, such an approach gives a reasonable estimate of the reflection ratio for the centre frequency.

There is negligible attenuation due to damping in a steel plate at this frequency. However there is a signal decay due to beam spreading, and indeed this will be discussed later when examining the detail of the predictions. The beam spreading loss in the experiments was estimated by observing the reduction in the measured reflected signal as a receiver was moved away from an edge of the plate, and assuming

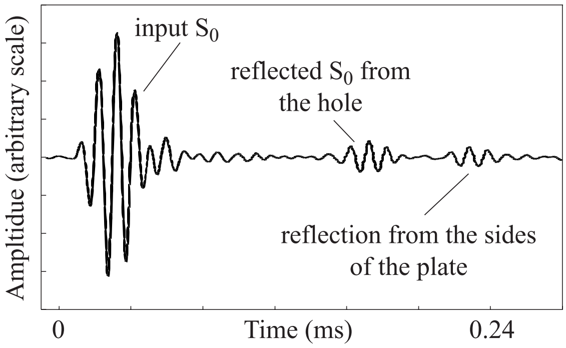

Figure 3.7: Example of measured time signal at 390 mm away from the edge of the hole; the hole is 108 mm in diameter.

the decay to be a logarithmic function. This gave an attenuation of 8.2 dB/m. This figure was used to compensate the experimental measurements for comparison with the predictions. Essentially the compensation required the received signal to be compared with the amplitude of the incident signal when it arrived at the hole, rather than when it passed the receiver on its way to the hole.

3.6 Results and discussion

The results of the Finite Element, analytical and experimental studies are presented and compared here. First the direct reflection of the S_0 wave from the hole is considered, then the SH_0 wave which is scattered at 90 degrees from the hole, and then finally, the variation of the wave fields with angular position around the hole is presented.

3.6.1 S_0 direct reflection from the hole.

Figure 3.8 shows a comparison between a typical time history predicted by the analytical model with that predicted by the Finite Element simulation. The signal is monitored at a location which is 390 mm from the edge of a hole, and the hole is 114 mm in diameter. Excellent agreement is found between the two curves. The figure also shows clean separation of the signals, so allowing reliable extraction of the incident and reflected parts for the calculation of the reflection ratio functions.

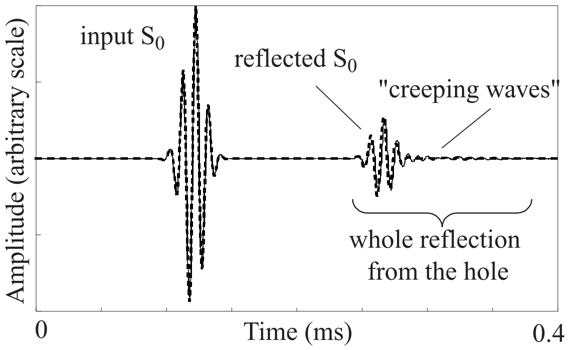

Figure 3.8: Comparison between typical Finite Element (solid line) and analytical (dashed line, Grahn model) time traces of direct S_0 reflection for a hole 120 mm in diameter and monitored at 390 mm from the edge of the hole.

The reflection ratio was initially calculated using the frequency domain technique, that is by dividing the frequency spectra of the reflected part of the signal by that of the incident part. The curve thus obtained displays amplitude (reflection ratio) against frequency. A convenient way to present the results for different hole diameters is to normalise them to the wavelength of the incident mode. This has been done in Figure 3.9 using results from the analytical predictions, the Finite Element predictions and the experimental measurements, and in each case for the centre frequency of 100 kHz. Very good agreement of the trend is obtained in all three sets of results, and it is particularly noteworthy how well the experimental points agree with the predicted points.

However there are some differences in detail between the two sets of predictions. It is believed that the principal reason for the differences is in the Finite Element discretisation around the hole. Since the surface of the hole is not smooth, but composed of a series of steps, the propagation of waves around the hole (these will be discussed shortly) is significantly affected by the detail of the mesh [67]. This was confirmed by repeating one of the cases with different discretisations of the same hole: the outcome was that there were indeed some variations of the results which were of the appropriate magnitude. On the other hand, a refined mesh, yet which

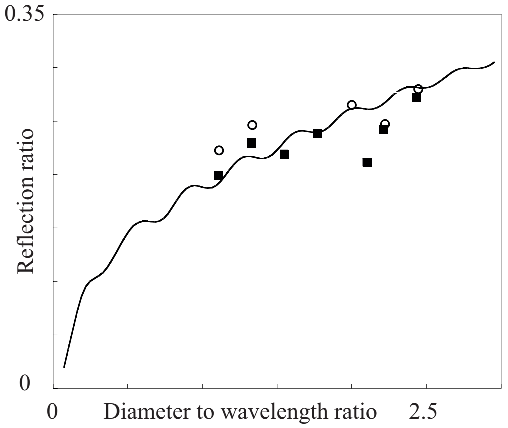

Figure 3.9: Predicted variation of S_0 reflection ratios at 390 mm away from the hole with hole diameter normalized to wavelength; comparison between experimental (circle), Finite Element (filled square) and analytical (solid line, Grahn model) results.

retained the identical step profile of the hole, gave identical results, confirming that the mesh itself was sufficiently fine for the correct propagation of the waves. This issue could in principle be pursued using significantly refined meshes, but it was decided not to pursue this. The computation effort for these calculations is already large, and in any case this focus would go beyond the needs of the practical application which motivates the study.

The upward trend of the reflection function is as expected, but it also exhibits undulations which need some explanation. Additionally, it will be important to examine how this function would change for different receiver positions. Each of these issues will be examined in turn, starting with the latter.

In order to see how the reflection function varies with the distance of the receiver from the hole, Finite Element predictions of the reflection ratio were made at a series of points along the axis. In each case the processing was performed using the time domain method which had the benefit of smoothing the undulations out of the signal, and so clarifying the comparisons for different distances. The basis of this smoothing will be studied later.

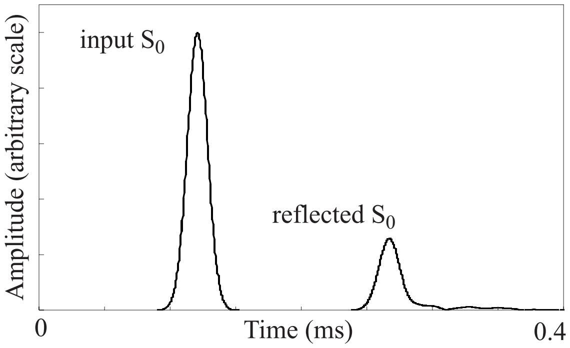

Figure 3.10: Hilbert envelope of the signal from the Finite Element results in Figure 3.8.

Figure 3.10 represents the Hilbert transform of the signal in Figure 3.8. Following the explanation in section 3.5, the reflection ratio was extracted from the figure by dividing the peak amplitude of the S_0 direct reflection by the maximum amplitude of the input S_0 wave. This was repeated for a range of distances from the hole and for three different sizes of hole. The results are presented in Figure 3.11. As expected, the reflection ratio increases with diameter and decreases with distance from the hole.

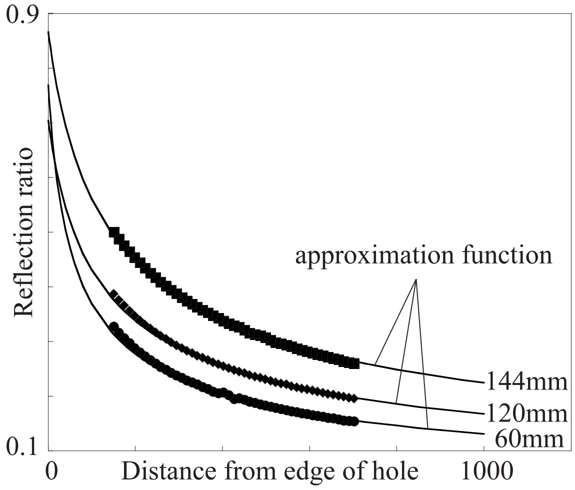

Figure 3.11: Finite Element predictions (symbols) of S_0 reflection ratio plotted as a function of distance away from the edge of the hole, for three different diameters of the hole. Values are taken from the Hilbert envelope calculation. Lines show the approximation function which has been fitted to just one point for each hole.

If the hole is assumed to act as a cylindrical emitter of the reflected waves, then it is possible to fit a simple decay function to these curves to describe this beam spreading behaviour. The ideal spreading function of cylindrical waves is that the amplitude is inversely proportional to the square root of the propagation distance from the source, such that

$$A(\delta) = \frac{A_{refl}}{\sqrt{\delta + \delta_0}}, \tag{3.5}$$

where A_{refl} is a constant related to the amplitude of the wave, δ is the distance from the edge of the hole along the axis of propagation and δ_0 is the distance from the centre of the beam spreading to the edge of the hole. As the centre of the hole is also the centre of the curvature, a logical choice for δ_0 is to set it equal to the radius of the hole. The constant A_{refl} was calculated by fitting this equation to values from the Finite Element results. Each curve required just a single value to calculate its A_{refl}, and in each case this was taken towards the near end of the distribution in Figure 3.11. The approximation functions have been superposed on the Finite Element results in the figure, showing a very good fit.

An interesting correlation is observed if the analytical solutions are re-plotted (same as plotting the approximation function curves) using the axis of the distance normalised to the hole-diameter. Figure 3.12 shows that all the curves plotted in this way are almost overlaid. This means that, at a given distance from the hole measured in multiple diameters, all reflection ratios at a given frequency are the same, whatever the hole size. For example, if the hole diameter is 30 mm, the reflection at 180 mm (6 diameters) away from that hole will be the same as that from a 60 mm diameter hole monitored at 360 mm. Also shown in this plot is that some curves are shorter than others. This comes from the fact that all the data were calculated for the same distance path away from the hole but different cases were normalised to different hole diameters.

Returning to the issue of the undulations, the underlying phenomenon can be shown to be the interference of the signal which is reflected directly from the near side of the hole with a second signal which arrives slightly later. The second signal is much

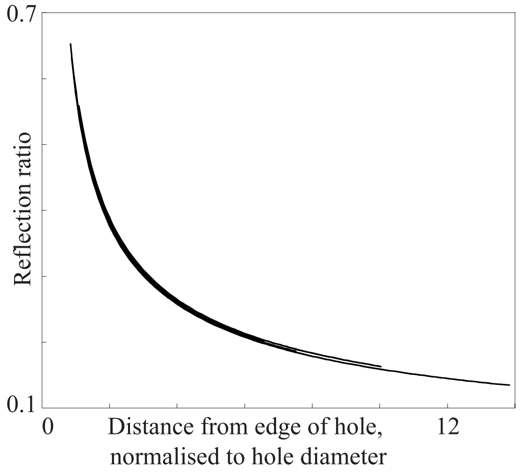

Figure 3.12: Analytical amplitudes plotted as a distance normalised to hole diameter.

smaller than the direct reflection, but nevertheless has an influence on the overall result. The second signal can just be seen following the direct reflection in Figure 3.8, where it is labelled “secondary reflections”. Sources of the secondary reflections include reflected SH_0 waves, which are slower than the S_0 wave, and “creeping wave”, which travel around the circumference of the hole, re-radiating time-delayed signals. SH_0 waves are present directly on the axis, but only with a radial component that decays quickly with the distance (equation 3.5). Creeping waves have been studied quite extensively, albeit usually in plane strain, for example by Nagy *et. al.* [57, 58].

The secondary waves were neglected when the peak of the Hilbert transform of the direct reflection was used to construct Figures 3.11 and 3.12, resulting in smooth distributions. However, they can be taken into account by dividing the spectra of the whole reflected wave signal by the spectra of the incident S_0 wave, using the frequency domain approach. This was done for three diameters of hole, and in each case the reflection ratio was measured at the centre frequency (100 kHz) for several points away from the edge of the hole. The results of this processing are shown in Figure 3.13, exhibiting the undulations which are characteristic of the interference phenomenon. In this plot the undulations are believed to result mainly from the reflected SH_0 waves, because their amplitudes decrease with distance from the hole.

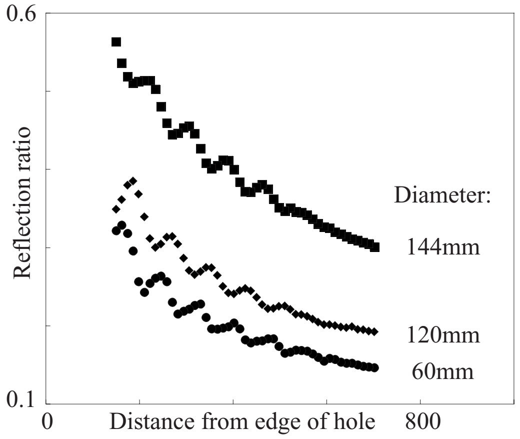

Figure 3.13: Reflection ratio calculated using the whole reflection from the hole, showing influence of the creeping waves. Example for three different diameters: 60 mm (filled circle), 120 mm (filled diamond) and 144 mm (filled square).

3.6.2 SH_0 reflected at 90 degrees from the hole.

A very similar study was performed on the SH_0 mode which is scattered at 90 degrees from the hole. The direction of the scattering and location of the monitoring points is indicated in Figure 3.3.

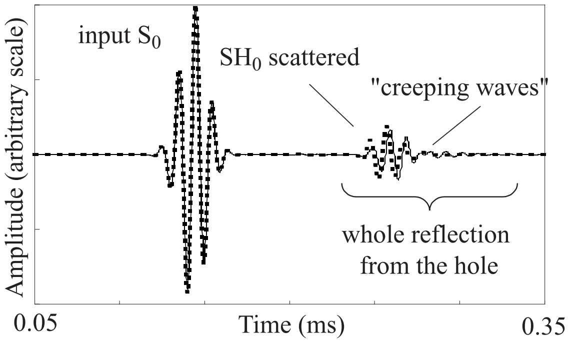

Figure 3.14: Comparison between typical Finite Element (solid line) and analytical (dashed line, Grahn model) time traces of direct SH_0 reflection for a hole 120 mm in diameter and monitored at 234 mm from the edge of the hole.

Figure 3.14 shows typical time domain predictions from the Finite Element and analytical models, and once again there is very close agreement. The predictions were made at 390 mm from the edge of the hole. The Finite Element reflection ratios were calculated from these signals using the frequency domain approach applied to the whole scattered wave signal, and extracting just the value at the centre frequency of 100 kHz. The reflection ratios are plotted against the ratio of hole diameter to wavelength in Figure 3.15. Care should be taken in interpreting the reflection ratio axis, since this relates modes of different types: this ratio expresses the amplitude of the in-plane displacement of the scattered SH_0 wave divided by the amplitude of the in-plane displacement of the incident S_0 wave. Fairly good agreement is found between the Finite Element and the analytical results. As with the earlier work, the differences between the predictions are believed to result from the mesh details around the edge of the hole. Similarly, the undulations are expected to result from the creeping wave behaviour, and indeed this is in evidence in the later part of the signal in Figure 3.14. Experimental measurements were not obtained for this case because it proved not to be possible to avoid unwanted signals due to reflections from the edge of the plate and also the presence of the incident plane wave across the full width of the plate.

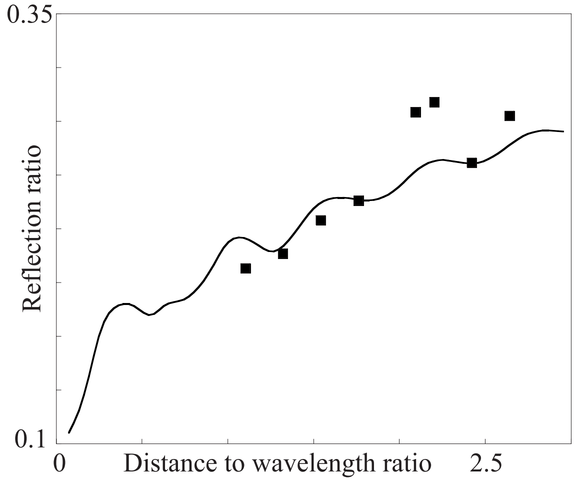

Figure 3.15: Predicted variation of SH_0 reflection ratios at 390 mm away from the hole, with hole diameter normalized to wavelength; comparison between analytical (solid line, Grahn model) and Finite Element (filled square) results at 100 kHz.

Figure 3.16 summarises the results for the scattered SH_0 wave, following the sequence of analysis which was taken earlier for the reflected S_0 wave. It shows precisely the same features: (a) the amplitude of the scattered wave increases with the hole diameter and decreases with the distance from the hole; (b) the decay with distance form the hole can be described well by the cylindrical beam spreading function; (c) if the distance away from the hole is normalised to hole diameter all reflection ratios are approximately the same whatever the hole size; and (d) creeping waves have an effect on the results.

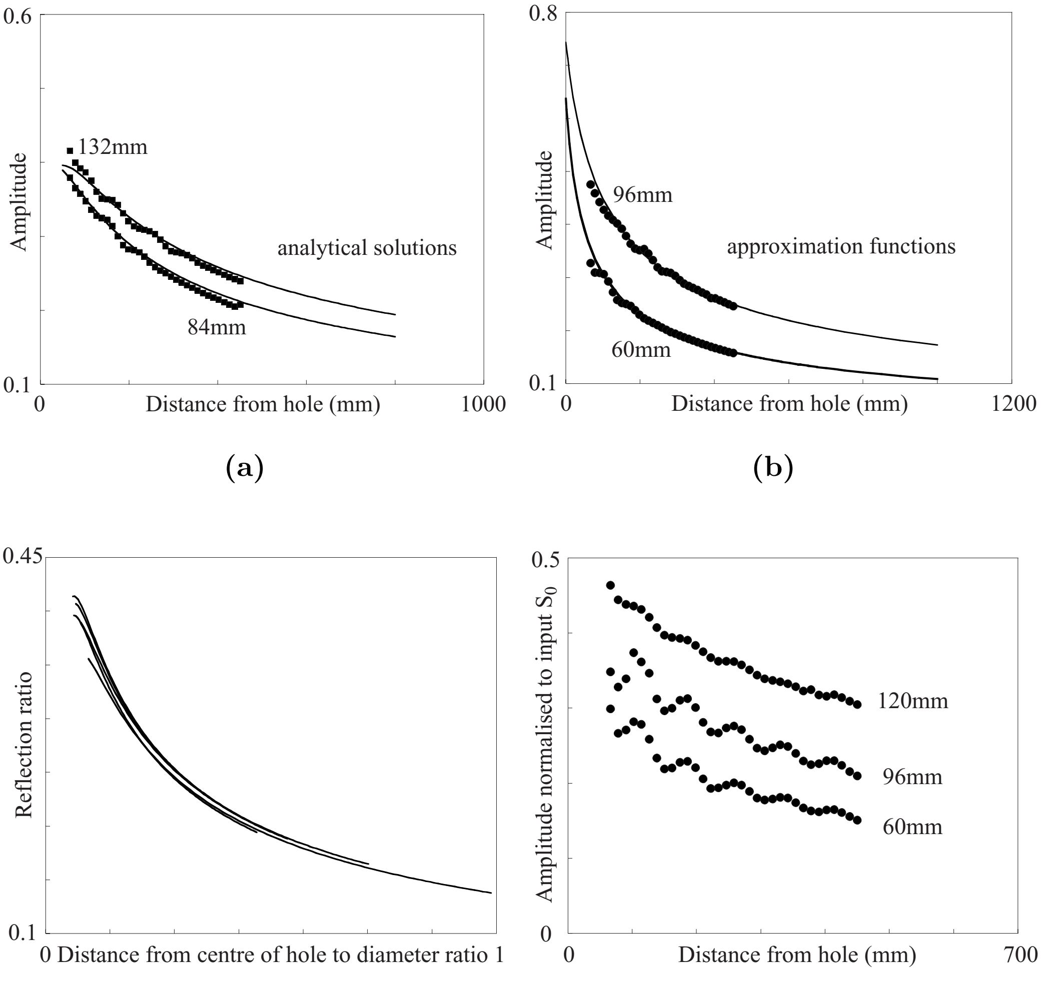

(a) (b)

(c) (d)

Figure 3.16: (a) Comparison between analytical (Grahn model) and Finite Element predictions for the SH_0 amplitude plotted as a function of distance away from the edge of the hole. Values are taken from the Hilbert envelope calculation. For clarity, results are plotted for only two diameters (84 mm and 132 mm), (b) Comparison between results from the S_0 specular reflection for Finite Element and approximation function, (c) Analytical results plotted as distance normalised to hole diameter and (d) Influence of the creeping waves on the scattered SH_0 curves.

3.6.3 Wave field around the hole represented by polar plots

The scattered field around the hole is illustrated well by a polar plot. Figures 3.17(a) and 3.17(b) show the predicted amplitudes of the scattered modes for a hole which is 84 mm in diameter, when the receiver is at a distance of 390 mm away from the edge of the hole. The circumferential axis of the plots corresponds directly to the angular location with respect to the centre of the hole; the origin (180 degrees) corresponds to the direction of the incident wave. The radial axis of the plots corresponds to the magnitude of the displacement.

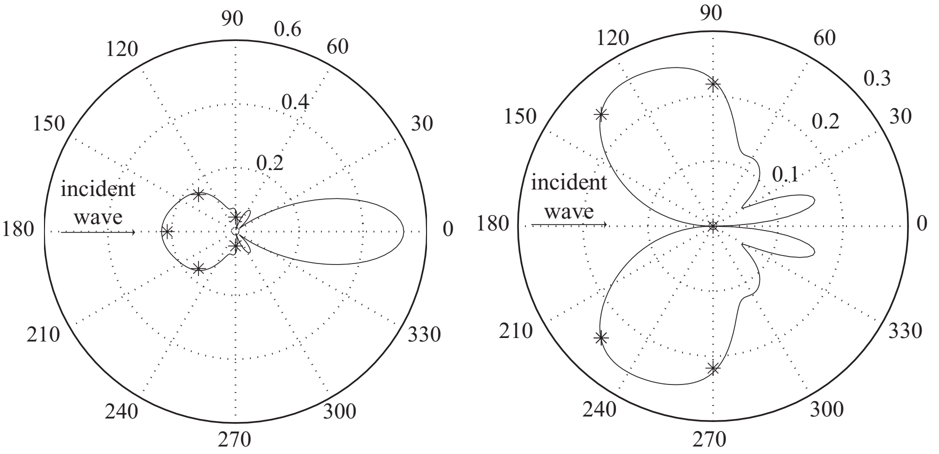

(a) S_0 mode **(b)** SH_0 mode

Figure 3.17: Polar plots comparing analytical (solid line, Grahn model) and Finite Element (asterisk) predictions for a hole 84 mm in diameter, when the wave is received at 390 mm away from the hole. The radial distance in the plots represents the amplitude of the received signal. The S_0 mode is incident at 100 kHz-mm. Plots show scattering of (a) S_0 mode; (b) SH_0 mode.

The dominant displacement components are shown, that is the radial component, u_r (Figure 3.17(a)), for the S_0 mode and the circumferential component, u_θ (Figure 3.17(b)), for the SH_0 mode. The solid lines are calculated from the analytical model developed by Grahn for a single frequency of 100 kHz. Results from the Finite Element models are also included at some specific angles and those points are calculated from the Hilbert envelope of the signal. Very good agreement is found between the two techniques. The reflected S_0 wave is scattered mainly forwards and backwards (at 0 and 180 degrees), while the reflected SH_0 is scattered mainly in the transverse direction. Note that the incoming S_0 wave is not plotted.

3.7 Conclusion

The interaction of a low-frequency plane S_0 wave with a circular through-thickness hole in a plate has been studied using three different approaches: Finite Element simulation, analytical predictions, and experimental measurements. A specific focus was directed on the directly reflected S_0 mode and the laterally scattered (90 degrees) SH_0 mode, and the study was limited to hole diameters in the range of 1 to 3 wavelengths of S_0 at the frequency thickness product of 100 kHz. Good agreement between the three sets of results was obtained. The results show quite high reflection ratios: for example, a 54 mm hole diameter has a specular reflection ratio of 0.27 (approximately -11 dB).

Interpretation of the nature of the S_0 reflection and SH_0 scattering ratios has indicated the same form of the behaviour for each case:

(a) the ratio increases with the diameter of the hole and decreases with distance from the hole;

(b) a single function can be used to express the trend of the ratio for all hole diameters and distances from the hole, by normalising the distance to the diameter of the hole;

(c) the trend of the decay of the ratio with distance from the hole closely follows a cylindrical beam spreading function;

(d) the trend of the ratio is perturbed by small undulations; these are the result of interference with the main signal by re-radiation from creeping waves which travel around the hole.

Chapter 4

Reflection and scattering of the S_0 Lamb mode from a part-depth circular defect

4.1 Introduction

A second study of the interaction of Lamb waves with a circular defect is presented in this chapter. The Lamb wave mode chosen is the S_0 mode in the low frequency-thickness regime. A three dimensional Finite Element mesh is generated, representing an area of the plate with a circular part-depth hole (33 % or 50 % of the plate thickness deep). The specular reflection of an incident S_0 wave is predicted and shows the importance of several factors, including the constructive or destructive interference between the front and the back edge of the hole; the decay in amplitude of the reflected wave; and the generation of "creeping waves" which travel around the hole.

The chapter is in four sections. The first section presents the methodology of the Finite Element modelling; the details of the mesh, and the chosen frequency for the tests, and surveys significant earlier work done by the author on two-dimensional Finite Element analysis of plates with notches. The second presents an analytical model, which is an extension of the model represented in 3.4, for the part-depth hole, and the third section reports results obtained for partial-depth defects (3-D), where investigation has been carried out in order to understand the scatter and discontinuities shown on the reflection coefficient curves. Finally a conclusion is presented, summarizing the results.

Note that no experimental results are attempted in this chapter. In principle, experiments similar to those presented in the precedent chapter could be done, but as the results show the same trend as in the previous chapter, they were not attempted. On the other hand, experimental results obtained with the plate tester device will be compared with predictions in the next chapter.

4.2 Methodology for Finite Element predictions

4.2.1 Frequency range of interest

Figure 4.1(a) shows the group velocity dispersion curves for an aluminium plate. Aluminium was chosen in this case in regard to later experiments that will be presented in chapter 5. Large plates were used in those experiments and they needed to be manoeuvrable. Since steel is much heavier than aluminum, the latter was chosen. The material properties of aluminium are presented in table 2.1.

Figure 4.2 shows the displacement and stress mode shapes for the S_0 Lamb mode at the frequency-thickness product 100 kHz-mm. They are very similar to those for a steel plate presented in chapter 3. They are dominated by the in-plane components. At this frequency regime, this mode is equally sensitive to any type of defect through the thickness of the plate; it has low dispersion; and if the plate is immersed, the attenuation due to leakage is very small (see Figure 4.1(b)). Within the same frequency range A_0 and SH_0 can also be present as was the case in the preceding chapter.

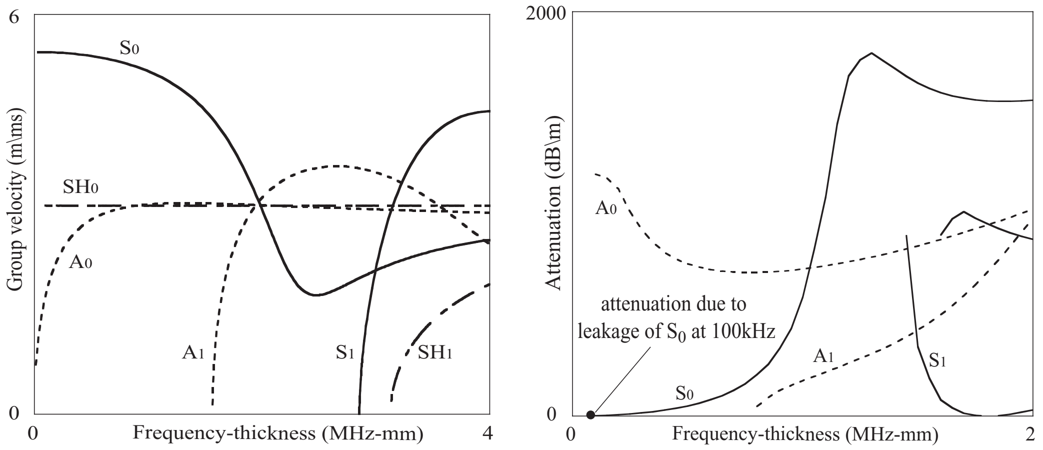

(a) Group velocity **(b)** Attenuation

Figure 4.1: (a) Group velocity dispersion curves for Lamb waves in an aluminium plate; (b) attenuation dispersion curves for for lamb waves in the system water-aluminium.

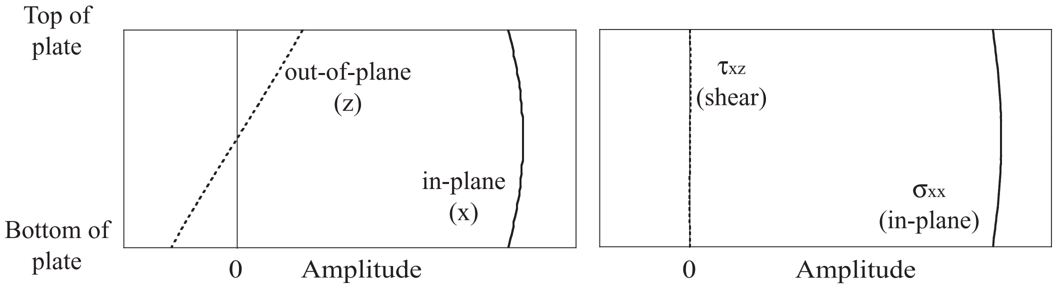

(a) Displacements **(b)** Stresses

Figure 4.2: Mode shapes of the S_0 mode in an aluminium plate at 100kHz-mm; (a) Displacements and (b) Stresses.

4.2.2 Plates with a notch (previous work)

A previous piece of work which forms a necessary understanding for the part-depth circular hole in a plate is the infinitely long notch in a plate. This will help to understand one aspect of the behaviour of the reflection from a part-depth circular hole and so is summarised here. The notch work was achieved prior to the PhD and thus prior to the work done on circular holes. The material thickness and frequency were different in that earlier work, nevertheless, the important trends can be seen in the results. This work on notched plates has been published in the Journal of the Acoustical Society of America [51].

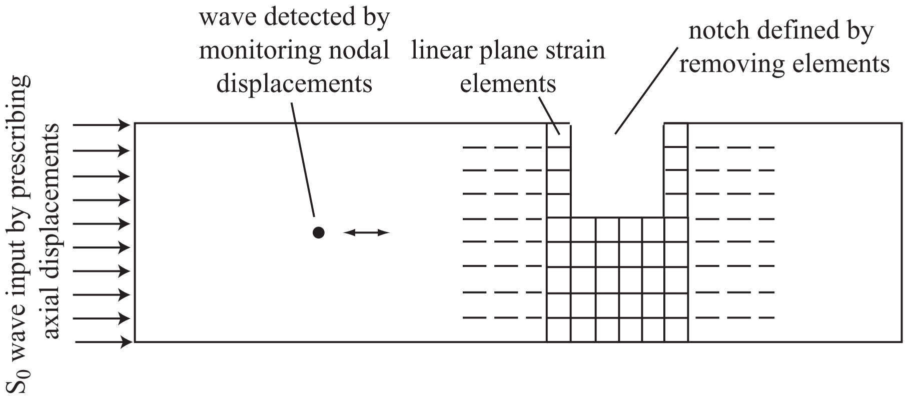

Figure 4.3: Schematic illustration of Finite Element spatial discretisation, with excitation of the S_0 wave.

Finite Element

The notch is assumed to be rectangular in section (with zero width in the case of a crack), is infinitely long and is aligned normal to the direction of propagation. Thus a plane strain assumption in the plane of the particle motion of the Lamb wave is sufficient for all considerations. Thus, the Finite Element modelling was performed in a two-dimensional domain using the program FINEL [72]. A schematic illustration of the model is shown in Figure 4.3. A plate of 3 mm thickness and 600 mm length was modelled, each notch was created simply by removing elements from the mesh, as is shown in the figure. Two different depths of notch were studied, 17 % and 50 % of the plate thickness.

The temporal model used a narrow band signal consisting of a 5 cycle tone burst of 400 kHz in a Hanning window, applied at one end of the plate as a displacement boundary condition in the in-plane direction (as shown in Figure 4.3), thus generating the S_0 wave.

Experiments

A plane wide-band piezoelectric transducer (Panametrics V301, 0.5 MHz centre frequency) was placed centrally at the end of the 3 mm thick plate (see Figure 4.4). In-plane measurement of the signal at a single point on the surface of the plate ensured that only the S_0 mode was present. The signal which was used for the study was a 400 kHz centre frequency tone burst modified by a Hanning window and generated by a wavemaker (Macro design Ltd, UK) instrument.

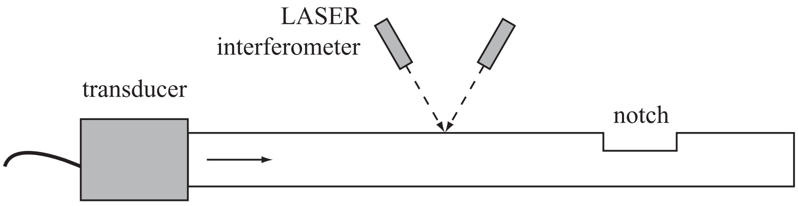

(a) side view

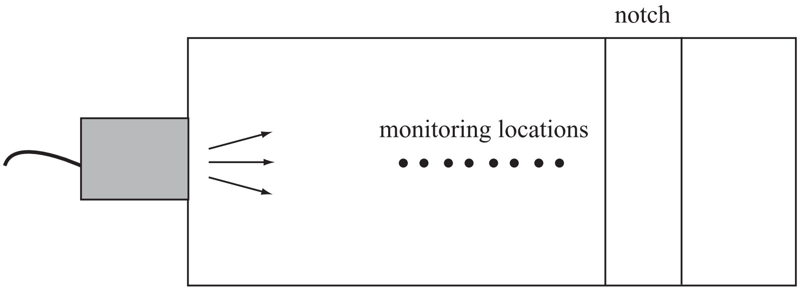

(b) top view

Figure 4.4: Arrangement of notched plate, piezoelectric transmitter and laser receiver for experiments; (a) side view, (b) plan view.

The detection was achieved using the same laser interferometer presented in chapter 2 to measure the in-plane displacement at the surface of the plate. Since the notch reflects energy of both the S_0 and A_0 modes, it was necessary to take steps to detect just the desired S_0 mode. First, the in-plane displacement was measured, rather than the out-of-plane displacement. Second, the measurements were taken at a series of equally spaced positions along the plate, then a two-dimensional Fourier transform (2DFFT) [92] was used to separate the S_0 and A_0 components.

The experiment was repeated for a series of notches identical to the Finite Element cases.

Results

Figures 4.5(a) and 4.5(b) show comparison between experimental data and Finite Element results. The horizontal axis has been scaled to normalise the notch width to the wavelength of S_0. Plotting results in this manner allows the reader to compare different models on the same graph. The experimental measurements and Finite Element predictions can be seen to agree well in both cases.

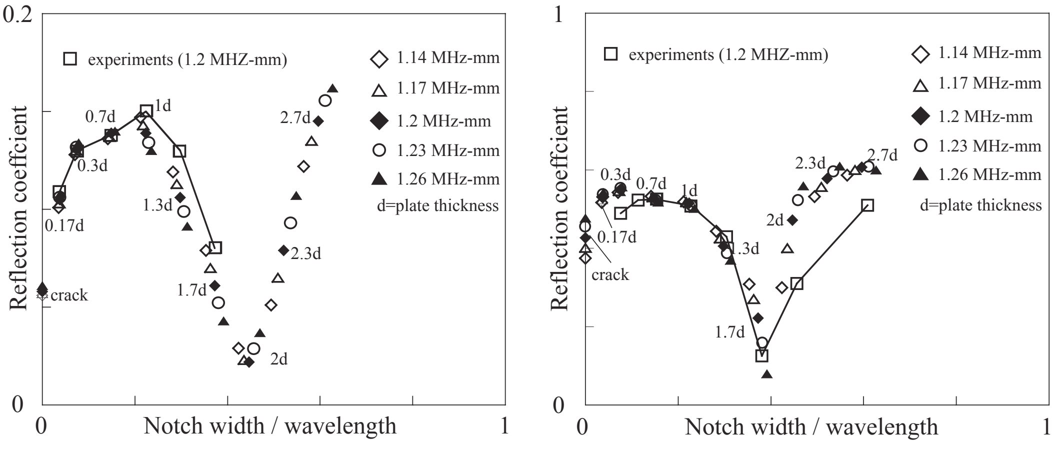

(a) (b)

Figure 4.5: Comparison between predicted and experimental variations of S_0 with notch width normalised to wavelength, when notch depth is (a) 17 % of plate thickness and (b) 50 % of the plate thickness; results for 5 similar frequency-thickness products.

The reflection coefficient starts at a low value, then rises as the notch width increases. The peak amplitude then occurs when the notch width is about 25 % of the wavelength and decreases until it is 50 % of the wavelength, then there is an increase again. It is not shown here, but this pattern of peaks and troughs continues regularly as the notch width is increased. The reason for the peaks and troughs of the function is the interference between two signals which reflect from the notch, one from the leading edge and the other one from the trailing edge. This is the important behaviour which must be understood as a background to the study of the part-depth circular defects.

The reflection from the trailing edge is of course retarded with respect to the signal from the leading edge, so their superposition in the resulting wave packet is either constructive or destructive, depending on the duration of the delay. Furthermore, the reflections from the start and the end of the notch differ in phase too, this is due to the impedance change. For the leading edge, there is a decrease in impedance, whereas there is an increase for the trailing edge. Consequently, the constructive interference occurs when the trailing edge reflection is half a cycle behind the front edge reflection, that is when the notch is a quarter of a wavelength wide. Similarly, a notch width of half a wavelength delays the reflection by one cycle, thereby causing the destructive effect. However, these maxima and minima do not occur exactly at a quarter or half wavelength. This is because the reflection is not only composed of the S_0 mode, but is a combination of both the A_0 and the S_0 modes. This is more evident with the deeper of the two notches.

Further work on the nature of these maxima / minima can be found in [93], where Demma examines the scattering of the SH_0 mode from steps and notches.

4.2.3 Plates with a part-depth circular hole

Geometry of the part-depth circular hole studied

In order to be able to model all the different Lamb modes which might be present, three-dimensional solid "brick" elements with eight nodes were used, each node having three degrees of freedom (X, Y, Z displacements in Figure 4.6). Three-dimensional Finite Element models are computationally very intensive, so just two or three elements were used through the thickness of the plate.

To be sure that two or three elements through the thickness are enough to model the different waves properly, a model with six elements through the thickness was used and compared with the current models. Exactly the same results were achieved and the time required to perform the calculation lasted four times longer than the model with three elements through the thickness. This comforted the author in the choice of having few elements through the thickness in order to gain computational time.

Plates of 5 mm and 7.5 mm thickness were selected, each with a 2.5 mm deep hole. Thus the holes were 50 % and 33 % deep respectively. The two other dimensions (X and Y axes) of the element were 3 mm. Also to reduce computation time, only half of the plate was modelled, applying symmetry in the X/Z plane through the centre of the hole.

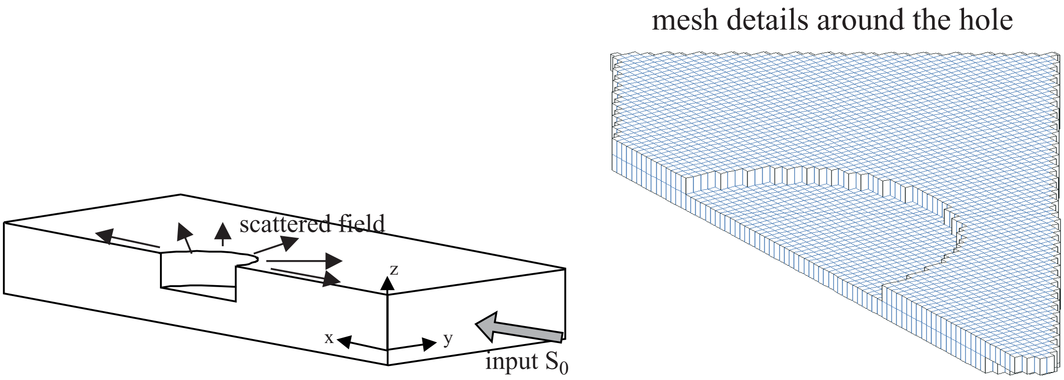

(a) (b)

Figure 4.6: Schematic illustration of Finite Element spatial discretisation: (a) outline of the mesh and (b) details of the hole.

Computational method used

A 5 cycle S_0 wave input was excited at 100 kHz by prescribing axial displacements (in the X direction only) along the whole edge at one end of the plate and its propagation was simulated in the time domain. Following the interaction of the input S_0 with the hole, the S_0, A_0 and SH_0 components of the signal are reflected or scattered. In this chapter, only the S_0 wave specular reflection is studied. Since only S_0 and A_0 are present along the plane of symmetry, a monitoring region was required which was long enough to avoid overlay of the input and these two reflected waves. A plate edge to hole distance of 900 mm was found to be sufficient and 33 points were monitored along the plane of symmetry. To remove the A_0 component, the top and bottom surface in-plane time history signals were added. As A_0 is antisymmetric, this addition removed the A_0 in-plane displacement and only S_0 remained.

4.3 Analytical model

The analytical model for this problem, developed by Dr. T. Grahn, is very similar to that presented in chapter 3. Dr. Grahn has already produced literature on the interaction between the S_0 Lamb mode and part-depth circular defects [82, 94]. In comparison with the model surveyed in chapter 3, the calculation of Lamb and SH waves need now to include the antisymmetric Lamb modes, as the A_0 Lamb mode will be generated by mode conversion at the defect.

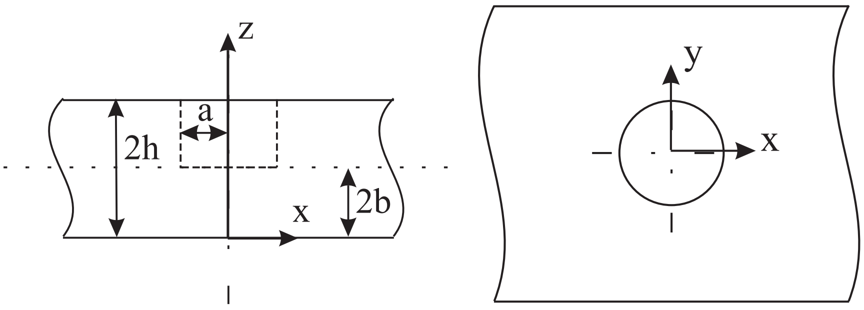

(a) side view **(b)** top view

Figure 4.7: Geometry of the analytical problem with: (a) side view and (b) top view.

The boundary conditions have also changed. For this specific problem, the boundary conditions have to be specified in order to determine the scattered wave field due to the hole in the plate. The boundary conditions are of two kinds, continuity of displacements and stresses. For the displacements, continuity must hold at $r = a$ (see Figure 4.7) in the region of the hole, thus

$$\boldsymbol{u}^{inc} + \boldsymbol{u}^{>} = \boldsymbol{u}^{<}, \quad 0 < z < 2b, \quad r = a. \tag{4.1}$$

where $\boldsymbol{u}^{>}$ is the scattered field in the outer region ($x < -a$ and $x > a$) and $\boldsymbol{u}^{<}$ is the displacement field in the inner region ($-a < x < a$). The boundary conditions for the stress are continuity at $r = a$ in the region below the hole and that the hole is stress free, thus

$$(\boldsymbol{\sigma}^{inc} + \boldsymbol{\sigma}^{>}).\hat{\boldsymbol{e}}_{\boldsymbol{r}} = \begin{cases} \mathbf{0}, & 2b < z < 2h, \quad r = a \\ \boldsymbol{\sigma}^{<}.\hat{\boldsymbol{e}}_{\boldsymbol{r}}, & 0 < z < 2b, \quad r = a \end{cases}. \tag{4.2}$$

where $\hat{\boldsymbol{e}}_{\boldsymbol{r}}$ is the unit vector in the radial direction.

Only polar plots similar to Figures 3.17(a) and 3.17(b) will be compared with the work of the author, unlike in chapter 3 where time traces and reflection ratio curves were also compared.

4.4 Results

Figure 4.8 shows a typical Finite Element time history signal monitored at 390 mm from the edge of a hole 114 mm in diameter and 50 % of the plate-thickness in depth. The incoming S$_0$ Lamb wave on its way to the defect is separated from the S$_0$ wave reflected by the defect.

The reflection ratio was calculated by dividing the spectrum of the full signal reflected from the hole by that of the input, in the frequency domain. The curve thus obtained displays amplitude (reflection ratio) against frequency. By further plotting reflection ratio against the axis “hole-diameter to wavelength ratio”, different models can be compared. The results for 33 % and 50 % deep holes are presented in Figures 4.9(a) and 4.9(b) respectively. The wavelengths of the S_0 mode chosen correspond to frequencies at 90, 95, 100, 105 and 110 kHz for each point extracted from each plate.

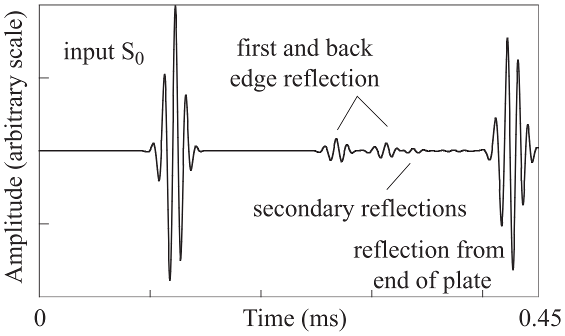

Figure 4.8: Typical time record from Finite Element simulation; hole diameter 114 mm, 50 % of the plate thickness deep and monitored at 390 mm from the first edge of the hole.

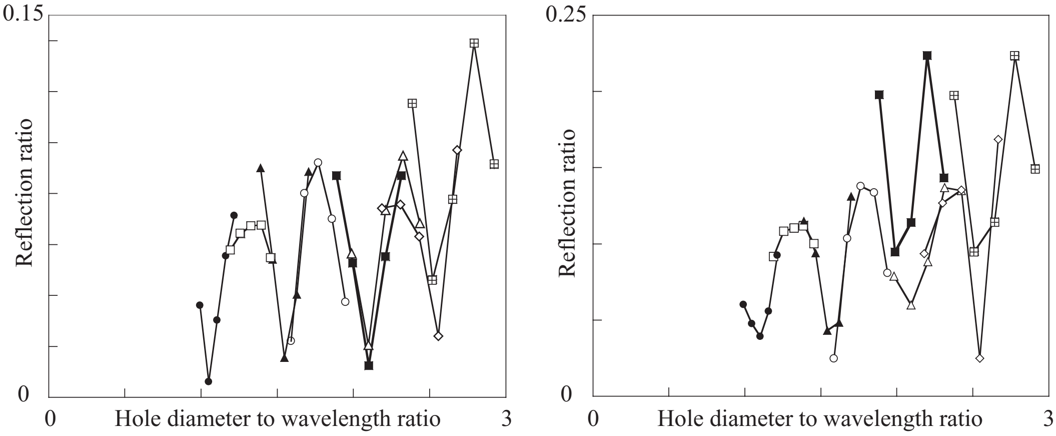

(a) **(b)**

Figure 4.9: Predicted variation of S_0 reflection ratio with hole diameter normalized to wavelength, when hole depth is (a) 33 % and (b) 50 % of plate thickness; results for hole diameters 60 mm (●), 72 mm(□), 84 mm(▲), 96 mm(○), 114 mm(■), 120 mm(△), 132 mm(◇), and 144 mm(⊞) for different frequencies.

As in the case of the notched plates, maxima in amplitude are observed at diameters corresponding to an odd multiple of quarter of wavelengths, and minima at even multiples. These results are very useful from an engineering point of view, but for precise computing, in order to get an accurate mapping of the plate, more understanding is needed, as it is obvious that there is significant scatter in the data, i.e. different results are obtained from the same diameter to wavelength ratio with the different models. One reason for these discontinuities is the mesh details of the holes which changes from one mesh to another. As the hole is modelled with cube-shaped elements, its shape is not exactly a circle and the “definition” of a hole differs one from another. Another reason is that the receiver location is a fixed distance (390 mm), not a normalised distance (fixed number of hole diameters).

In order to see how the reflection function varies with the distance of the receiver from the hole, a series of points was monitored along the axis of symmetry at the mid-plane of the plate (see Figure 4.10). In each case, the processing was performed using the time domain method which has the benefit of smoothing the undulations out of the signal, and so clarifying the comparisons for different distances. The principle of the smoothing will be discussed later.

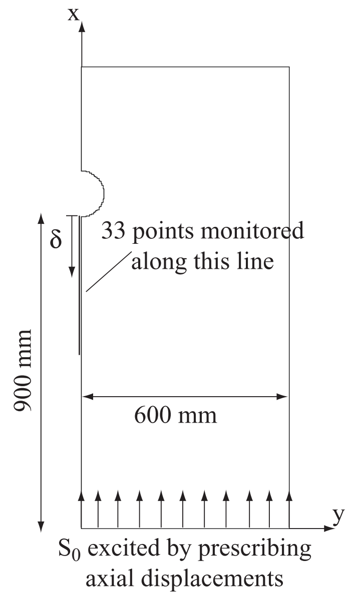

Figure 4.10: Portion of mesh where a circular hole is present and 33 points are monitored along the X axis in order to calculate the decay of the first part of the reflection.

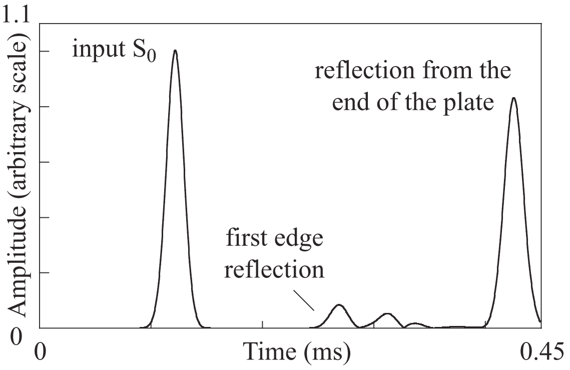

Figure 4.11: Envelope of time signal shown in Figure 4.8; hole diameter 114 mm, 50 % of the plate thickness and monitored at 390 mm from the first edge of the hole.

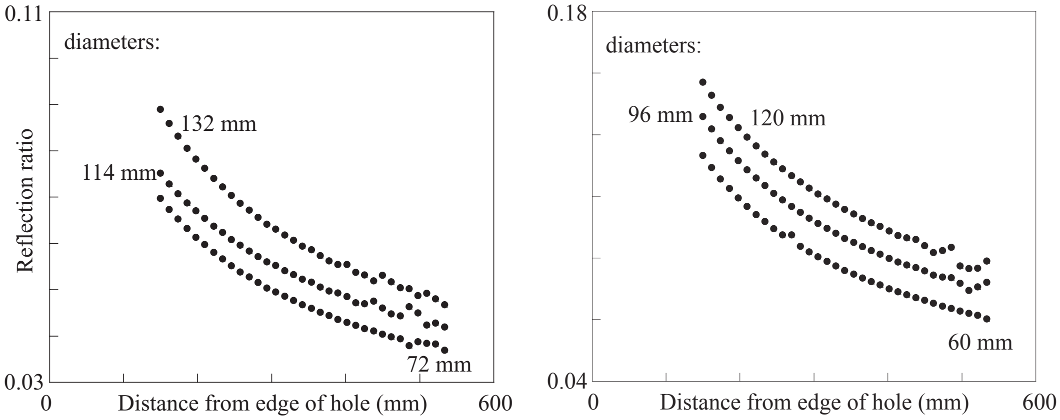

(a) (b)

Figure 4.12: Decay of the first reflection form the hole for (a) 33 % of the thickness deep hole and (b) 50 % of the thickness deep hole. Note that to clarify the results are only shown for 3 diameters.

The time domain processing method uses the Hilbert transform, as follows Figure 4.11 represents the Hilbert transform of the signal in Figure 4.8. This is essentially a convenient way of obtaining the envelope of the time domain signal. The reflection ratio was extracted from the figure by dividing the peak amplitude of the first-edge reflection by the maximum amplitude of the input. This differs from the spectral method used for Figures 4.9(a) and 4.9(b) because that takes the full hole reflection into account, not just the first peak. This was repeated for a range of distances from the defect and for several defect diameters. Results obtained from the different models are presented in Figures 4.12(a) and 4.12(b). As expected, the reflection ratio increases with diameter and decreases with distance from the hole, also the difference in amplitude between the 33 % and 50 % deep hole results can be observed.

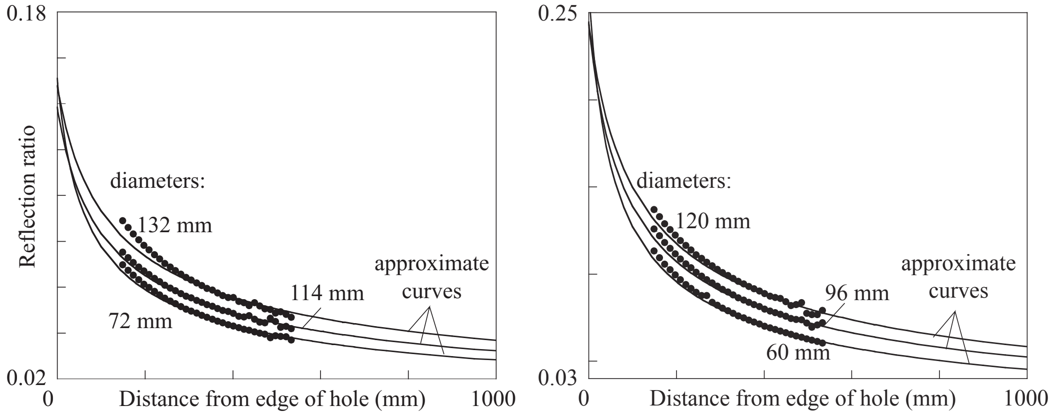

(a) **(b)**

Figure 4.13: Comparison between Finite Element results and approximate curves for 33 and 50 % of the thickness deep hole. Note that the results are only shown for 3 diameters in order to clarify the graph.

The hole is assumed to function as a cylindrical emitter of reflected waves. Since the decay of a signal is (ideally) inversely proportional to the square root of the propagated distance, equation 4.3 should represent the decay of the reflected wave:

$$A(\delta) = \frac{A_{refl}}{\sqrt{\delta + \delta_0}} \tag{4.3}$$

where A_{refl} is related to the amplitude of the wave, δ is the distance from the edge of the hole along the axis of propagation and δ_0 is the distance from the edge to the centre of the beam spreading. As the centre of the hole is also the centre of the curvature where the beam spreading is generated, δ_0 was set equal to the radius of the hole. The coefficient A_{refl} was then calculated simply by taking the Finite Element predictions of the amplitude of the wave at a given distance away from the near-edge of the hole. Comparisons between FE and the approximate curves are shown in Figures 4.13(a) and 4.13(b). The good fit confirms the assumed value of δ_0.

As in the work in chapter 3, an interesting correlation is observed if these approximations are plotted as a function of the ratio between distance and hole-diameter. Figures 4.14(a) and 4.14(b) shows that all the curves plotted in this way are very similar. This means that, at a given distance from the hole measured in multiple diameters, all reflection ratios at a given frequency are approximately the same, whatever the hole size. For example, if the hole diameter is 30 mm, the reflection at 180 mm (6 diameters) away from that hole will be approximately the same as that from a 60 mm diameter hole monitored at 360 mm.

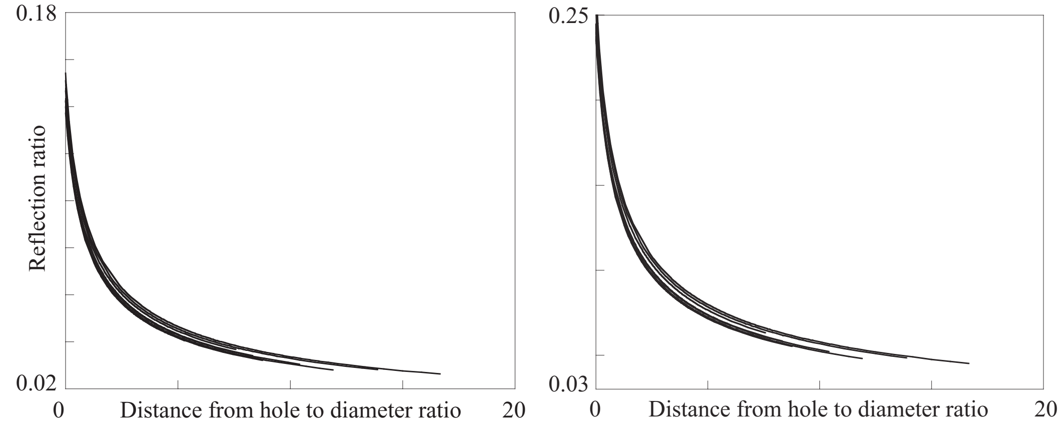

(a) **(b)**

Figure 4.14: Approximations calculated from the Finite Element results, plotted as ratio of distance away from hole to hole diameter for: (a) 33 % of the plate thickness deep hole and (b) 50 %. All data points for 8 diameters between 60 and 144mm are shown.

Returning to the issue of discontinuities in the plots, the waviness phenomenon can be seen as an interference between the S_0 Lamb waves reflected by the defect and secondary reflections. In Figure 4.8, waves other than the reflected and input S_0 mode can be seen to be present (labelled “secondary reflections”). These waves consist of the back edge reflection, circumferential creeping waves (as discussed in chapter 3) and SH_0 waves. Shear waves are present directly on the axis, but only with a radial component that decays quickly (equation 4.3).

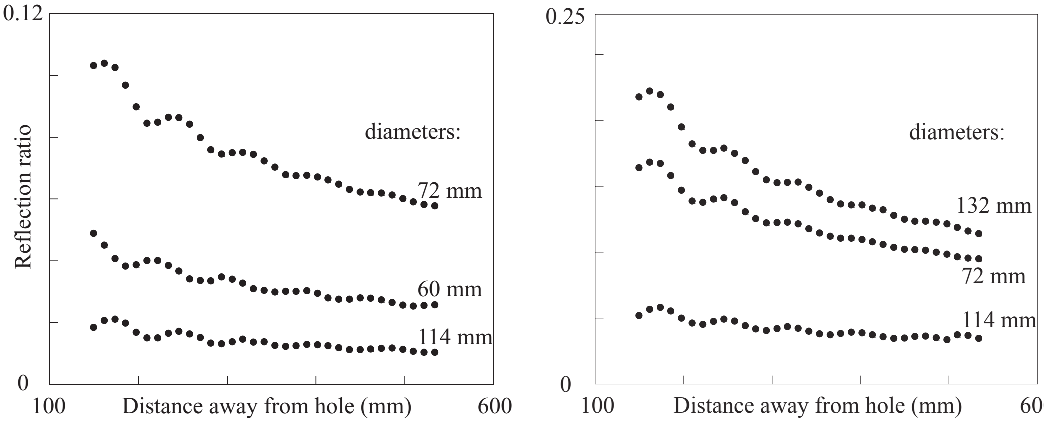

(a) (b)

Figure 4.15: Influence of the creeping waves on the whole wave reflected as it propagates away from the hole for (a) a 33 % of the plate thickness deep hole and (b) 50 % of the plate thickness deep hole.

The total re-radiated field can then be observed as a small perturbation caused by the curvature of the surface. Figures 4.15(a) and 4.15(b) shows the magnitude of the Fourier transform at the centre frequency (100 kHz) of the full signal reflected from the hole shown in Figure 4.8 as a function of distance away from the hole. Figures 4.9(a) and 4.9(b) show the same kind of data but plotted at different frequencies and fixed distance. Figures 4.15(a) and 4.15(b) shows that the decay curve with distance is not smooth, in contrast to Figures 4.12(a) and 4.12(b) which excluded the secondary reflections. This undulation may contribute to the discontinuities between curves for different models shown in Figures 4.9(a) and 4.9(b) (the same hole-diameter to wavelength ratio in Figures 4.9(a) and 4.9(b) was obtained by varying the frequency for different modelled hole sizes).

The scattered field around the hole is illustrated well by a polar plot. Figures 4.16(a) and 4.16(b) show the predicted amplitudes of the scattered modes for a hole which is 100 mm in diameter, when the receiver is at a distance of 250 mm away from the edge of the hole. The circumferential axis of the plots corresponds directly to the angular location with respect to the centre of the hole; the origin (180 degrees) corresponds to the direction of the incident wave. The radial axis of the plots corresponds to the magnitude of the displacement.

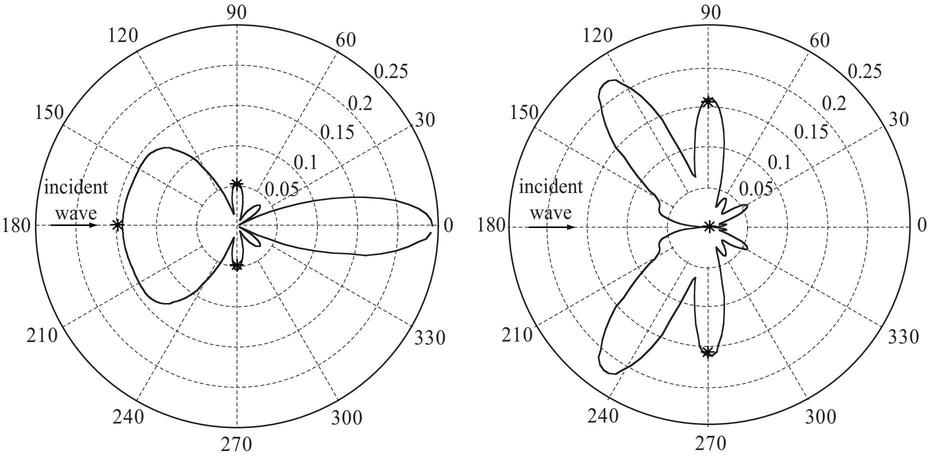

(a) **(b)**

Figure 4.16: Polar plots comparing analytical (solid line) and Finite Element ($*$) predictions for a hole 100 mm in diameter, when the wave is received at 250 mm away from the hole. The radial distance in the plots represents the amplitude of the received signal. The S_0 mode is incident at 100 kHz-mm. Plots show scattering of (a) S_0 mode; (b) SH_0 mode.

The dominant displacement components are shown, that is the radial component, u_r (Figure 4.16(a)), for the S_0 mode and the circumferential component, u_θ (Figure 4.16(b)), for the SH_0 mode. The solid lines are calculated from the analytical model developed by Grahn for a single frequency of 100 kHz. The amplitude plotted here is the whole Lamb mode reflected amplitude from the hole, that is to say the combination of the first edge and the back edge waves. Results from the Finite Element models are also included at some specific angles and those points are calculated by measuring in the frequency domain the reflected or scattered Lamb wave amplitude at 100 kHz.

Very good agreement is found between the two techniques. The reflected S_0 wave is scattered mainly forwards and backwards (at 0 and 180 degrees), while the reflected SH_0 is scattered mainly in the transverse direction. Note that the incoming S_0 wave is not plotted. What can also be drawn from the results, but is not shown here, is that there were enough elements through the thickness of the Finite Element models in order to predict the A_0 mode conversion.

4.5 Conclusion

Following work presented in chapter 3 on related two-dimensional problems, three-dimensional Finite Element studies have been performed in order to investigate the nature of the specular reflection of the simple extensional mode S_0 from a circular part-depth hole in a plate. It was found that:

(a) when the reflection ratio of the full reflection from the defect is plotted as a function of hole diameter to wavelength ratio, maxima in amplitude are observed at diameters corresponding to an odd multiple of quarter-wavelengths, and minima at even multiples. This comes from the constructive or destructive interference between the front and the back edge of the defect reflections;

(b) the signal decays as a function of one over the square root of distance from the centre of the hole;

(c) at a given distance away from the hole-centre, measured in multiple diameters, all reflection ratios at a given frequency are approximately the same whatever size the hole is;

(d) secondary waves, consisting of creeping waves and SH_0 waves, induce undulation in the reflection ratio.

Furthermore, comparison with analytical results of the wave field around the hole showed that the three-dimensional Finite Element model predicts well the S_0 Lamb mode reflected at the defect and the SH_0 mode conversion.

Experiments were not attempted in this chapter because of the difficulty of exciting plane waves, but experiments will be performed in the next chapter, when comparing Finite Element results with the plate tester device (small circular source or plate tester array).

Chapter 5

Reflection of the S_0 Lamb mode from a circular defect when the incident wave is created by a small source

5.1 Introduction

In chapter 3, the interaction of Lamb waves with a through-thickness circular hole was studied. FE predictions compared with experimental results showed that the reflection and scattering of the incident S_0 wave at different monitoring angles around the defect generate a wave field consisting of the SH_0 mode as well as S_0. Their magnitude depends on the monitoring angle. Chapter 4 studied the interaction of the same S_0 mode with a flat bottom circular defect. This showed effects of interactions between the reflections from the near side and the far side of the hole, as well as secondary reflections which propagate around the hole. In these two chapters, the S_0 Lamb mode was excited along one end of the plate, matching the behaviour of a plane wave. In the present chapter, the author is interested in the behaviour of the specular S_0 mode reflection when the incident wave is excited by a circular source aimed to be more representative of the practical transduction arrangement. This will be studied both numerically and experimentally.

The chapter is in 4 sections. The first section surveys the methodology of the Finite Element modelling; the details of the mesh and the frequency range chosen. The second section presents the experimental set-ups; the first studies the case of a single EMAT and a second studies the phased array transducer. Finally the third section will compare results from the two precedent sections before a conclusion is drawn.

5.2 Methodology for Finite Element simulation studies

5.2.1 Frequency range of interest

Figure 5.1 shows the group velocity dispersion curves for Lamb waves and SH waves in an aluminium plate and Figure 5.2 shows stress and displacement mode shapes through the plate at a frequency-thickness product of 750 kHz-mm. This frequency-thickness was chosen because it was found that this is the most appropriate for the use of the EMATs which were available. As in the two previous chapters, the displacements and stresses are dominated by the in-plane component, which means that a wave excited at this frequency-thickness is equally sensitive to any type of defect though the thickness of the plate; it has low dispersion; and if the plate is immersed, the attenuation due to leakage is very small. Within the same frequency range A_0 and SH_0 can also be present as was the case in the preceding chapter.

5.2.2 Discretisation

The simulation of the propagation of Lamb waves has been performed using FINEL [72]. In order to be able to model all the different wave modes that might be present, three-dimensional solid brick elements with eight nodes, each node having three degrees of freedom (X, Y and Z displacements in Figure 5.3(a)), were used. For this project, plates of interest are between 5 and 20 mm thick and it was decided to study a plate of 5 mm thickness. 3D FE models are computationally very intensive so it is important to minimise the number of elements. The author has found ([95]) that

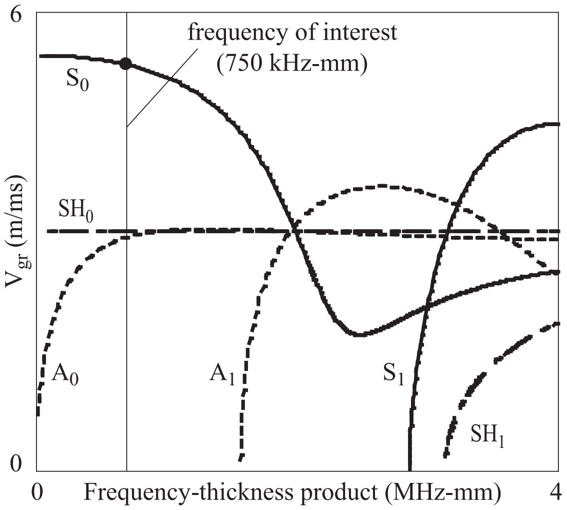

Figure 5.1: Group velocity dispersion curves for Lamb waves in an aluminium plate.

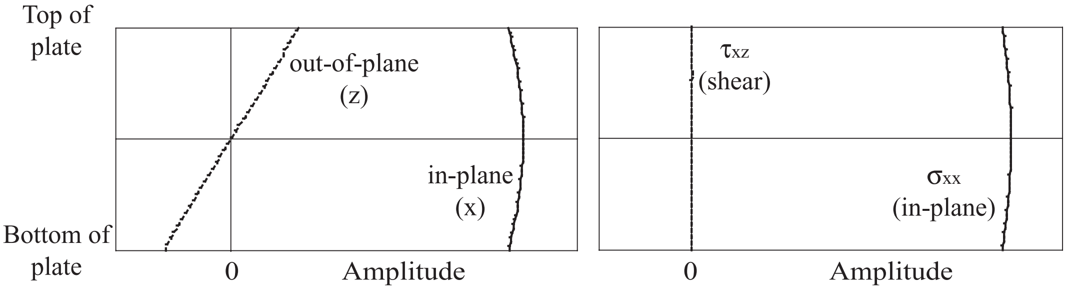

(a) Displacements

(b) Stresses

Figure 5.2: Mode shapes of the S_0 mode in an aluminium plate at 150kHz; (a)Displacements and (b) Stresses.

just two elements through the thickness are sufficient to model all 3 different Lamb modes with reasonable accuracy at this low frequency. The two other dimensions of the element (X and Y axes) were of 1.5 mm. Note that the mesh is then finer than in the two precedent chapters, where elements were 3 mm in the X and Y directions. A hole of 50% of the plate thickness whose diameter varied between one and 2.5 wavelengths of S_0 at 150 kHz (corresponding to 750 kHz-mm) was introduced in the mesh by removing elements. Also, to reduce computation time, only half of the plate was modelled, applying symmetry boundary conditions at the symmetric edge.

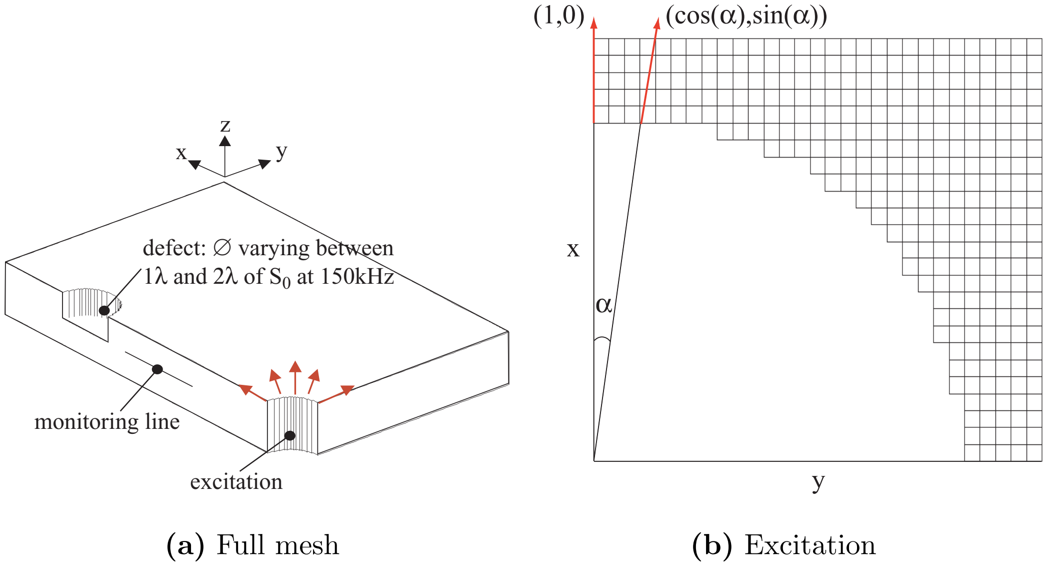

(a) Full mesh **(b)** Excitation

Figure 5.3: (a) Outline of the Finite Element model, showing the monitoring line as well and the excitation; (b) details of the excitation.

It is not possible to excite motion at a single point in all the in-plane directions. Thus in order to model a localised source, excitation from the edge of a circular hole was introduced, as shown in Figure 5.3(b). Excitation could have been applied to a circle of nodes, without creating a hole, but in this case there would have been an additional component of the signal caused by waves propagating back through the centre of the circle. Therefore the use of a hole enables a cleaner signal to be simulated. A five cycle S_0 wave input was excited at 150 kHz centre frequency by prescribing in-plane displacement radially to the edge of the source circle all through the thickness of the plate and its propagation was simulated in the time domain [67, 95]. In order to be sure that the wave was excited in a cylindrical manner (amplitude constant around a circle centred on the source), the incident wave has been monitored at 420 mm from the source and at three angles (0, 45 and 90 degrees) around the excitation source. It can be seen from Figure 5.4 that all three curves overlay perfectly, meaning that the same wave is excited all around the excitation circle.

Following the interaction of the incident S_0 wave with the defect, S_0, A_0 and SH_0

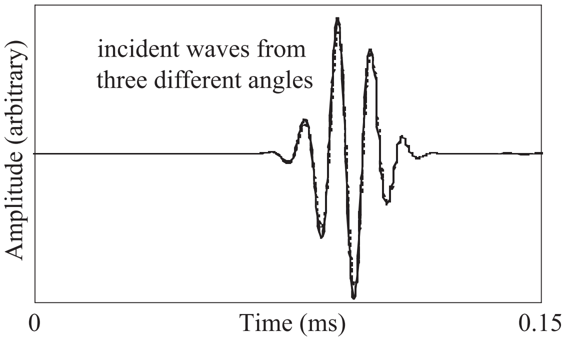

Figure 5.4: Superposed time records from Finite Element simulation at 420 mm from the source and monitored at three different angles: 0, 45 and 90 degrees, showing the incident S$_0$ wave.

are reflected and scattered. For comparison with the experimental data, the author is particularly interested in the S$_0$ specular reflection. Since remotely from the hole only A$_0$ and S$_0$ have motion in the X direction along the plane XZ, by monitoring the in-plane displacement at the centre of the plate thickness, only the S$_0$ mode is monitored. As the A$_0$ Lamb mode is anti-symmetric, its in-plane displacement at this location is equal to zero. The displacement was monitored starting at 150 mm away from the edge of the defect and then every 12 mm for 30 locations.

5.3 Methodology for experimental studies

This section will bring some understanding on the performance of the phased array transducer that was developed by Wilcox, by comparing results with Finite Element predictions. Before the array itself is presented, it is interesting to review the functioning of a single EMAT.

5.3.1 Single EMAT study

The abbreviation EMAT stands for Electro-Magnetic Acoustic Transducer. In the context of ultrasonic NDE it is used to describe a particular family of transducers [96, 97, 98]. These rely on Eddy-currents to induce and receive ultrasonic waves in an electrically conducting material. Their range of application includes for example tube inspection [22, 99, 100], the railway industry [101, 102, 103] and stress measurements [104, 105].

Principle of operation

A wire carrying an alternating current above a sheet of conducting material will induce a “mirror image” current in the conductor. This current is known as an Eddy current. Now, if a DC magnetic “bias” field is superimposed over the region of the Eddy current, a Lorentz force will be generated within the material. This force will react against the source of the magnetic field. This force will be perpendicular to the eddy current and the magnetic field. By choosing the orientation of the magnetic field it is thus possible to induce the S_0 mode in the plate. The ability to generate an in-plane wave is not the only advantage of the EMAT, it also has more predictable coupling, and can also work at high temperature. On the other hand, they are not as sensitive, in voltage terms, as piezoelectric transducers.

Figure 5.5 shows an example of the EMAT that will be used in the experiments. Circular eddy currents are induced in the plate (parallel to the coil) and they interact with an out-of-plane magnetic field to produce a radial pattern of Lorentz forces on the plate.

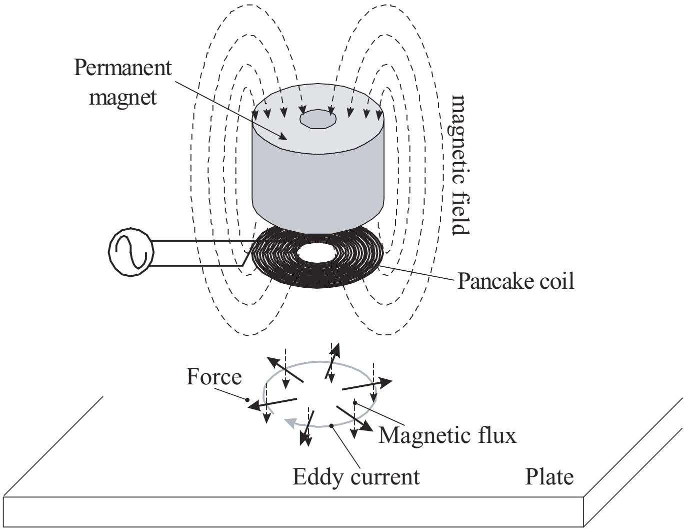

Figure 5.5: Pancake coil EMAT schematic diagram.

Experimental set-up

Two kinds of experiments have been carried out with a single EMAT. First the EMAT transducer is supposed to work as point source and it was considered useful to check its basics behaviour. This was performed with the help of a student: Prabhu Rajagopal. To study this, tests were done on a 4 mm thick, 1 m by 1.28 m aluminium plate. The transmitter and the receiver (both EMATs) were located along the diagonal of the plate. Both of them had weight to hold them down and the gap between the plate and the EMAT is constant and equal to the plastic layer underneath it. In order to obtain the variation of the amplitude with distance, the receiver was moved every 10 mm away from the transmitter for 25 measurements. Figure 5.6(a) describes this set-up.

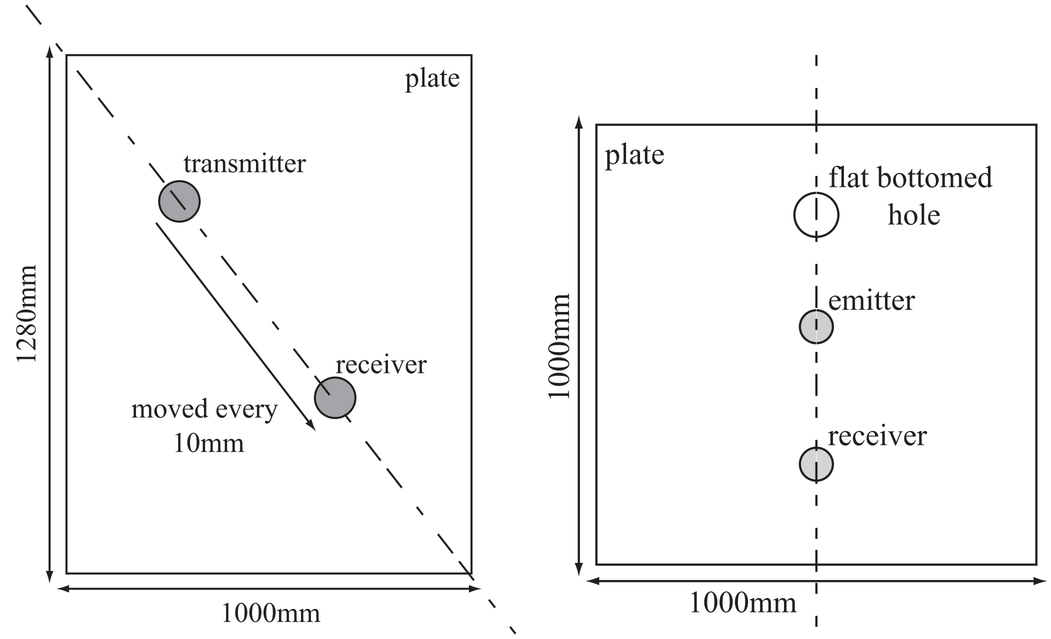

(a) Point source behaviour experiment

(b) Reflection ratio study experiments

Figure 5.6: Pair of single EMAT experimental set-up for (a) the study of the point source behaviour and (b) reflection ratio from flat bottomed circular defects.

The second set of experiments was carried out to compare results directly with the Finite Element reflection ratio calculations.

The major problem working with time traces is to separate unwanted echoes from echoes from the defect. One idea would be to use a two dimensional Fourier transform (2D-FFT), but contrary to section 4.2.2, the incident wave here is supposed to be a point source and so it decays with distance travelled. Hence, the 2D-FFT, which extracts an average value of the amplitude over a spatial length cannot usefully be employed. Instead, the plate has to be designed so that all the unwanted signals are separated from the reflection from the defect. As the thickness increases, the amount of the A_0 mode increases and so the thickness was chosen to be as small as possible in order to reduce this factor. Taking into account these factors, 3 mm thick aluminium plates were used. The plates were 1 m by 1 m wide and a 30, 40 or 50 mm diameter flat bottom circular defect was machined in each of them (see Figure 5.6(b)).

Different measurement distances were used for each defect (hole). For the 50 mm diameter and 50 % of the plate-thickness defect, the emitter was positioned at 125 mm from the leading edge of the hole and the receiver was positioned at a further 300 mm away. For the 40 mm diameter hole the emitter was placed at 130 mm from the leading edge of the defect and the receiver 300 mm further. The emitter for the experiment on the 30 mm diameter defect was placed at 140 mm from the edge of the defect and the receiver at 250 mm from the exciter EMAT. Five frequency-thickness product measurements were taken at 450, 570, 660, 810 and 1020 kHz-mm.

5.3.2 Full array study

A 1 m by 1 m by 5 mm thick aluminum plate was used for the full array experiments. Two defects, 30 and 50 mm in diameter and 50% of the plate thickness deep, were machined in the plate as shown in Figure 5.7. The S_0 mode was excited by a 5 cycle 150 kHz tone burst modified by a Hanning window. The testing device [1] uses an array of transduction elements (the overall diameter of the array is 200 mm) to excite and detect guided waves. The array elements are electromagnetic acoustic transducers (EMATs) and individually they behave as either point transmitters or receivers with omni-directional sensitivity. The transmission and reception electronics and digitisers are housed in a number of separate boxes and the overall operation is controlled by a computer. Digital post-processing of the data obtained from numerous transmitter receiver pairs enables the system as a whole to achieve directionality and wavelength selectivity.

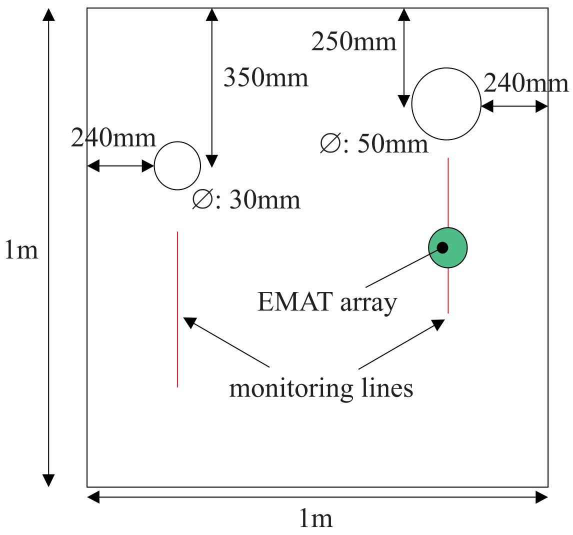

Figure 5.7: Experimental set-up using the phased array transducer.

Conceptually, the operation of the array may be regarded as a number of pulse-echo tests, each looking in a different direction at the surrounding plate. In each of these tests, the array sends out a burst of guided wave energy in a particular direction and detects energy reflected back towards it from the same direction. Reflections occur when the outgoing wave-packet is incident on a feature in the plate such as an edge or a defect. The final output from the array is displayed to the operator as a two-dimensional map of the plate, where a colour scale indicates the amplitude of the reflected signal at each point in the plate. Because the array is of finite size, its directionality is not perfect, and it cannot resolve the angular position of a reflector precisely. Instead, a single reflector produces a characteristic arc shaped signal on the output map as can be seen later. The array was used along two lines of interest as shown in Figure 5.7, it was hold down by weight and the gap between it and the plate was equal to the plastic layer thickness underneath it. More information about this array can be found in [1].

5.4 Results

The results of the Finite Element, analytical and experimental studies are presented and compared in this section. Only the direct reflection of the S_0 wave from the hole is considered. The results from the single EMAT study will give some insight for the studies carried out with the phased array transducer.

5.4.1 Single EMAT

Single EMAT studies are performed in order to understand the behaviour of the elements of the phased array transducer. In this manner experiments are made to be compared with FE results to investigate if it works as a point source. In a second part, more investigations will be performed in order to see if a receiving EMAT acts on any waves which travel under it. That is to say, if the properties of the electronic equipment or the effect of the magnetic field modify the waves travelling underneath.

Comparison between Finite Element and single EMAT results

In order to see how the reflection function varies with the distance of the receiver from the hole, Finite Element predictions of the reflection ratio were made at a series of points along the axis. In each case the processing was performed using the time domain method which had the benefit of smoothing the undulations out of the signal, and so clarifying the comparisons for different distances.

Figure 5.8(a) shows a FE typical measured time history at a location on this monitoring line and 350 mm from the hole. This shows the incident S_0 mode on its way to the hole, which was in this case 50 mm in diameter, and the S_0 reflection from the hole. The secondary reflections can also be seen. Figure 5.8(b) shows a measured time history trace at a location 425 mm from the hole. The centre frequency of the 5 cycle tone burst is 810 kHz. This shows the incident S_0 mode on its way to the hole, which was in this case 50 mm in diameter, and the S$_0$ reflections from the hole. Electrical noise is also present, but it does not interfere with the incident wave.

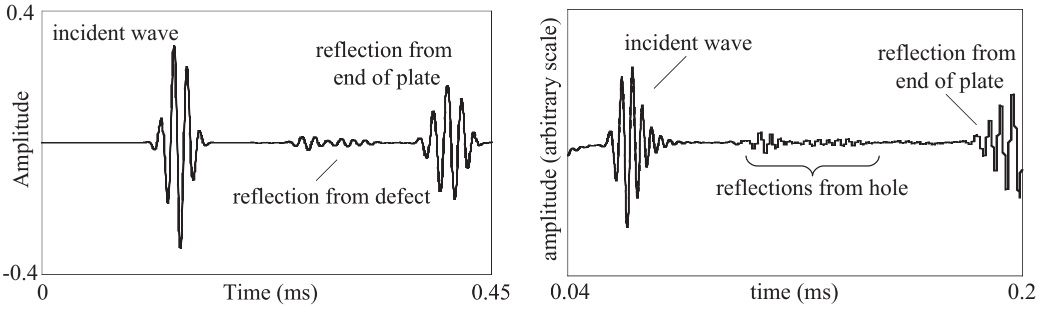

(a) Finite Element **(b)** Single EMAT

Figure 5.8: Example of (a) a monitored FE time signal at 350 mm away from the edge of the hole, the hole is 50 mm in diameter; and (b) a monitored single EMAT time signal at 425 mm away from the edge of the hole; the hole is 50 mm in diameter.

Figures 5.9(a) and 5.9(b) represent the Hilbert transforms of the signals in Figures 5.8(a) and 5.8(b), respectively. The reflection ratio was extracted from the figures by dividing the peak amplitude of the S$_0$ direct reflection by the peak amplitude of the input S$_0$ wave.

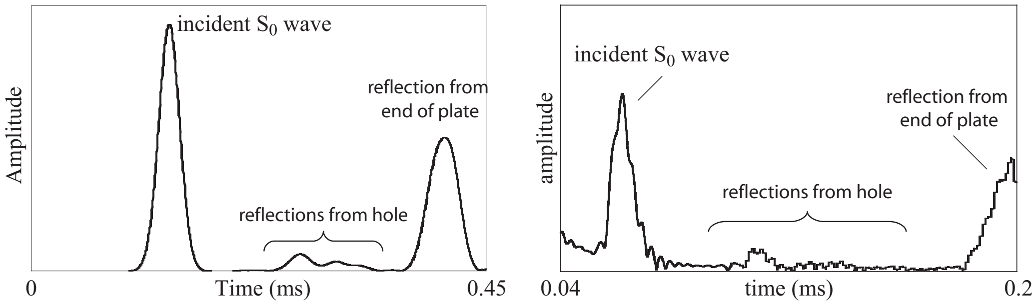

(a) Finite Element **(b)** Single EMAT

Figure 5.9: (a) Envelope of time signal shown in Figure 5.8(a); hole diameter 50 mm, 50 % of the plate thickness and monitored at 350 mm from the first edge of the hole. (b) Envelope of time signal shown in Figure 5.8(b); hole diameter 50 mm, 50 % of the plate thickness and monitored at 425 mm from the first edge of the hole.

Figure 5.10 compares experimental data with FE results for decay of the incident S$_0$ Lamb wave with distance travelled towards the hole. Also shown on the figure is the "point source decay" approximation function described in earlier chapters. Excellent agreement is found between all three. This result will be important to explain the behaviour of the phased array transducer.

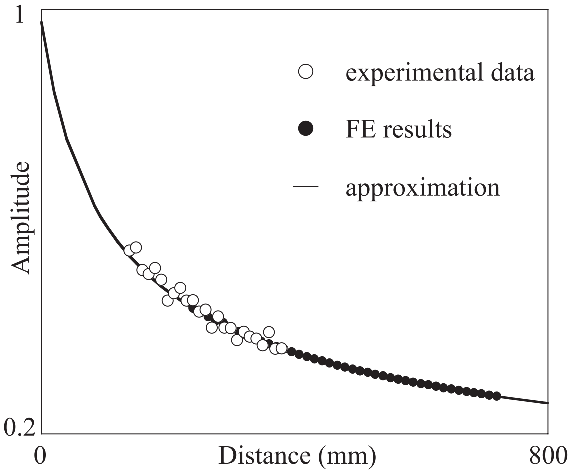

Figure 5.10: Comparison between Finite Element predictions (•) and experimental data using a single EMAT (∘) of the incident S$_0$ mode plotted as a function of distance from the source. Values are taken from the Hilbert envelope calculation. The line shows the approximation function which has been fitted to just one point.

The reflection ratio was calculated by dividing the spectrum of the full signal reflected from the hole by that of the input in the frequency domain, for both the FE and experimental data and some results are shown in Figure 5.11. The curve thus obtained displays amplitude (reflection ratio) against frequency. The points on the graph correspond to 10 frequency-thickness measurements from the Finite Element results and 5 frequency measurements from the experimental data within the frequency-thickness bandwidth 500-1000 kHz-mm. Note that each frequency-thickness product measurement corresponds to a hole diameter to wavelength ratio. Plotting reflection ratio against the axis "hole-diameter to wavelength ratio" allows different models to be compared. The experimental incident wave has travelled only 125 mm on its way to the defect, compared with the 900 mm for the FE calculations;

and the receiver is placed at 425 mm away from the hole in both cases. In order to compensate the difference in amplitude between the two incident waves when they reach the defect, the beam spreading, or decay in amplitude, is taken from Figure 5.10 and normalized to that of the FE. The results for 50 % deep holes are presented in Figure 5.11 and good agreement is found between the different techniques. As in the previous case (*cf.* chapter 4), maxima in amplitude are observed at diameters corresponding to an odd multiple of quarter of wavelengths, and minima at even multiples. There is still scatter in the data despite the finer mesh, i.e. different results are obtained from the same diameter to wavelength ratio with the different models. One reason for these discontinuities is the mesh details of the holes which change from one mesh to another. As the hole is modelled with cubic elements, its shape is not exactly a circle and the “definition” of one hole may differ from another.

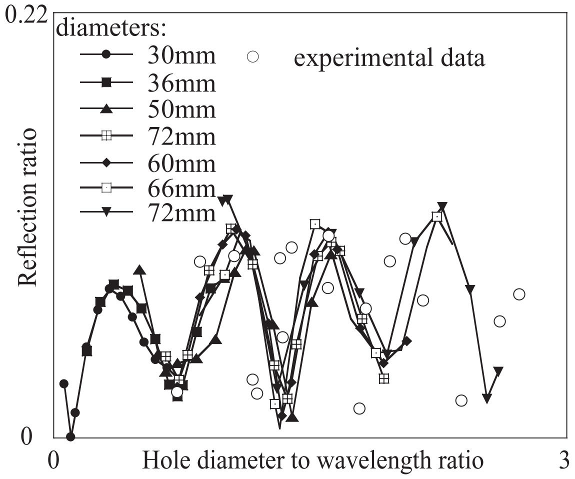

Figure 5.11: Comparison between predicted and experimental variation of S_0 reflection ratio with hole diameter normalized to wavelength, when hole depth is 50 % of plate thickness; FE results for hole diameters 30 mm (•), 36 mm (■), 50 mm (▲), 57 mm(⊞), 60 mm (♦), 66 mm (□), and 72 mm(▼) and experimental data for 30 mm, 40 mm and 50 mm (○) for different frequencies.

Study on single EMAT for plate tester use

Three different studies were performed in order to assess the physical properties of a single EMAT and their effect on the plate tester device. They are summarised below.

The first study showed that there is some variation of measurements with time. Measurements showed that the amplitude of the signal takes a few minutes to stabilize. This variation (around 3 %) was found to be mainly caused by the electrical system of the receiver EMAT.

The second study was carried out after the electrical system had been on for a while and it showed that EMATs give consistent readings but as the thickness of the plate increases, the repeatability decreases. The A_0 Lamb mode has some in-plane displacement at the frequency-thickness product used for the tests. Hence, the EMAT exciting in-plane displacements will generate some A_0. The reason for this change in repeatability with the thickness of the plate is that as the thickness increases, the A_0 Lamb mode is more readily excited. This may become an issue for the sensitivity of the plate tester device, as plate up to 10 mm thick can be tested.

A final study showed that the magnetic field created by a receiving EMAT did not perturb the signal going under it as it has already been seen by others [106]. This study was also important in order to understand the full phased array transducer. As it was explained in section 5.3.2, the plate tester excites with one EMAT after another and receives with all. Then, the excited wave will propagate in the plate and underneath the receiving EMAT, but the magnetic field created by the receiving row should not alter the signal.

In conclusion to this study, it comes out that small variations in the power supply to the receiver are the only source of variations in the results.

5.4.2 Comparison between Finite Element and phased array results

In this section, results of Finite Element studies with a small circular source are compared with results obtained with the plate tester device. The calculations are on the outgoing wave as well as the S$_0$ specular reflection.

Finite Element study

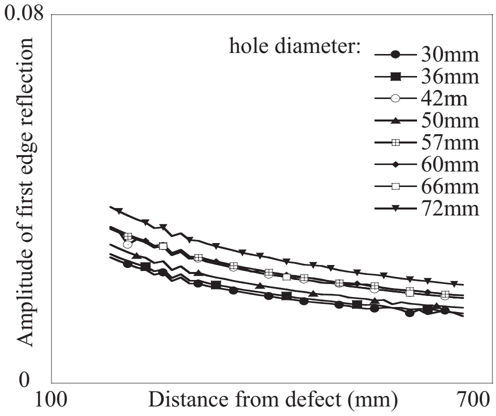

Figure 5.12: FE predicted decay of amplitude of first reflection from the defect with distance from the hole. Different hole diameters are plotted: 30 mm (●), 36 mm (■), 42 mm (⊙) 50 mm (▲), 57 mm (⊞), 60 mm(♦), 66 mm (□), and 72 mm(▼). Source has unit amplitude.

Figure 5.8(a) shows a typical Finite Element time history signal monitored at 350 mm from the edge of a hole 50 mm in diameter and 50 % of the plate-thickness in depth when the source excitation is from a 120 mm diameter circular source. The side of the source was 960 mm away from the side of the defect. The figure shows clean separation of the signals, so allowing reliable extraction of the incident and reflected parts for the measurement of the amplitude of the reflection. The reflected signal is the sum of signals from the near and far edge of the hole, and they can also include creeping waves [95] and SH$_0$ waves which have been created at the defect and reflected at a slight angle around the XZ plane. In order to see how the reflection function varies with the distance of the receiver from the hole, Finite

Element predictions were made at a series of points along the axis. In each case the processing was performed using the time domain amplitudes. Figure 5.9(a) shows the Hilbert transform of the signal in Figure 5.8(a). The amplitude of the reflected signal from the hole was measured by taking the peak amplitude of the whole reflection from the hole. This was repeated for hole diameters varying between one and 2.5 wavelengths of S_0 at 750 kHz-mm. The amplitude of the incident signal was unity at the edge of the source circle. The results are presented in Figure 5.12. As expected, the reflection amplitude increases with hole diameter and decreases with distance from the hole, the decay being inversely proportional to the square root of the propagated distance.

Figure 5.13 shows the same curves but when the distance from the edge of the hole to the monitoring location is normalised to the defect diameter. Unlike in the plane wave predictions [67, 95], all the curves do not overlay, here we also need to take into account the source diameter and the distance between the source and the defect.

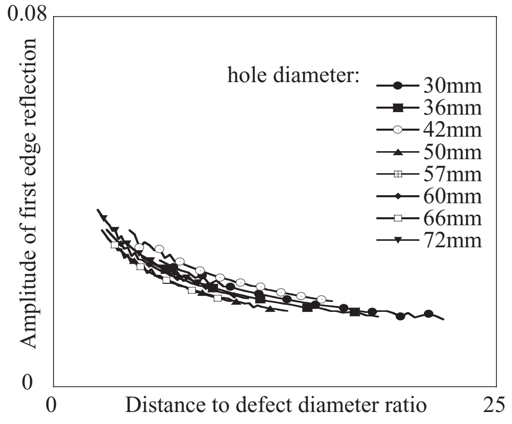

Figure 5.13: FE predicted decay function when the distance from the hole is normalised to the diameter of the defect. Different hole diameters are plotted: 30 mm (●), 36 mm (■), 42 mm (⊙) 50 mm (▲), 57 mm (⊞), 60 mm(♦), 66 mm (□), and 72 mm(▼). Source has unit amplitude.

Two models were studied in order to confirm the proposed normalisation procedure. The first model had a source diameter of 120 mm and the defect was placed at 8 source diameters away (960 mm) from the edge of the source circle. A second model had a 60 mm diameter source and again the distance between the edge of the source and the defect was 8 source diameters (480 mm). The results for two different defect diameters are shown in Figure 5.14. The two reflection amplitude curves overlay. This shows that the source can be normalised for all cases by the ratio of its distance from the defect to its diameter.

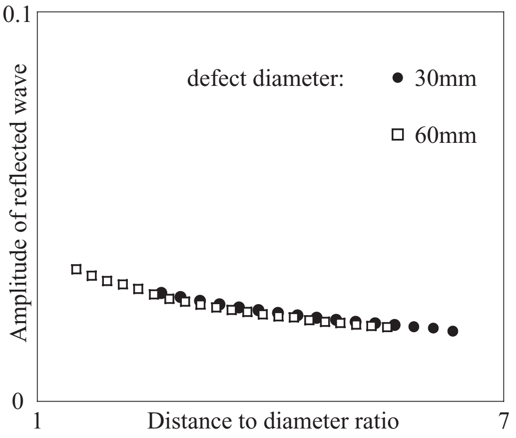

Figure 5.14: FE predicted decay function when the distance from the hole is normalised to the diameter of the defect and the distance between the edge of the source and the defect is taken into account. Results shown for a 30 mm diameter defect (●) and a 60 mm diameter defect (□). Source has unit amplitude.

Comparison with the plate tester device results

Figure 5.15 shows an example of a map obtained by the plate tester system described earlier in the chapter and in detail in [1]. The edges of the plate can be clearly seen as well as the two defects. Only one wave reflected by the 30 mm diameter defect is detected, as the near edge and the far edge reflections overlay in time. On the other hand, these two reflections can be seen separately for the 50 mm diameter hole.

In order to compare FE amplitude results with these experiments, the FE incident wave needs to be scaled to the amplitude of that from the experiments. In the FE model, the incident wave has unit amplitude at the edge of the source circle. In the experiment, the normalisation is such that the incident wave has unit amplitude at its first reflection, this being the near edge of the plate (240 mm, see Figure 5.7).

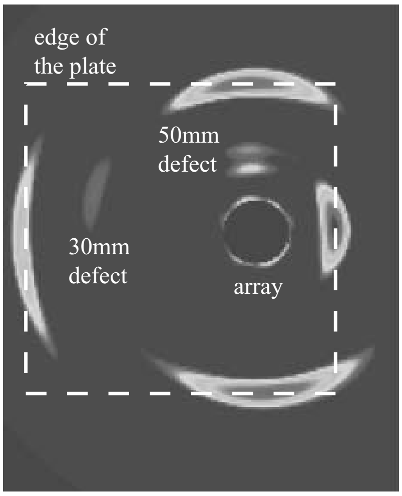

Figure 5.15: Map of the plate obtained with the plate tester device [1]. Scale: 27 dB (white 0 dB, black -27 dB).

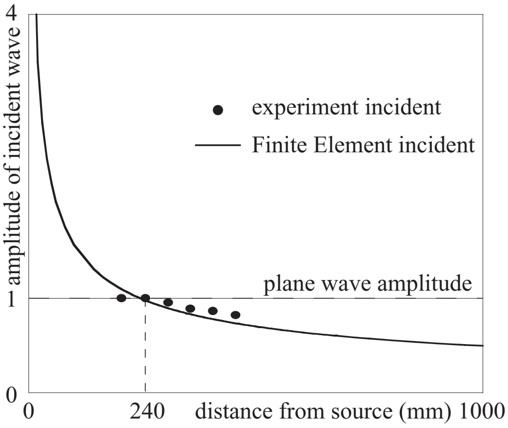

Figure 5.16: Comparison between experimental and FE results of the decay of the amplitude of the incident wave. Incident wave has unit amplitude at 240 mm from the centre of the source.

It is interesting to see the nature of the decay, or beam spreading, of the outgoing wave from the experimental transducer before it gets to the defect. This is needed to understand if the approximation of decay from a point source is correct. Figure 5.16

shows a comparison between the FE and the experimental results for the outgoing wave. The dashed line shows the constant amplitude which would be expected for a plane wave source (unity), the solid line is the amplitude predicted by FE for a point source, and the filled circles are the experimental data. In general, good agreement is found between FE and experiments. It seems, unsurprisingly, that the decay of the incident wave follows the predicted point source decay at distances greater than the reference distance (240 mm).

Figures 5.17(a) and 5.17(b) show a comparison between the experimental data (symbols) and the FE results (dashed line: plane wave; solid line: circular source excitation) for the wave reflected from a 30 mm diameter defect (Figure 5.17(a)) and a 50 mm diameter defect (Figure 5.17(b)). The symbols representing the experimental data are calculated as follows: the middle point is the root mean square (rms) of 5 values; the upper and lower points are the rms plus or minus one standard deviation, respectively. Again, very good agreement is found between the predictions and the experiments. The same trend as for the incident wave, of point source decay, is observable. There is one anomalous experimental point marked α on Figure 5.17(b), it is possible that this point results from an experimental error.

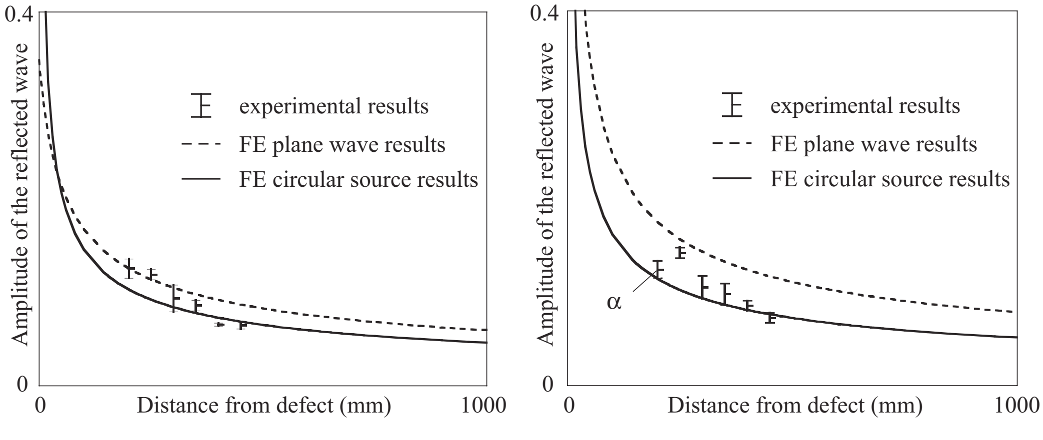

(a) Defect diameter: 30 mm **(b)** Defect diameter: 50 mm

Figure 5.17: Comparison between experimental and FE results of the decay of the amplitude of the reflected wave for (a) a 30 mm diameter defect and (b) a 50 mm diameter defect. Incident wave has unit amplitude at 240 mm from centre of source.

5.5 Conclusion

In the two precedent chapters, the interaction of a plane S_0 Lamb wave with circular shaped defects has been studied.

In this chapter, three-dimensional Finite Element studies have been performed in order to investigate the nature of the reflection of the simple extensional mode S_0, excited by a circular source, from a circular part-depth hole in a plate, and the results have been compared with experimental measurements.

FE model studies have demonstrated that the reflection behaviour for a circular source can be normalised to account for the source diameter, the defect diameter, and the distance between them. Very good agreement was found between FE and experimental results using a single EMAT and the prototype plate tester instrument. The single EMAT experiments were performed in order to give some understanding of the full array and it was found that there is limited experimental scattering in the results which comes from fluctuations of the power supply to the receiver if it is used before it has had enough time to stabilize.

Chapter 6

Conclusions

The non-destructive testing of materials can be conducted by various techniques, of which ultrasonic waves is one of the most common. Lamb waves are of particular interest for the inspection of large structures. There are a number of reasons for this: they permit the inspection of a line or a 2-dimensional space rather than a single point; they are equally sensitive to flaws on either side of the plate; they propagate over long distances; and they are guided by the structure.

The detection of corrosion in large plate-like structures such as oil tanks and pressure vessels using guided wave array transducers has been investigated in this thesis. A new technique using Lamb waves to assess rapidly the integrity of a plate has been developed. A transducer unit is placed on the plate which generates and receives Lamb waves in controlled directions; processing the reflected waves allows a map of corrosion anywhere in the plate to be constructed. Work on the transduction and signal processing aspects of this technique has already been carried out by Dr. Paul Wilcox. This thesis addressed the scattering aspect of the project, assessing the important challenge of identifying the strength of the reflection of the guided waves from the defects.

6.1 Non Propagating Modes

The chosen Lamb mode for the plate tester device is the S_0 mode, but when it reaches a non-symmetric feature, it will mode convert into anti-symmetric modes. This study of the reflection of the fundamental A_0 and S_0 modes from the end of a plate has been carried out in order to understand two phenomena: (1) it is essential when processing the received signal to account for the ones which are reflections from the edge of the plate; for example, if not understood, phase delays of these reflections could affect the performance of the phased array transducer; (2) it is important to be aware of how far the transducer needs to be from the edge of the plate in order to avoid detecting the additional localised displacements.

Semi-analytical, Finite Element and experimental studies confirmed the presence of these non-propagating modes when the incident Lamb mode was A_0. Two frequencies have been studied, one below the A_1 cut-off frequency (1 MHz-mm) and one above (2.7 MHz-mm). Good agreement has been found between all three techniques. Then, by identification of the displacement fields and phases of the propagating modes, it has been possible to remove these propagating modes from the total edge displacements, thus revealing and illustrating the fields due solely to the non-propagating modes.

The symmetric S_0 Lamb mode has also been studied, and Finite Element predictions showed that within the frequency range up to the A_1 cut-off there is no evidence of such additional disturbances. There was also no evidence of a phase change when reflecting from the end of the plate. Nevertheless, this is only applicable to the low frequency regime; significant amplitudes of non-propagating modes exist at higher frequencies.

Overall, the changes of phase and the region around the edge of the plate where these non-propagating modes occur have been identified for both A_0 and S_0 modes.

6.2 Reflection and scattering of the S_0 Lamb mode from circular defects

The interaction between an incident S_0 Lamb wave and a circular defect has been studied through three different chapters. The studies started with the simplest of shapes, that is to say a circular hole through the full thickness of a plate and plane wave excitation, and went on to a more realistic study of part depth defects and circular sources.

6.2.1 Hole through the full thickness of a plate - Plane wave excitation

The interaction between the S_0 Lamb wave and a circular hole through the full thickness of a plate was studied using Finite Element and experimental approaches. The results have also been compared with analytical solutions developed by Dr. Tomas Grahn. The specular S_0 reflection, and the SH_0 wave scattered at 90^o from a hole whose diameter varied between 1 and 3 wavelengths of S_0 at 100 kHz were studied with particular interest. Good agreement was found between all three different techniques.

The results indicated that both S_0 and SH_0 reflections exhibit equivalent behaviours. It was shown that the reflection ratio increases with the hole diameter and decreases in a cylindrical beam spreading manner with the distance from the defect. It was also shown that if this distance from the hole is normalised to the corresponding defect diameter, all the curves overlay. This is understandable as all the parameters of the system are then taken into account. Also the results were perturbed by additional reflections from the hole, consisting of creeping waves as well as shear waves propagating at shallow angles around the monitoring lines.

6.2.2 Part depth hole - Plane wave excitation

As a normal follow up of the work done on through thickness holes, three-dimensional Finite Element studies have been performed in order to study the nature of the direct S_0 reflection from 33 % and 50 % of the plate thickness deep flat-bottom circular defects.

The first results showed that when the reflection ratio is plotted as a function of hole diameter to wavelength ratio, maxima in amplitude are observed at diameters corresponding to an odd multiple of quarter-wavelengths, and minima at even multiples. This behaviour is the result of the interference between the near edge of the hole and the back edge of the hole reflections. The reflection from the trailing edge is of course retarded with respect to the signal from the leading edge, so their superposition in the resulting wave packet is either constructive or destructive, depending on the duration of the delay. Furthermore, the reflections from the start and the end of the hole differ in phase too, this is due to the impedance change. Consequently, the constructive interference occurs when the trailing edge reflection is half a cycle behind the front edge reflection, that is when the defect is a quarter of a wavelength in diameter. Similarly, a diameter of half a wavelength delays the reflection by one cycle, thereby causing the destructive effect. Other results showed the same features as for the full thickness deep defects, that is to say: the signal decays as a function of one over the square root of the distance from the centre of the hole; at a given distance away from the hole-centre, measured in multiples of hole-diameters, all reflection ratio are approximately the same whatever the diameter is; and secondary waves, consisting of creeping waves, as well as SH_0 waves, induce undulations in the reflection ratio results.

Furthermore, the S_0 and SH_0 wave fields around the hole were compared with analytical solutions and the good agreement showed that the Finite Element model predicted well the symmetric modes as well as the anti-symmetric mode converted at the defect. Further more, the latter was not trivial due to the small number of elements through the thickness, which might not have been enough to model correctly the A_0 Lamb mode.

6.2.3 Part-depth hole - Circular source

The third part of the study of the interaction of the S_0 Lamb wave with a circular defect was when the incident S_0 mode was approximated by a small circular source in the low frequency-thickness regime.

A three dimensional Finite Element mesh was generated, representing an area of the plate with a 50% of the plate thickness deep circular hole. The specular reflection of an incident S_0 wave was predicted and compared with the plate tester device as well as with a single EMAT transducer.

FE model studies demonstrated that the reflection behaviour for a circular source can be normalised to account for the source diameter, the defect diameter, and the distance between them. Very good agreement was found between FE and experimental results. In addition to the generic results throughout the thesis, the single EMAT experiments gave some understanding of the full array and it was found that one source of experimental scattering in the results comes from the power supply to the receiver, whereas the magnetic field created by a receiving EMAT has no effect on the wave propagating underneath it and on its way to the hole or back to the receiver.

6.3 Implication for testing

In relation to the motivation for the work, the development of NDE techniques for the inspection of plates, there are two important outcomes from the study of non-propagating modes. The first is that the reflection of the S_0 mode occurs without change of phase, whereas the reflection of the A_0 mode occurs with a change of phase, for example a 90 degree delay in the more useful 1 MHz-mm case. It may be necessary to take account of this when dealing with the superposition of multiple reflected signals in an area-inspection technique. The second is that the non-propagating modes can enhance the displacement field at some distance from the end of the plate, and this indicates the importance of transducer placement for inspection. In the 1 MHz-mm case the field is enhanced within a region of about 5 plate thicknesses from the end of plate.

Research on the interaction between the S_0 Lamb mode and a circular defect was achieved in order to model a first approximation of corrosion patches and to give some background knowledge when processing the raw data from the plate tester device. It is essential when processing received signals to account properly for those which are reflected from different features. For example, studying interactions with corrosion-like defects is a necessity in order to understand what modes are converted at the defect and how they behave when they propagate back in the plate. That means their amplitude or reflection ratio, the beam spreading, and their interaction with additional displacements created at the feature. It was shown that not only common Lamb modes (A_0 and S_0 waves) are mode converted at the defect but there are also some other waves including Shear Horizontal and creeping waves, both of which may pollute the direct reflection from the defect.

Chapter 7

Future work

This thesis has investigated the scattering aspects of the reflection of fundamental Lamb modes from different defects. Several topics have been covered in some detail, and in this chapter, future work in these areas is proposed.

7.1 Towards a more realistic model of defects

Only straight edge circular holes have been studied in this thesis. But real corrosion patches are not perfectly circular nor do they have straight edges. Figures 7.1(a) and 7.1(b) show different types of defects that would be interesting to model using Finite Element or analytical methods. The circular shape of the defect in plan does not really need to be changed as corrosion patches are often more or less circular. But the through thickness shape is always very un-even.

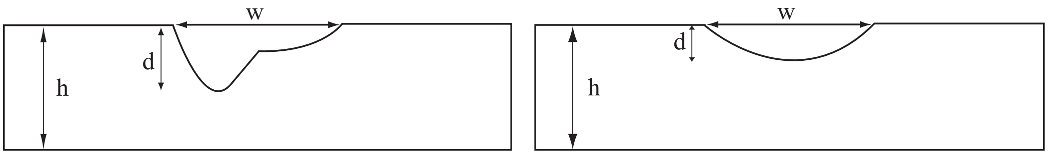

(a) **(b)**

Figure 7.1: Examples of defects to be studied.

Models will have to be performed in two major steps. First, 2-dimensional models will study the scattering aspect from infinitely long notches [51, 66] but with shapes such as in Figures 7.1(a) or 7.1(b). This approach should indicate the most important characteristics of the defects. Is it the depth (d on the figures), the length (w on the figures) or other parameters? Second, Once this study is done, one can move on to 3-dimensional plate design and study more realistic defects.

7.2 Using other modes

On thicker plates, a better approach may be to use a higher order low attenuation mode such as S_1.

Figure 7.2 shows a map of a 20 mm thick steel plate with various defects. The centre frequency of the incident S_0 Lamb mode used is 100 kHz. The scale of the plot is 30 dB (white 0 dB, black -30 dB). This is a very bad result because the edges of the plate cannot be distinguished from potential defects or even from the noise. The reason for this bad measurement is that on 20 mm thick plates, 100 kHz (or 2 MHz-mm) correspond to a dispersive area of the S_0 Lamb mode (see Figure 7.3), and there are multiple modes which do not simplify the processing of the measurements. But at lower frequencies, thus in the non dispersive regime, would not give better results as the EMATs would not behave at their best. Another idea would be to use another mode at a higher frequency which is more appropriate for the EMATs. Hence, a stronger mode could be excited and better results should be obtained.

Figure 7.3 shows the dispersion curves for a 20 mm thick steel plate. In the frequency range highlighted in white, several modes appear. The S_1 Lamb mode (thicker line) was chosen to perform a test. Figure 7.4 shows the map of the same plate as in Figure 7.2 but when a 220 kHz centre frequency S_1 Lamb mode is used. The scale of the plot is the same as in the previous figure, that is to say 30 dB. This time, the edges of the plate can be clearly seen as well as potential defects. But some work still needs to be done on the processing. Nevertheless, this first result looks very promising.

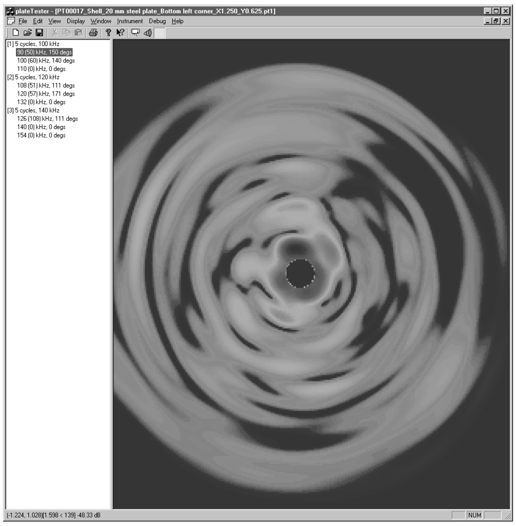

[1] 5 cycles, 100 kHz
    90 (50) kHz, 150 degs
    100 (60) kHz, 140 degs
    110 (0) kHz, 0 degs
[2] 5 cycles, 120 kHz
    108 (51) kHz, 111 degs
    120 (57) kHz, 171 degs
    132 (0) kHz, 0 degs
[3] 5 cycles, 140 kHz
    126 (108) kHz, 111 degs
    140 (0) kHz, 0 degs
    154 (0) kHz, 0 degs

(-1.224, 1.028)[1.598 < 139] -48.33 dB

Figure 7.2: Map of a 20 mm thick steel plate when the incident signal is S_0 at 100 kHz.

The advantage of using a higher mode is that the operating frequency is higher. Hence, a better resolution is acquired. The disadvantages of using higher modes is that there are more unwanted modes present that need to be suppressed by the processing algorithm and that the defect sensitivity is unknown. Furthermore there is a limited range of test frequencies. Mode conversion could possibly be used at these higher frequencies, giving more information on the defects. In turn, this would require more work on scattering studies, particulary for realistic defects (see section 7.1). The new research will have to address all these issues.

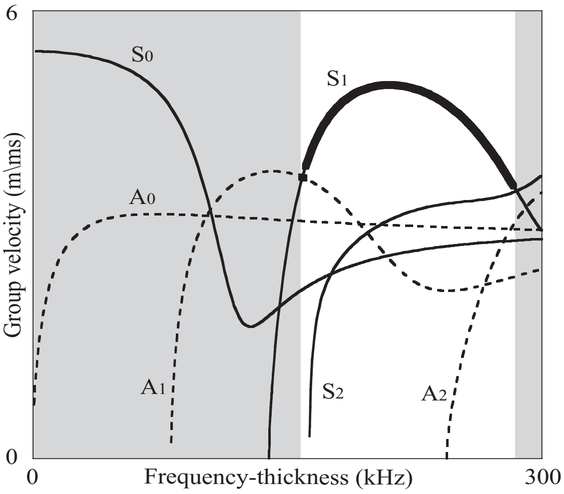

Figure 7.3: Dispersion curves for a 20 mm thick steel plate.

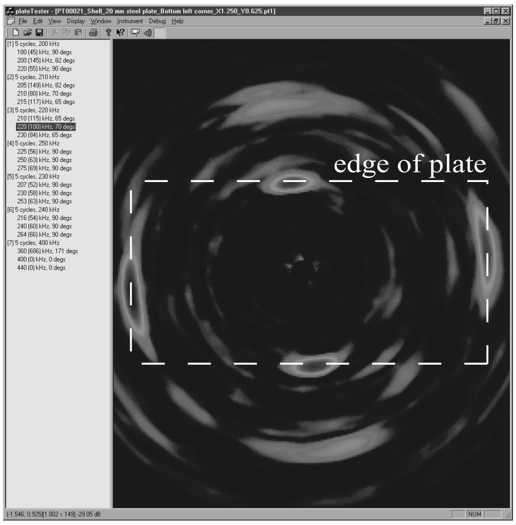

```
[1] 5 cycles, 200 kHz
    180 (45) kHz, 90 degs
    200 (145) kHz, 82 degs
    220 (55) kHz, 90 degs
[2] 5 cycles, 210 kHz
    205 (149) kHz, 82 degs
    210 (80) kHz, 70 degs
    215 (117) kHz, 65 degs
[3] 5 cycles, 220 kHz
    210 (115) kHz, 65 degs
    220 (100) kHz, 70 degs
    230 (84) kHz, 65 degs
[4] 5 cycles, 250 kHz
    225 (56) kHz, 90 degs
    250 (63) kHz, 90 degs
    275 (69) kHz, 90 degs
[5] 5 cycles, 230 kHz
    207 (52) kHz, 90 degs
    230 (58) kHz, 90 degs
    253 (63) kHz, 90 degs
[6] 5 cycles, 240 kHz
    216 (54) kHz, 90 degs
    240 (60) kHz, 90 degs
    264 (66) kHz, 90 degs
[7] 5 cycles, 400 kHz
    360 (686) kHz, 171 degs
    400 (0) kHz, 0 degs
    440 (0) kHz, 0 degs
```

```
(-1.546, 0.925)[1.802 < 149] -29.05 dB
```

Figure 7.4: Map of a 20 mm thick steel plate when the incident signal is S_1 at 220 kHz.

References

[1] P.D. Wilcox, M.J.S. Lowe, and P. Cawley. An EMAT array for the rapid inspection of large structures using guided waves. In D.O. Thompson and D.E. Chimenti, editors, *Review of Progress in Quantitative NDE.* American Institute of Physics, New York, 2003, in press.

[2] RTD. http://www.rtd.nl/en.

[3] Baker Hughes. http://www.bakerhughes.com/bakerhughes/index.htm.

[4] P.D. Wilcox, M.J.S. Lowe, and P. Cawley. Lamb and shear wave transducer arrays for the inspection of large areas of thick plates. In D.O. Thompson and D.E. Chimenti, editors, *Review of Progress in Quantitative NDE*, volume 19, pages 1049–1056. Plenum Press, New York, 2000.

[5] M. Lowe. Matrix techniques for modeling ultrasonic waves in mutilayered media. *IEEE Trans. Ultrason. Ferroelectr. Freq. Control*, 42:525–542, 1995.

[6] B.N. Pavlakovic, M.J.S. Lowe, D.N. Alleyne, and P. Cawley. Disperse: A general purpose program for creating dispersion curves. In D.O. Thompson and D.E. Chimenti, editors, *Review of Progress in Quantitative NDE*, volume 16, pages 185–192. Plenum Press, New York, 1997.

[7] P.J. Torvik. Reflection and wave trains in semi-infinite plates. *J. Acoust. Soc. Am.*, 41:346–353, 1967.

[8] B.A. Auld and E.M. Tsao. A variational analysis of edge resonnances in semi-infinite plates. *IEEE Trans. Sonics Ultrason.*, SU-24:317–326, 1977.

[9] I. A. Viktorov. R*ayleigh and* L*amb waves.* Plenum Press, New York, 1970.

[10] S. Zhang, J. Shen, and C. Ying. The reflection of the Lamb wave by a free plate edge : visualisation and theory. *Mater. Eval.*, 46:638–641, 1988.

[11] D.N. Alleyne and P. Cawley. The interaction of Lamb waves with defects. *IEEE Trans. Ultrason. Ferroelectr. Freq. Control*, 39:381–397, 1992.

[12] M. Ech-Cherif El-Kettani, P. Pareige, F. Luppe, and J. Ripoche. Experimental study of the conversion of Lamb waves at the end of an immersed plate. *Acoustica*, 82:251–259, 1996.

[13] R. Briers, O. Leroy, and G.N. Shkerdin. Conversion of a Stoneley wave at the extremity of a fluid-loaded plate. *J. Acoust. Soc. Am.*, 101:1347–1357, 1997.

[14] H. Lamb. On waves in an elastic plate. In *Proc. R. Soc. London, Ser. A*, pages 114–128, 1917.

[15] D.C. Worlton. Ultrasonic testing with Lamb waves. *NonDestr. Test.*, 15:218–222, 1957.

[16] D. Worlton. Experimental confirmation of Lamb waves at megacycle frequencies. *J. Appl. Phys.*, 32:967–971, 1961.

[17] D.N. Alleyne. *The nondestructive testing of plates using ultrasonic* L*amb waves*. PhD thesis, University of London, 1991. Mechanical Engineering.

[18] D. Chimenti and A. Nayfeh. Ultrasonic reflection and guided wave propagation in biaxially laminated composite plates. *J. Acoust. Soc. Am.*, 87:1409–1415, 1990.

[19] C. Aristégui. *Anisotropie élastique totale naturelle ou induite*. PhD thesis, Université de Bordeaux, 1997. Ultrason.

[20] A.K. Mal, P.-C. Xu, and Y. Bar-Cohen. Leaky Lamb waves for the ultrasonic non-destructive evaluation of adhesive bonds. *Journal of Engineering Materials + Technology*, 112:255–259, 1990.

[21] W. Mohr and P. Holler. On inspection of thin-walled tubes for transverse and longitudinal flaws by guided ultrasonic waves. *IEEE Trans. Sonics Ultrason.*, SU-23:369–378, 1976.

[22] W. Bottger, H. Schneider, and W. Weingarten. Prototype EMAT system for tube inspection with guided ultrasonic waves. *Nuclear Eng. Design*, 102:356–376, 1987.

[23] J.H. Rose, M. Bilgen, and P.B. Nagy. Acoustic double-reflection and transmission at a rough water-solid interface. *J. Acoust. Soc. Am.*, 95:3242–3251, 1994.

[24] J.J. Ditri. Utilization of guided elastic waves for the characterization of circumferential cracks in hollow cylinders. *J. Acoust. Soc. Am.*, 96:3769–3775, 1994.

[25] D.N. Alleyne and P. Cawley. Long range propagation of Lamb waves in chemical plant pipework. *Mater. Eval.*, 55:504–508, 1997.

[26] D.N. Alleyne, M.J.S. Lowe, and P. Cawley. The reflection of guided waves from circumferential notches in pipes. *J. Appl. Mech*, 65:635–641, 1998.

[27] M.J.S. Lowe, D.N. Alleyne, and P. Cawley. The mode conversion of a guided wave by a part-circumferential notch in a pipe. *J. Appl. Mech*, 65:649–656, 1998.

[28] S. Datta. Wave propagation in the presence of interface layers in composites. *Materials Science and Engineering*, A126:141–147, 1990.

[29] S.K. Datta, T.H. Ju, and Shah A.H. Scattering of an impact wave by a crack in a composite plate. *J. Appl. Mech.*, 59, 1992.

[30] Y. Bar-Cohen and D.E. Chimenti. Non-destructive evaluation of composite laminates by leaky Lamb waves. In D.O. Thompson and D.E. Chimenti, editors, *Review of Progress in Quantitative NDE*, pages 1–8. Plenum Press, New York, 1985.

[31] N.Q. Guo and P. Cawley. The finite element analysis of the vibration characteristics of piezoelectric discs. *J. Sound Vib.*, 159:115–138, 1992.

[32] R.D. Mindlin. Waves and vibrations in isotropic, elastic plates. In N.S. Goodier, editor, *First Symposium on Naval Structural Mechanics*, pages 199–232. Pergamon Press, 1960.

[33] B.A. Auld. *Acoustic Fields and Waves in Solids*, volume 2. Krieger Publishing Company, Malabar, Florida, 1990.

[34] Y. Cho and J.L. Rose. A boundary element solution for a mode conversion study on the edge reflection of Lamb waves. *J. Acoust. Soc. Am.*, 99:2097–2109, 1996.

[35] M. Onoe. Contour vibration of thin rectangular plates. *J. Acoust. Soc. Am.*, 30:1159–1162, 1958.

[36] D. Gazis and R. Mindlin. Extensional vibrations and waves in a circular disk and a semi-infinite plate. *Transactions of the American Society of Mechanical Engineers, J. Appl. Mech*, 27:541–547, 1960.

[37] R.D. Gregory and I Gladwell. The reflection of a symmetric Rayleigh-Lamb wave at the fixed or free edge of a plate. *Journal of Elasticity*, 13:185–206, 1983.

[38] E. Le Clézio, M.V. Predoi, and M. Castaings. Numerical predictions and experiments on the free-plate edge mode. *Ultrasonics*, 41:25–40, 2003.

[39] X-M. Wang and C.F. Ying. Scattering of Lamb waves by a circular cylinder. *J. Acoust. Soc. Am.*, 110:1752–1763, 2001.

[40] N.F. Haines. The theory of sound transmission and reflection at contacting surfaces. Technical report, CEGB Berkely Nuclear Laboratories, 1980.

[41] O. Buck, R.B. Thompson, and D.K. Rehbein. The interaction of ultrasound with contacting asperities : applications to crack closure and fatigue crack growth. *J. Nondestruct. Eval*, 4:203–212, 1984.

[42] O. Buck, R.B. Thompson, D.K. Rehbein, D.D. Palmer, and L.S.H. Brasche. Contacting surfaces : a problem in fatigue and diffusion bonding. *Metallurgical Transactions*, 20A:627–635, 1989.

[43] F.J. Margetan, R.B. Thompson, and T.A. Gray. Experimental studies pertaining to the interaction of ultrasound with metal-metal bonds. In D.O. Thompson and D.E. Chimenti, editors, *Review of Progress in Quantitative NDE*, volume 9, pages 1323–1330. Plenum Press, New York, 1990.

[44] F.J. Margetan, R.B. Thompson, J.H. Rose, and T.A. Gray. The interaction of ultrasound with imperfect interfaces : experimental studies of model structures. *J. Nondestruct. Eval*, 11:109–126, 1992.

[45] Y. Cho, D.D. Hongerholt, and J.L. Rose. Lamb wave scattering analysis for reflector characterization. *IEEE Trans. Ultrason. Ferroelectr. Freq. Control*, 44:44–52, 1997.

[46] T.L. Mansfield. Lamb wave inspection of aluminium sheet. *Mater. Eval.*, 33:96–100, 1975.

[47] S. Rokhlin. Resonance phenomena of Lamb waves scattering by a finite crack in a solid layer. *Journal of the American Ceramic Society*, 69:922–928, 1981.

[48] J. Paffenholz, W. Fox, X. Gu, G. Jewett, S. Datta, and H. Spetzler. Experimental and theoretical study of Rayleigh-Lamb waves in a plate containing a surface-breaking crack. *Res. Non-Destr. Eval.*, 1:197–217, 1990.

[49] D.N. Alleyne and P. Cawley. Optimization of Lamb wave inspection techniques. *NDT & E Int.*, 25:11–22, 1992.

[50] T. Ghosh, T. Kundu, and P. Karpur. Efficient use of Lamb modes for detecting defects in large plates. *Ultrasonics*, 36:791–801, 1998.

[51] M.J.S. Lowe and O. Diligent. The low frequency reflection characteristics of the fundamental symmetric Lamb wave s_0 from a rectangular notch in a plate. *J. Acoust. Soc. Am.*, 111:64–74, 2002.

[52] L. Flax, G.C. Gaunaurd, and Überall H. Theory of resonance scattering. *Physical Acoustics*, 15:191–293, 1981.

[53] J.L. Opsal and W.M. Visscher. Theory of elastic wave scattering: Apppli-cations of the method of optimal truncation. *J. Appl. Phys.*, 58:1102–1115, 1985.

[54] J.C. McKeon and M.K. Hinders. Lamb wave scattering from a through hole. *J. Sound Vib.*, 224:843–862, 1999.

[55] C.F Ying and R. Truell. Scattering of a plane longitudinal wave by a spherical obstacle in an isotropically elastic solid. *J. App. Phys.*, 27:1086–1097, 1955.

[56] I.A Viktorov. Rayleigh-type waves on cylindrical surfaces. *J. Acoust. Soc. Am.*, 4:131–136, 1958.

[57] W. Hassan and P. Nagy. Circumferential creeping waves around a fluid-filled cylindrical cavity in an elastic medium. *J. Acoust. Soc. Am.*, 101:2496–2503, 1997.

[58] P.B. Nagy, M. Blodgett, and M. Golis. Weep hole inspection by circumferential creeping waves. *NDT&E Int*, 27:131–142, 1994.

[59] X.L. Bao, K. Raju, and H. Überall. Circumferential waves on an immersed, fluid-filled elastic cylindrical shell. *J. Acoust. Soc. Am.*, 105:2704–2709, 1990.

[60] G. Maze, F. Léon, and H. Überall. Repulsion phenomena in the phase-velocity dispersion curves of circumferential waves on elastic cylindrical shells. *J. Acoust. Soc. Am.*, 105:1695–1701, 1999.

[61] G. Liu and J. Qu. Transient wave propagation in a circular annulus subjected to transient excitation on its outer surface. *J. Acoust. Soc. Am.*, 104:1210–1220, 1998.

[62] G. Liu and J. Qu. Guided circumferential waves in a circular annulus. *J. Appl. Mech*, 65:424–430, 1998.

[63] J. Qu, J.D. Achenbach, and R.A. Roberts. Dispersion of guided circumferential waves in a circular annulus. *IEEE Trans. Ultrason. Ferroelectr. Freq. Control*, 36:280–286, 1989.

[64] J. Qu, Y. Berthelot, and L. Li. Dispersion of guided circumferential waves in a circular annulus. In D.O. Thompson and D.E. Chimenti, editors, *Review of Progress in Quantitative NDE*, volume 15, pages 169–176. Plenum Press, New York, 1996.

[65] C. Valle, M. Niethammer, J. Qu, and L.J. Jacobs. Crack characterization using guided circumferential waves. *J. Acoust. Soc. Am.*, 110:1282–1290, 2001.

[66] M.J.S. Lowe, P. Cawley, J-K. Kao, and O. Diligent. The low frequency reflection characteristics of the fundamental anti-symmetric Lamb wave a0 from a rectangular notch in a plate. *J. Acoust. Soc. Am.*, 112:2612–2622, 2002.

[67] O. Diligent, M.J.S. Lowe, and P. Cawley. Reflection and scattering of the s_0 Lamb mode from circular defects in plates. In D.O. Thompson and D.E. Chimenti, editors, *Review of Progress in Quantitative NDE*, volume 20B, pages 1134–1141. American Institute of Physics, 2001.

[68] O. Diligent, M.J.S. Lowe, E. Le Clézio, M. Castaings, and B. Hosten. prediction and measurement of non-propagating Lamb modes at the free end of a plate when the fundamental antisymmetric mode a_0 is incident. *J. Acoust. Soc. Am., in press*, 113:3032–3042, 2003.

[69] E. Le Clézio. *Diffraction des ondes de* L*amb par des fissures verticales.* PhD thesis, Université Bordeaux I, 2001.

[70] P. Kirrmann. On the completeness of the Lamb waves. *J. of Elasticity*, 37:39–69, 1995.

[71] *Vibrometer operator's manual for Polytec Vibrometer OFV 2700.* Lambda Photometrics Ltd., Lambda House, Harpenden Hertfordshire AL5 5BZ, UK, 1999.

[72] D. Hitchings. Fe77 user manual. Technical report, Imperial College of Science, Technology and Medicine, London, UK, 1994.

[73] K.-J. Bathe. *Finite Element procedures in engineering analysis.* Prentice-Hall, Englewood Cliffs, New Jersey, 1982.

[74] B.N. Pavlakovic, D.N. Alleyne, M.J.S. Lowe, and P. Cawley. Simulation of Lamb waves propagation using pure mode. In D.O. Thompson and D.E. Chimenti, editors, *Review of Progress in Quantitative NDE*, volume 17, pages 1003–1010. Plenum Press, New York, 1998.

[75] A.N. Norris and C. Vemula. Scattering of flexural waves on thin plates. *J. Sound Vib.*, 181:115–125, 1995.

[76] A.N. Norris and C. Vemula. Flexural wave propagation and scattering on thin plates using mindlin theory. *Wave Motion*, 26:1–12, 1997.

[77] Z. Chang and A.K. Mal. Scattering of Lamb waves from a rivet hole with edge cracks. *Mech. Materials*, 31:197–204, 1999.

[78] J.D. Achenbach and Y. Xu. Wave motion in an isotropic elastic layer generated by a time-harmonic point load of arbitrary direction. *J. Acoust. Soc. Am.*, 106:83–90, 1999.

[79] J.L. Rose, J.J. Ditri, A. Pilarski, K. Rajana, and F. Carr. A guided wave inspection technique for nuclear steam generator tubing. *NDT & E Int.*, 27:307–310, 1994.

[80] J. Rasmussen. Prediction of fatigue using ultrasonic surface waves. *Non-Destructive Testing*, 20:103–110, 1962.

[81] A.J. Testa and C.P. Burger. A measurement of crack depth by changes in the frequency spectrum of Rayleigh wave. In *Novel non-destructive testing methods for materials*, pages 91–108. American Institute of Mining Metallurgical and Petroleum Engineers, 1983.

[82] T. Grahn. *Scattering of elastic waves from inhomogenities in solids.* PhD thesis, Chalmers univerity of technology, 2001. Application to Ultrasonic NDT.

[83] O. Diligent, T. Grahn, A. Boström, P. Cawley, and M.J.S. Lowe. The low-frequency reflection and scattering of the s_0 Lamb mode from a circular through-thickness hole in a plate: Finite element, analytical and experimental studies. *J. Acoust. Soc. Am.*, 112:2589–2601, 2002.

[84] P.D. Wilcox, M.J.S. Lowe, and P. Cawley. Long range Lamb wave inspection: the effect of dispersion and modal selectivity. In D.O. Thompson and D.E. Chimenti, editors, *Review of Progress in Quantitative NDE*, volume 18, pages 151–158. Plenum Press, New York, 1999.

[85] I. Viktorov, O. Zubova, and T. Kaekina. Investigation of Lamb wave excitation by the “wedge” method. *Soviet Physics - Acoustics*, 10:354–359, 1965.

[86] Y.V. Gulayev, Plesskii V.P., and Y.A. Ten. Excitation of surface acoustic waves by means of a wedge. *American Institute of Physics*, 27:472–475, 1981.

[87] V. Krylov. Wedge acoustic waves : new theoretical and experimental results. *Acoustoelectronics*, pages 174–189, 1989.

[88] J. Ditri, J. Rose, and A. Pilarski. Generation of guided waves in hollow cylinders by wedge and comb type transducers. In D.O. Thompson and D.E. Chimenti, editors, *Review of Progress in Quantitative NDE*, volume 12, pages 211–218. Plenum Press, New York, 1993.

[89] X. Jia. Modal analysis of Lamb wave generation in elastic plates by liquid wedge transducers. *J. Acoust. Soc. Am.*, 101:834–842, 1996.

[90] D.N. Alleyne and P. Cawley. The excitation of Lamb waves in pipes using dry coupled piezoelectric transducers. *J. NDE*, 15:11–20, 1996.

[91] D. Alleyne, B. Pavlakovic, M.J.S Lowe, and P. Cawley. Rapid, long range inspection of chemical plant pipe work using guided waves. In D.O. Thompson and D.E. Chimenti, editors, *Review of Progress in Quantitative NDE*, volume 20A, pages 180–187. American Institute of Physics, 2001.

[92] D. Alleyne and P. Cawley. A two-dimensional fourier transform method for the measurement of propagating multimode signals. *J. Acoust. Soc. Am.*, 89:1159–1168, 1991.

[93] A. Demma, P. Cawley, and M.J.S. Lowe. Scattering of the fundamental shear horizontal mode from steps and notches in plates. *J. Acoust. Soc. Am., in press*, 113:1880–1891, 2003.

[94] T. Grahn. Lamb wave scattering from a circular partly through-thickness hole in a plate. *Wave Motion*, 37:63–80, 2003.

[95] O. Diligent, M.J.S. Lowe, and P. Cawley. Reflection and scattering of the s0 Lamb mode from 3-d circular defects in plates. In D.O. Thompson and D.E. Chimenti, editors, *Review of Progress in Quantitative NDE*, volume 21, pages 231–238. American Institute of Physics, 2002.

[96] B.W. Maxfield, A. Kuramoto, and J.K. Hulbert. Evaluating EMAT designs for selected application. *Mater. Eval.*, 45:1166–1183, 1987.

[97] G.A. Alers and L.R. Burns. EMAT designs for special applications. *Mater. Eval.*, 45:1184–1189, 1987.

[98] R.B. Thompson. Physical principles of measurements with EMAT transducers. In Mason W.P. and Thurston R.N., editors, *Physical Acoustics*, volume XIX, pages 157–200. Academic Press, New York, 1990.

[99] W. Bottger, H. Schneider, and W. Weingarten. Tube inspection with an EMAT system using guided ultrasonic waves. In *4th Conference on NDT 1987*, pages 2305–2313. Pergamon, 1988.

[100] M. Gori, S. Giamboni, E. D'Alessio, S. Ghia, F. Cernuschi, and G.M. Piana. Guided waves by EMAT transducers for rapid defect location on heat exchanger and boiler tubings. *Ultrasonic*, 34:311–314, 1996.

[101] A.V. Clark Jr, R.E. Schramm, S. R. Schaps, and B.J. Filla. Safety assessment of railway wheels through roll-by detection of tread cracks. In Donald E. Gray

and D. Stone eds., editors, *SPIE Proceedings*, volume 2458, pages 109–119. Eng. Lib. TA 417.2N67237, 1995.

[102] H. Hirao, H. Ogi, and H. Fukuoka. Advanced ultrasonic method for measuring rail axial stresses with elctromagnetic acoustic transducer. *Research in Nondestructive Evaluation*, 5:211–223, 1994.

[103] R.E. Schramm. Ultrasonic measurement of stress in railroad wheels. *Review of Scientific Instruments*, 70(2):1468–1472, 1999.

[104] A.V. Clark Jr and S. R. Schaps. Measurement of plane stress states using electromagnetic - acoustic transducers. In D.O. Thompson and D.E. Chimenti, editors, *Review of Progress in Quantitative NDE*, volume 17, pages 1877 – 1882. Plenum Press, New York, 1995.

[105] H. Fukuoka, M. Hirao, H. Yamasaki, G. Ogi, G. Petersen, and C. Fortunko. Ultrasonic resonance method with emat for stress measurement in thin plates. In D.O. Thompson and D.E. Chimenti, editors, *Review of Progress in Quantitative NDE*, volume 12B, pages 2120–2136. Plenum Press, New York, 1993.

[106] G.A. Alers. *Non-contact Ultrasonic testing with electromagnetic transducers - Handbook of inteligent sensors for industrial automation*, pages 285–306. Nello Zuech Editor, Addison-Wesley Publishing Co. New York, 1992.

List of Publications

Lowe, M., and Diligent, O., *Low-Frequency reflection characteristics of the S0 Lamb wave from a rectangular notch in a plate*, J. Acoust. Soc. Am., Vol. 111(1), 64-74 (2002).

Diligent, O., Grahn, T., Bostrom, A., Cawley, P. and Lowe, M., *The low frequency reflection and scattering of the S0 Lamb mode from a through-thickness hole in a plate: Finite Element, analytical and experimental studies*, J. Acoust. Soc. Am., Vol. 112 (6), pp. 2589-2601 (2002).

Lowe, M.J.S., Cawley, P.,Kao, J-Y and Diligent, O., *The low-Frequency reflection characteristics of the fundamental antisymmetric Lamb wave A0 from a rectangular notch in a plate*, J. Acoust. Soc. Am., Vol. 112(6), 2612-2622 (2002).

Diligent, O., Lowe, M., Le Cézio, E., Castaings, M., Hosten, B., *Prediction and measurement of non-propagating Lamb modes at the free end of a plate when the fundamental antisymmetric mode A0 is incident*, J. Acoust. Soc. Am., Vol. 113 (6), pp. 3032-3042 (2003).

Lowe, M.J.S., Cawley, P.,Kao, J-Y and Diligent, O., *Prediction and measurement of the reflection of the fundamental anti-symmetric Lamb wave from cracks and notches*, in Review of Progress in QNDE, Vol. 19, eds. D. O. Thompson and D. E. Chimenti, American Institute of Physics, New York, 2000, pp. 193-200.

Lowe, M.J.S. and Diligent, O., *Reflection of the fundamental Lamb modes from the ends of plates*, in Review of Progress in QNDE, Vol. 20 eds. D.O. Thompson and D.E. Chimenti, American Institute of Physics, New York, 2001, pp. 89-96.

Diligent, O., Lowe, M.J.S. and Cawley, P., *Reflection and scattering of the S0 Lamb*

mode from circular defects in plates, in Review of Progress in QNDE, Vol. 20 eds. D.O. Thompson and D.E. Chimenti, American Institute of Physics, New York, 2001, pp. 134-141.

Wilcox, P., Evans, M., Diligent, O., Lowe, M., Cawley, P., *Dispersion and excitability of guided acoustic waves in isotropic beams with arbitrary cross section*, in Review of Progress in QNDE, Vol. 21 eds. D.O. Thompson and D.E. Chimenti, American Institute of Physics, New York, 2002, pp. 203-210.

Diligent, O., Lowe, M.J.S. and Cawley, P., *Reflection and scattering of the S0 Lamb mode from 3-D circular defects in plates*, in Review of Progress in QNDE, Vol. 21 eds. D.O. Thompson and D.E. Chimenti, American Institute of Physics, New York, 2002, pp. 231-238.

Diligent, O., Lowe, M.J.S. and Cawley, P., *Reflection of the S0 Lamb mode from part-depth circular defect in a plate, when the incident wave is created by a small source*, in Review of Progress in QNDE, Vol. 22 eds. D.O. Thompson and D.E. Chimenti, American Institute of Physics, New York, 2003, *in press*.